DESIGN, FABRICATION, AND PERFORMANCE OF HIGH-FREQUENCY PHASED-ARRAY ULTRASONIC ENDOSCOPES

By

André Bezanson

Submitted in partial fulfillment of the requirements
for the degree of Doctor of Philosophy

at

Dalhousie University
Halifax, Nova Scotia
March 2020

TABLE OF CONTENTS

LIST OF TABLES

LIST OF FIGURES

LIST OF ABBREVIATIONS AND SYMBOLS USED

%	Percent
±	Plus and minus
°	Degree
A	Area (when used within equations)
a	Source aperture (when used within equations)
$a(t)$	Echo intensity signal
C	Proportionality constant
c	Speed of sound
c_{piezo}	Speed of sound of a piezoelectric material
D	Diameter
d	Depth or distance
F	Focal length
$F_{\#}$	F-number; ratio of focal length to aperture
F_e	Effective focal distance
f	Frequency
f_c or f_o	Center frequency
k	Bandwidth factor
k_{eff}	Average electromechanical coupling factor
k_t	Electromechanical coupling coefficient
N_{31}	Lateral frequency coefficient
N_T	Thickness-mode frequency coefficient
R	Radius
R_c	Radius of curvature,
R_L	Lateral Resolution
R_A	Axial Resolution
R_{pr}	Reflected pressure ratio
t_m	Mass thickness
t_s	Spring thickness
v_s	Velocity of sound in parylene
$\overline{x}$	Displacement of point source to element center
Z_o	Acoustic impedance

Z_F	Focal depth of a geometrically focused transducer
α	Attenuation coefficient
β	Materials bulk modulus
θ_i	Incident angle
θ_t	Transmission angle
λ	Wavelength
μm	Micrometer
ρ	Density
ϕ	Phase shift
Ω	Ohm
2D	Two dimensional
3D	Three dimensional
A-mode	Amplitude mode
B-mode	Brightness mode
CT	Computed tomography
cos	Cosine
dB	Decibels
DNR	Dynamic range
DRIE	Deep reactive ion etching
E-Beam	Electron beam
FFT	Fast Fourier transform
F-number	Ratio of a focused system's focal length to aperture size
FPGA	Field programable gate array
ICE	Intracardiac echocardiography
I-Q	In-phase quadrature
IEEE	Institute of Electrical and Electronics Engineers
IVUS	Intravascular ultrasound
KLM	Krimholtz, Leedom and Matthaei
kPa	Kilopascal
kg	Kilogram
MR	Magnetic resonance
MRI	Magnetic resonance imaging
mm	Millimeter

m	Meter
MHz	Megahertz
mV	Millivolt
nm	Nanometer
OCT	Optical coherence tomography
PCB	Printed circuit board
PCIe	Peripheral component interconnect express
psi	Pounds per square inch
RF	Radiofrequency
Rayl	Rayleigh dimensional units of acoustic impedance ($kg/s/m^2$).
SCF	Sign coherence function
SNR	Signal-to-noise ratio
s	Second
sin	Sine
TPX	Polymethyl pentene
UFFC	Ultrasonic, Ferroelectrics and Frequency Control division of the Institute of Electrical and Electronics Engineers
USB	Universal serial bus
Vp-p	Peak-to-peak voltage

ABSTRACT

With a rapidly aging population, there is an imminent need to reduce healthcare costs and improve patient outcomes. Minimally invasive surgical procedures have the potential to help facilitate this objective due to shorter recovery times and improved outcomes. However, challenges with the visualization of tissues limit the adoption of these procedures. This work aims to help advance clinical practice by developing new techniques to produce high-resolution ultrasonic endoscopes for minimally invasive surgical procedures.

Micro-fabrication techniques are incorporated into a novel endoscopic ultrasonic transducer design, allowing for a 64-element array with an element pitch of 38 μm and an encapsulated transducer size of 2.5 mm by 3.1 mm. Impulse response simulation scripts are developed and tested to aid in the design and construction of the transducers. Tests on wire-phantoms and cadaveric porcine tissue showed a dynamic range of up to 60 dB, an axial resolution of 40 μm, and a lateral resolution of 152 μm.

An experimental design using Vernier element spacings was developed, modeled, constructed, and tested to passively reduce the effects of grating lobe image artifacts at high steering angles. The design utilizes a 128-element transducer with every third element providing pulse transmission and every fourth element providing pulse reception. The Vernier array design reduced the intensity of grating lobe image artifacts by 15 dB relative to the previously constructed array. However, the transducer's overall signal strength was attenuated by 18.2 dB, limiting the potential applications.

Kerfless array designs, without mechanical separation of the piezoelectric wafer between elements, were investigated due to their improved manufacturability. Though existing literature and simulations predicted poor performance of the kerfless arrays, measurements of their acoustic radiation patterns showed higher signal levels at steering angles beyond ± 20° than was expected. The simulation models were updated to include the effects of lateral acoustic emissions within the piezoelectric wafer. They provided a strong fit with experimental measurement, demonstrating the viability of kerfless array designs as a low-cost alternative to traditional arrays.

CHAPTER 1:

INTRODUCTION

Recent trends in surgical practice have shown a shift toward minimally invasive surgical procedures (Cullen and Talamini 2010; Fudulu et al. 2017) due to improved outcomes for patients (Ochsner 2000; Mu et al. 2015; Parisi et al. 2017; Y.-H. Zhang et al. 2016). However, there are significant challenges associated with the visualization of tissue during minimally invasive procedures (Wilhelm et al. 2018).

Ideally, imaging devices for minimally invasive procedures would provide high-resolution images of the tissue in real-time and would generate depth-resolved images into the anatomy, allowing visualization before resection. Currently, clinicians have access to a relatively wide array of endoscopic imaging tools such as optical video endoscopes, optical coherence tomography endoscopes (OCT), and low-resolution endoscopic ultrasound. However, at the current time, no endoscopic device can provide high-resolution images with significant cross-sectional depth, in real-time.

Clinicians can also make use of external imaging techniques such as computed tomography (CT), fluoroscopy (x-ray) and magnetic resonance imaging (MRI), among many others (Mezger, Jendrewski, and Bartels 2013). These external imaging techniques can be advantageous for diagnosis and intraoperative applications due to their abilities to image large cross-sectional volumes of tissue. However, their intraoperative use can be cumbersome, expensive, and potentially dangerous to the clinician if involving ionizing radiation. More importantly, these options may not provide the imaging resolution, frame rate, and tissue contrast required during minimally invasive procedures.

Endoscopic ultrasound fills a unique niche in minimally invasive procedures as it allows for real-time imaging without ionizing radiation and provides a deeper field of view than OCT. However, to achieve an endoscopic form-factor in existing ultrasonic devices, design compromises are implemented that degrade image resolution and introduce image artifacts.

The objective of this dissertation is to develop a new technologically advanced high-resolution ultrasonic endoscope. The initial focus was on the development of novel microfabrication techniques, facilitating the packaging of a forward-looking ultrasonic phased array into an endoscopic form-factor. From there, computational models were developed that allow for the optimization of endoscopic arrays. Each of the three studies in this work provides validation of the developed techniques through experimental testing and device characterization.

By developing prototypes for minimally invasive surgical procedures that aim to incorporate high-resolution ultrasonic imaging into endoscopic form-factors, this work aims to help advance imaging technologies and thereby contribute to improved patient care.

1.1 MOTIVATION

The world's population distribution is shifting toward an elderly demographic with a lower ratio of working-age individuals to elderly individuals (UN 2010). Predictions suggest that 22% of the world's population will be over the age of 60 years by 2050. As healthcare systems are already under significant pressure, this demographic shift presents substantial challenges in the coming years due to the increased demands on existing infrastructure and operations (Fuster 2017).

Though there are many technological advancements under development to improve healthcare and reduce costs, some notable examples of interest are the development of robotic caregivers (Vallor 2011), advancements in telepresence surgeries (Leal Ghezzi and Campos Corleta 2016), the improvement of healthcare through self-monitoring technologies (Pavel, Callaghan, and Dey 2010) and a shift toward minimally invasive surgical procedures (Ochsner 2000; Mu et al. 2015; Parisi et al. 2017; Y.-H. Zhang et al. 2016).

Minimally invasive surgical procedures present a promising option for decreasing some of the burdens on health care systems, as these procedures are associated with shorter hospital stays and faster recoveries (Bates and Divino 2015). A study by Fleshman et al. (1996), showed a significant reduction in hospital stays, from 9.7 days to 5.7 days, for patients undergoing treatment of colorectal cancer when minimally invasive procedures were utilized.

Recent work, however, suggests that increased training requirements limit the adoption of minimally invasive surgeries in clinical practice (Bates and Divino 2015), and that challenges exist in the visualization and manipulation of tissue during these procedures (Pierorazio and Allaf 2009). It follows that the development of more capable imaging devices will help to lessen this burden, aid adoption and improve outcomes.

Ultrasonic imaging is a valuable tool in medical imaging due to its low-cost and the generation of real-time images (K Kirk Shung 2015). However, typical high-resolution probes (Foster et al. 2009) are too large for endoscopic applications, and the existing endoscopic ultrasound devices incorporate significant design compromises that reduce their image resolution, introduce image artifacts, or limit the frame-rate of the acquired images (D. Zhou et al. 2011).

The purpose of this work is to generate the techniques and methods required to produce endoscopic ultrasound probes that generate high-resolution and real-time images. This dissertation details the design and fabrication of novel high-resolution ultrasonic endoscopes, and compares the experimental performance to the simulated designs.

1.2   RESEARCH OBJECTIVES AND HYPOTHESIS

The investigative work within this dissertation is broken down into three areas of study, with each study representing a significant body of work to which the author was the primary contributor. The primary areas of study are:

1.2.1 DEVELOPMENT OF AN ULTRASONIC PHASED-ARRAY ENDOSCOPE (STUDY 1 – CHAPTER 3)

This study's objective was to create an array that meets the miniature size requirements for a clinically useful forward-looking endoscope, while providing the performance of a high-density ultrasonic array. The hypothesis for this study was that a novel interconnect design and the application of new fabrication techniques would result in an acceptably miniaturized form-factor. The hypothesis was explored, and the prototype transducer provided images with steering angles up to $\pm$ 32° from a form-factor suitable for minimally invasive procedures. However, grating lobe image artifacts prevented imaging to the desired level of $\pm$ 45° that is seen in conventional low-frequency phased array systems.

1.2.2 A VERNIER ARRAY FOR GRATING LOBE SUPPRESSION (STUDY 2 – CHAPTER 4)

The objective of this study was to develop a passive method for the reduction of the grating lobe artifacts seen in study 1. The application of a Vernier array design was selected and explored as a method of passively attenuating grating lobe artifacts that avoided the need for computationally demanding post-processing techniques. The hypothesis was that the technique could suppress the off-axis constructive interference of grating lobes. Testing showed that the use of Vernier element spacings provided attenuation of grating lobe artifacts by approximately 15 dB, however, the overall signal-to-noise ratio was reduced, limiting the potential applications of this technique.

1.2.3 PERFORMANCE EVALUATION OF KERFLESS ARRAYS WITH UPDATED MODELING TECHNIQUES (STUDY 3 – CHAPTER 5)

Kerfless array designs were used in several phased arrays tested in studies 1 and 2. In these kerfless arrays, neighboring elements are not physically separated from each other by machined slots. Previous literature suggests that steering to angles beyond $\pm$ 15° would not provide useable levels of return signal. However, this prediction contradicted the results from studies 1 and 2, where signals remained significant to $\pm$ 32°. The objective of this study was to determine the fundamental reason for the better-than-expected performance.

The hypothesis for this work was that active beamforming was suppressing lateral waves that would otherwise contribute to reduced beamformed directivity; that as the lateral acoustic waves moved across the array stack, after the firing of an element, they would be canceled out by the acoustic waves emanating from neighboring elements as they fired in turn. Updated simulations and experimental testing, however, suggests that the unexpected performance primarily results from the acoustic emissions of the lateral acoustic wave and its interaction with the primary acoustic pulse from the original element. This study describes the development of a new method of modeling this phenomenon and includes experimental verification using newly developed kerfless and kerfed phased arrays.

1.3 THESIS STRUCTURE

Chapter 1 presents the motivation for the investigative studies presented herein. As clinical techniques move towards minimally invasive procedures, advancements are needed in the miniaturization of ultrasonic devices. This chapter outlines the three main research objectives of this work and presents information on the structure of the dissertation. Finally, a summary of the author's contributions to each body of work is presented.

Chapter 2 reviews the relevant background literature related to the design of ultrasonic transducers. This chapter details some of the underlying methodologies used to simulate ultrasonic transducer designs through electromechanical modeling and acoustic simulations based on the impulse response function. Additionally, this chapter describes existing fabrication processes used in high-frequency ultrasonic arrays and presents challenges associated with the adaptation of their design to endoscopic form-factors.

Chapter 3 presents the first investigative study. The design, fabrication, and performance assessment of an ultrasonic endoscope is presented. The specifics of the design are summarized and related to theoretical models. Subsequently, the methods of construction are detailed for the completed design. The performance of the constructed devices is investigated and summarized. Chapter 3 concludes with a discussion of the potential applications for the developed endoscopic device. The limitations of the devices, due to grating lobe image artifacts, are discussed and present a topic of investigation in study 2 (Chapter 4).

However, better-than-expected imaging performance is observed and presents the basis for study 3 (Chapter 5).

Chapter 4 presents study 2, which investigates the application of a Vernier transmit and receive strategy to reduce the grating lobe image artifacts seen in study 1. Simulations are developed that allow for the prediction of ultrasonic radiation patterns from the Vernier arrays. The fabrication of endoscopic Vernier arrays is developed and detailed. The results of physical characterization are discussed and contrasted against theoretical expectations. The chapter concludes with a discussion of the trade-offs between reduced sensitivity and improved grating lobe performance provided by Vernier arrays.

Study 3 in Chapter 5 investigates the better-than-expected performance of the transducers developed during study 1 (Chapter 3). The chapter begins with an introduction to the standard simulation methods and theorizes on the limitations in the standard models. From there, current simulation techniques are expanded to allow for the integration of lateral acoustic modes into the models. The simulation results are then compared against physical arrays. Chapter 5 concludes with a discussion of the simulation techniques that were used and presents recommendations on future applications of this model.

Chapter 6 presents a general discussion of the results of studies 1, 2, and 3. It discusses how the work presented in this thesis suggests that viable techniques for the construction of high-resolution ultrasonic endoscopes are now established. Future work may be able to take advantage of the characteristics of kerfless arrays for improved manufacturability of endoscopic devices. Additionally, it is suggested that further investigations into the design of kerfless arrays may allow for the generation of a low-frequency imaging mode that may have the potential to provide an expanded field of view.

1.4   CONTRIBUTIONS

In study 1, I was responsible for the design, fabrication, and characterization of the miniaturized transducer array. Additionally, I was the first author on the resulting journal article (Bezanson, Adamson, and Brown 2014), and conference proceedings (Bezanson, Adamson, and Brown 2013; Bezanson et al. 2012). I also contributed to a patent (Bezanson,

Adamson, and Brown 2015) based on this work. The study included field modeling of the ultrasonic energy emitted and received by the arrays using a model based on the impulse response function. For this portion of the work, I expanded on a computational script written by Dr. Zahra Torbatian that solved for the impulse response function. I generalized the script to allow for the computation of the impulse response function, without region-based conditional arguments, and built a script that used this function to simulate the ultrasonic fields produced by the transducers developed in this study. Additionally, I modified and applied microfabrication procedures, such as photolithography, wire-bonding, flex-circuit design, micro-dicing, and lapping, as required for the construction of the array. The presentation of this work won the student paper award at the 2013 Institute of Electrical and Electronics Engineers (IEEE) Ultrasonics, Ferroelectrics and Frequency Control (UFFC) conference in Prague (2014).

In study 2, I was responsible for the design, fabrication, and characterization of the Vernier transducer array. However, the concept of Vernier array transducers and their application in reducing grating lobes was developed by Brunke and Lockwood (1997). To complete the primary publication related to this study (Bezanson, Leadbetter, and Brown 2014), I completed the design, simulation, and construction of the Vernier ultrasonic endoscope and drafted the publication. Additionally, I tested and characterized the design, as documented in the publication (Bezanson, Leadbetter, and Brown 2014).

In study 3, I developed a hypothesis for the mechanism causing the better-than-expected performance of our kerfless linear arrays. To explore this hypothesis, I expanded the existing simulation models, from studies 1 and 2, to include the effects of lateral wave propagation in the piezoelectric substrate. I constructed kerfless and fully-kerfed arrays to validate the model. As a final contribution, I tested the arrays and documented the study. This work is unpublished at the time of this thesis submission and will be submitted for publication after the defense of the thesis. This chapter also expands on ideas originally presented by Garland et al, (2011), a publication to which I provided experimental data.

Contributions to three additional publications (Bezanson, Adamson, and Brown 2011; Brown et al. 2013; Samson, Bezanson, and Brown 2017) were made during my studies. While related to the development of ultrasonic imaging systems, these projects are not covered within the scope of this thesis.

CHAPTER 2:

BACKGROUND

Since the development of x-ray projection imaging in 1895 by Roentgen (Scatliff and Morris 2014), medical professionals have been able to image the internal anatomy of the human body non-invasively. When introduced in the 1970s, medical pulse-echo ultrasound systems represented a significant milestone by providing a method for obtaining images of internal anatomy without ionizing radiation (Bradley 2008). Since then, ultrasound has found its place in clinical radiology as a universal, non-ionizing imaging modality with relatively high spatial/temporal resolution and soft-tissue contrast.

Complimentary to ultrasound, non-invasive imaging techniques such as CT, x-ray, and MRI provide diagnostic images of the internal structures of the body (Scatliff and Morris 2014). These techniques, however, can be expensive, cumbersome, and (except for MRI) expose patients and staff to ionizing radiation when used for intraoperative imaging (Shearwood and Goldstein 2017). X-ray, CT, and MRI, however, all have the advantage of a larger field of view than ultrasound and can image through dense materials such as bone. The clinician must carefully weigh the relative characteristics of each imaging modality when selecting the appropriate solution for their patient.

Optical visualization devices, such as microscopes and flexible optical endoscopes, are also an essential part of the clinician's toolkit. However, standard optical techniques cannot visualize structures beyond the tissue surface. OCT allows for the use of light for depth-resolved imaging but is fundamentally limited to a couple of millimeters of tissue penetration, due to the high attenuation and scattering of light within opaque tissue (Fujimoto and Swanson 2016).

The use of ultrasound is prevalent in the medical field due to its low cost, portability, and ease of use (Szabo 2004). Additionally, ultrasonic imaging offers advanced imaging modes such as Doppler (blood flow), elastography (tissue stiffness), and non-linear imaging (tissue contrast and resolution enhancement). Ultrasound also provides surgical guidance in applications such as the resection of pathological tissues, such as tumors. However, as surgical trends move towards minimally invasive approaches, conventional hand-sized ultrasound probes are often unsuitable for procedure guidance. As such, there is a need for high-resolution ultrasonic devices in an endoscopic form-factor that would bring the beneficial features of high-resolution ultrasonic transducers to minimally invasive applications.

2.1 TECHNICAL OVERVIEW - ENDOSCOPIC HIGH-FREQUENCY ULTRASOUND

Minimally invasive procedures require higher resolution and smaller probes than are available with standard ultrasound systems. In theory, high-frequency ultrasound could satisfy these conditions, as it allows for the generation of high-resolution real-time images and reduces the required size of the transducer elements.

The wavelength of the acoustic wave (λ) produced by an ultrasonic transducer correlates to the size of resolvable features. As the frequency (f) of sound increases, the acoustic wavelength decreases proportionally, according to:

$$\lambda = {}^{c}\!/_{f} \qquad\qquad (2\text{-}1)$$

where c represents the acoustic wave's propagation velocity, the speed of transmitted sound, and is a property of the imaged medium. Image resolution is inversely proportional to the acoustic wavelength. As the frequency of sound increases, finer structures are resolved, and the system's resolution increases. High-frequency sound waves attenuate faster during propagation, thereby reducing the depth of a high-resolution system's field of view relative to a low-resolution system.

The transducer elements within ultrasonic arrays are sized proportionally to the wavelength of sound that they produce. Therefore, as the frequency of sound increases, the wavelength

decreases, and the required transducer size decreases. However, as the transducer elements become smaller, they become more challenging to construct and electrically interconnect.

Recent works have shown that the increased resolution produced by high-frequency ultrasound provides precise measurement and visualization of various anatomical features (Ketterling et al. 2017; Urs, Ketterling, and Silverman 2016; Ramasawmy et al. 2016; Grune et al. 2018; Adelsperger et al. 2018). However, the limited penetration depth of hand-held high-frequency ultrasonic transducers restricts their applicability, as the tissue of interest is typically too deep to visualize from the human body's external surfaces. Although some endoscopic ultrasound arrays have been developed, high-frequency arrays have typically remained too large for endoscopic use, as designers have not been able to miniaturize the electrical interconnect.

Some specialized high-frequency ultrasonic endoscopes exist and provide clinically relevant imaging in intravascular, catheter-based applications. However, these devices are typically based on mechanically translated and unfocused single element transducers. The trade-off for these single element catheter-based devices is that their extremely small form-factors come with reduced image quality when compared to hand-held high-frequency ultrasonic transducers. This trade-off is primarily related to the use of unfocused single elements for imaging instead of more sophisticated ultrasonic arrays. Appendices B and C present a more detailed review of existing high-frequency and endoscopic imaging technologies and their applications.

This dissertation describes the development of novel endoscopic high-frequency imaging array probes. It presents newly developed microfabrication techniques for the miniaturization of the probes, new array geometries that minimize off-axis artifacts, and new techniques for modeling acoustic waves emitted by ultrasonic devices with large element-to-element coupling. The dissertation's research was undertaken to develop practical devices that provide high-resolution ultrasonic imaging during minimally invasive procedures.

2.2 TECHNICAL BACKGROUND – FUNDAMENTALS OF ULTRASONIC IMAGING

The ideal high-resolution ultrasonic endoscope would not sacrifice element density and image quality but would still provide a miniaturized endoscopic form-factor. The work presented in this dissertation describes the design, fabrication, and testing of a miniaturized, forward-looking, high-resolution endoscope. This design provides improved image quality over conventional endoscopic ultrasound probes that are based on low element counts or mechanical scanning. The transducer design achieves a high-density element count similar to high-quality external imaging probes that are significantly larger (Foster et al. 2009; L. Zhang et al. 2010; A. L. Bernassau et al. 2012).

The low-frequency analog to the probe developed in this dissertation is called a linear phased array. Phased arrays were initially developed to image the heart by imaging in-between the acoustically reflective rib bones. These probes produce a large field of view from a small aperture by steering the focused ultrasound beam outwards to a range of steering angles. Just as low-frequency phased arrays revolutionized ultrasonic cardiac imaging, high-frequency phased arrays could revolutionize many intra-operative surgical procedures by providing a large field of view from small surgical access routes.

In the design of ultrasonic transducers, there are three areas of study that must be combined for accurate modeling (Council 1996): (1) wave-based field distributions, (2) electromechanical transduction and (3) the mechanical and piezoelectric properties of transducer materials. In this work, the impulse response model is used to model the propagations of the acoustic waves, and the Krimholtz, Leedom, and Matthaei (KLM) model is used to model the electromechanical performance of the array (section 2.3.4).

2.2.1 PULSE-ECHO IMAGING

Conventional ultrasound works by transmitting vibrations (sounds waves) into a medium. The sound waves oscillate at frequencies much higher than can be heard by the human ear, and thus, the term 'ultrasound' is used (Bushberg and Boone 2011). The sound travels out into the medium and echoes off structures, as used by dolphins or bats to echo-locate food

sources. An illustrative example of the use of ultrasound in medical imaging is shown in Figure 2-1.
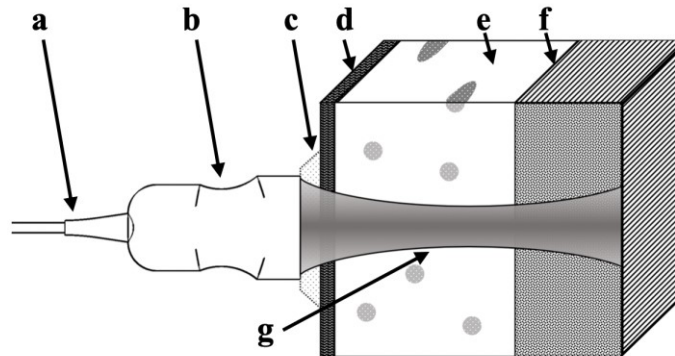
Figure 2-1: An illustrative example of an ultrasonic probe showing the emission of an ultrasonic pulse into a tissue sample. (a) transducer cable; (b) ultrasonic transducer; (c) coupling gel; (d) skin layer; (e) fat layer; (f) muscle layer; (g) ultrasonic beam.

The transducer generates ultrasonic sound waves that propagate into the tissue. Echoes of the pulse reflect off the interfaces between materials of different acoustic impedances and return to the transducer where they are detected and measured. The transducer shown in Figure 2-1 is focusing a transmit beam along a single scan line into the medium, thereby capturing a one-dimensional scan line. Equation (2-2) calculates the depth of each echo source within the tissue along the scan line:

$$d = \frac{c_0\, t}{2} \tag{2-2}$$

where d is the depth to the reflecting source, c_o is the speed of sound in the material, and t is the time from pulse transmission to the echo's return. Though the speed of sound varies in different biological tissues, it is typically assumed to be uniform throughout the field of view. For most tissues, the speed of sound is close to the speed of sound in water (Inagaki et al. 2018).

The transducer illustrated in Figure 2-2 is a phased array that uses timed delays (phase delays) to steer the acoustic beam to multiple angles on subsequent pulses, thereby forming a sector-shaped image. The phased array design allows a small transducer to image a large field-of-view.
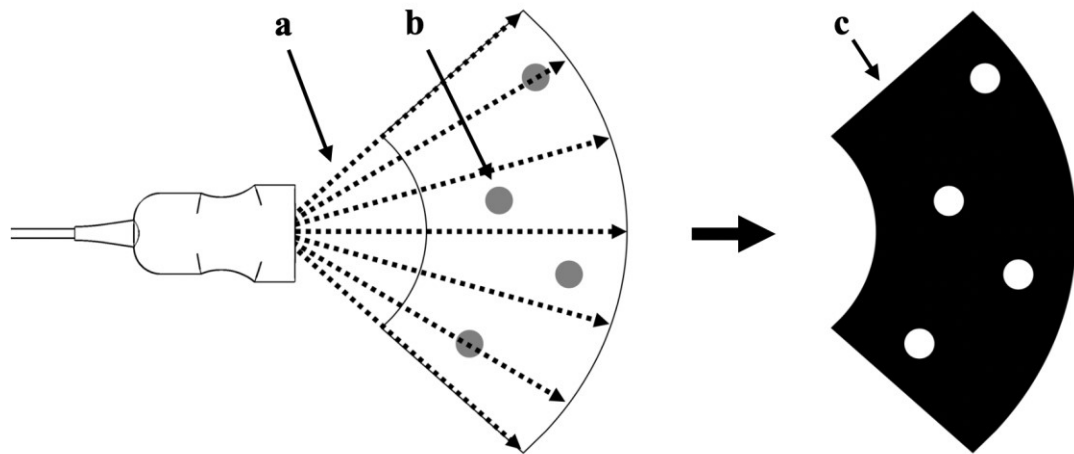
Figure 2-2: Adjacent scan lines are captured and stitched together to form a two-dimensional image of the transducer's field of view. (a) Scan lines; (b) acoustically reflective spheres; (c) resulting image. The resulting image displays the intensity of the acoustic reflection. Therefore, areas with high echo intensities are lighter, and areas without reflections are dark.

The transmission of a focused ultrasound beam allows for the insonification of a single line into the medium. Multiple scanlines must be acquired and stitched together to form a two-dimensional image, as shown in Figure 2-2.

Figure 2-3 shows an overview of the process by which the ultrasonic echoes are captured and processed for display. The procedure involves compensation for acoustic attenuation through time-gain amplification, signal intensity detection, and logarithmic compression for display.
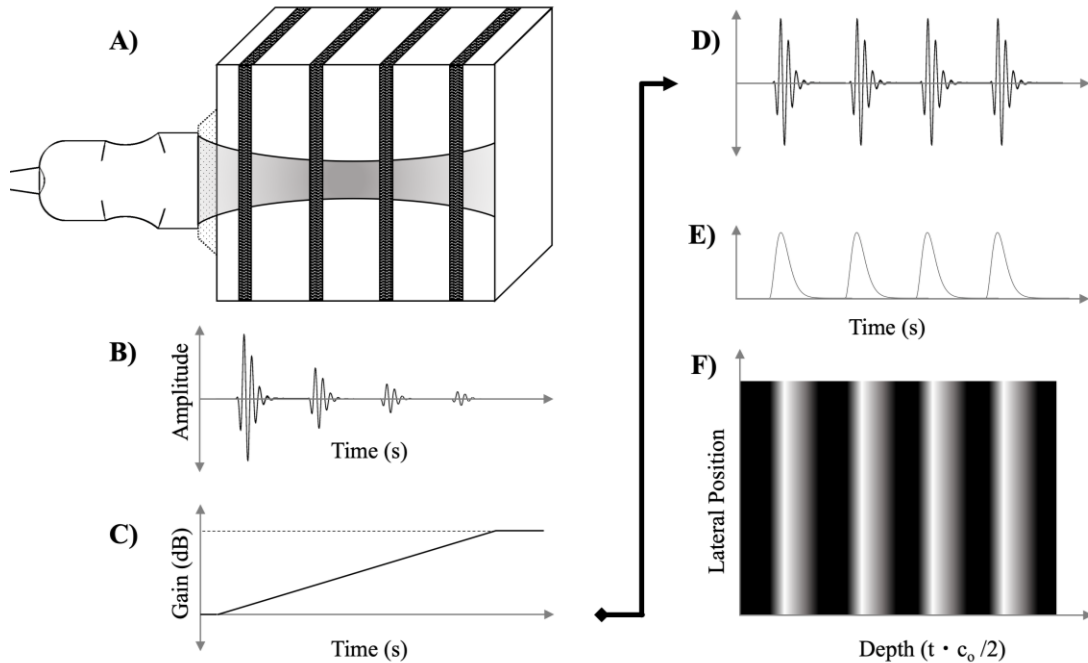
Figure 2-3: The process of image generation where a transducer images a body containing four equally spaced acoustic reflectors of equal echogenicity. (A) The transducer produces a scan line through the tissue. (B) Acoustic signals logarithmically attenuate as they propagate through tissue and the echoes show attenuation with increasing depth. (C) Amplification applied to the received signal. (D) The resulting time-gain compensated signal. (E) Signal envelope. (F) Adjacent scan lines are plotted to form a two-dimensional image. Log compression is applied to the plotted image, allowing for the visualization of weak reflectors in the same image space as strong reflectors. This image has adapted elements from (Bushberg and Boone 2011).

The fundamental principles and underlying processes needed for the generation of two-dimensional brightness mode (B-mode) images are discussed in the follow sections (2.2.2 to 2.2.8) in further detail.

2.2.2 ECHO SIGNAL STRENGTH

The intensity of the returned echo is a function of the initial pulse intensity, the attenuation of the acoustic wave propagating in tissue, and the acoustic properties at the reflective boundary or structure. Acoustic impedance is a characteristic mechanical property dependent on a tissue's density and the speed of sound within it. For a plane wave in an inviscid material, the acoustic impedance (Z_o) is given by Equation (2-3), (Szabo 2004):

$$Z_o = \rho_0 c_0 \qquad (2\text{-}3)$$

15

where ρ_o is the density of the material, and c_o is the speed of sound in that material. The speed of sound in a tissue can be measured directly by measuring the propagation time t of a pulse across a known distance d, or it can be determined from other mechanical properties of the tissue (Szabo 2004):

$$c_0 = \frac{d}{t} = \sqrt{\frac{\beta}{\rho_o}} \tag{2-4}$$

where β is the material's bulk modulus, relating the amount of pressure seen in a material for a given level of strain. The refraction of an acoustic pulse at an interface between two tissues is illustrated in Figure 2-4.
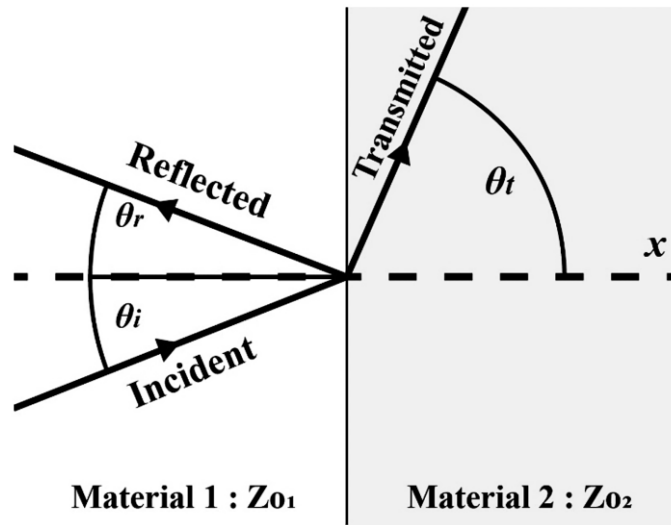
Figure 2-4: Geometric conventions describing the relative portions of the wave that are reflected and transmitted when a wave is incident on a boundary between two materials of different acoustic properties. When incident on a boundary, a wave may be fully reflected, fully transmitted, or it may be partially transmitted and partially reflected as determined by the equations below. This image was adapted from Figure 16-5 of (Bushberg and Boone 2011)

Equation (2-5) gives the reflected pressure ratio R_{pr} of reflected sound pressure p_r to incident pressure p_i when a sound wave encounters a boundary between two materials of different acoustic impedances (Z_{o1} and Z_{o2}) (Cobbold 2006). Where θ_i is the incident angle as measured from the line normal to the boundary surface on the incident side, and θ_t is the transmission angle.

$$R_{pr} = \frac{Z_{o2}\cos(\theta_i) - Z_{o1}\cos(\theta_t)}{Z_{o2}\cos(\theta_i) + Z_{o1}\cos(\theta_t)} = \frac{p_r}{p_i} = \left.\frac{Z_{o2} - Z_{o1}}{Z_{o2} + Z_{o1}}\right|_{\theta_{i,r}=0°} \tag{2-5}$$

Equation (2-6) gives the transmitted pressure ratio T_{pr} of transmitted sound pressure p_t to incident pressure p_i (Cobbold 2006):

$$T_{pr} = \frac{p_t}{p_i} = \frac{2Z_{o2}\cos(\theta_i)}{Z_{o2}\cos(\theta_i) + Z_{o1}\cos(\theta_t)} = \left.\frac{2 \cdot Z_{o2}}{Z_{o2} + Z_{o1}}\right|_{\theta_{i,t}=0°} \tag{2-6}$$

The relationship of the ratio of reflected pressure to transmitted pressure is given by:

$$R_{pr} = T_{pr} - 1 \tag{2-7}$$

The transmission angle θ_t of the acoustic wave for a given incident angle θ_i follows the acoustic version of Snell's law (Cobbold 2006):

$$\theta_t = sin^{-1}\left(\frac{c_{o2} \cdot sin\,\theta_i}{c_{o1}}\right) \tag{2-8}$$

Generally, echoes of the transmitted pulse will reflect from a boundary at a level that is proportional to the differences in acoustic properties between the layers. Transitions between similar materials, such as layers of muscle, will have weaker echoes than transitions between dissimilar layers, such as muscle and blood.

2.2.3   TIME-GAIN AMPLIFICATION

During pulse-echo imaging, an ultrasonic beam insonifies a line in the field of view (Figure 2-3.A). Time-gain signal amplification conditions the received echoes by amplifying proportionally to the echo's depth. Time-gain amplification compensates for the depth-dependent attenuation, ensuring that reflectors of equal reflectance produce the same amplitude (and brightness) in the resulting image at all depths.

As a wave travels through tissue, it experiences attenuation from the effects of absorption, scattering, and dispersion (Cobbold 2006).

- Absorption is the loss of energy from an acoustic wave due to the heating of the medium. The heating results from the frictional forces between oscillating particles within the acoustic wave.
- Scattering is the loss of energy due to the unorganized deflection of acoustic energy away from the wave path. This effect is typically due to small reflectors that interact with only a portion of the wave.
- Different frequencies of sound waves attenuate at different rates where attenuation increases with frequency. This frequency-dependent attenuation produces a downshift in the signal's frequency and reduces the amplitude of the signal's intensity envelope.

Equation (2-9) gives a good approximation of acoustic attenuation, where α is the amplitude attenuation coefficient. $\bar{I}(x)$ is the signal intensity, $\bar{I}(0)$ is the signal intensity at $x=0$, and x is the pulse propagation distance (Cobbold 2006).

$$\bar{I}(x) = \bar{I}(0) \cdot e^{-2\alpha x} \tag{2-9}$$

Additionally, the amplitude attenuation coefficient at a given frequency is a function of frequency, f, and the material, where both n and α_o are related to the material properties and temperature, and are available in reference tables based on experimental data (Cobbold 2006).

$$\alpha = \alpha_o f^n \tag{2-10}$$

Equation (2-10) shows that as the frequency increases, the acoustic signal attenuates faster. Therefore, the depth of detectable echoes is reduced at higher frequencies, thereby shortening the probe's penetration depth in high-frequency applications. Time gain amplification compensates for the effects of attenuation by amplifying echo signals by an amount proportional to its depth. However, the attenuation is exponentially proportional to frequency and so increases rapidly with frequency. Once the signal is below the system's noise floor, time-gain amplification is no longer effective, and so the amount of compensation that can be applied is limited.

All ultrasound systems have an inherent level of noise that is captured with the received signal. This noise remains relatively constant for all signal depths. With time-gain amplification, the noise amplifies along with the signal of interest. Therefore, despite time-gain amplification providing visual compensation for depth-related signal attenuation, the signal-to-noise ratio still decreases with depth. Thus, the maximum imaging depth remains at the depth where echoes are weaker than the system's noise floor.

2.2.4 DEMODULATION – SIGNAL AMPLITUDE DETECTION

Ultrasound systems must demodulate, or envelope-detect, the returned radio frequency (RF) signal to obtain the signal intensity for display. The return signal *v(t)* contains two parts: the carrier signal and the echo intensity signal. The carrier signal is a function of the resonance frequency of the transducer, represented in Equation (2-11) by *cos(2πft)*. The echo intensity signal *a(t)* is a function describing the amplitude of the reflections, from acoustic impedance differences:

$$v(t) = a(t) \cdot cos\ (2\pi f t\ +\ \phi) \tag{2-11}$$

where *f* is the center frequency of the transducer pulse, and ϕ is the phase shift of the pulse relative to a reference cosine wave. Demodulation (shown in Figure 2-5) separates the echo intensity signal, *a(t)*, from the carrier signal, *cos(2πft)*, when performed on the return signal, *v(t)*. Frequency shifts in the demodulated carrier signal correspond to Doppler shifts (frequency shifts due to tissue motion). The echo intensity signal *a(t)* is plotted to display the tissue characteristics.
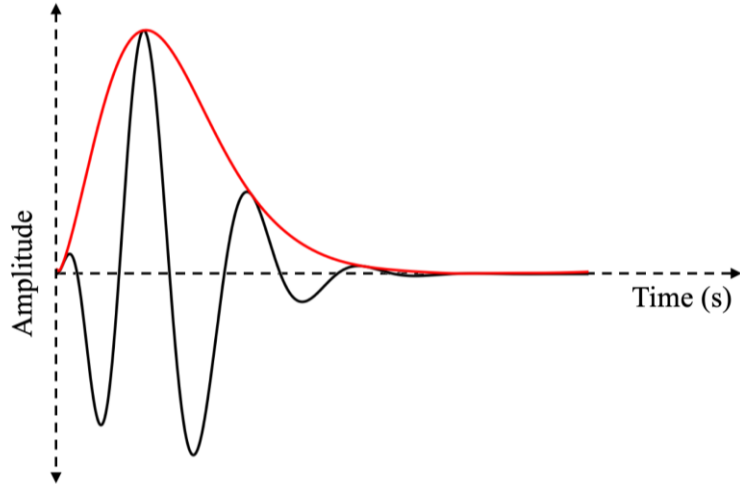
Figure 2-5: The solid black line shows a characteristic pulse-echo of a broadband transducer, *v(t),* and the red line shows the envelope of the signal *a(t)* given from the Hilbert transform of *v(t).*

The demodulated signal can be found from the returned RF echo by several different techniques:

- **Signal rectification and low-pass filtering:** this is a hardware-based solution that can be implemented directly in circuitry. However, it can only be applied after receive beamforming of the signal.

- **Hilbert transform:** this method provides a simple software solution for envelope detection, but requires some computational power, potentially lowering the frame rate.

- **I-Q (In-phase and quadrature) demodulation:** is a method that trades off envelope accuracy for reductions in computational processing.

Both Hilbert transformation and I-Q demodulation were used in this body of work. I-Q demodulation reduced the sampling rate requirements of the digitized ultrasonic signals, as per the method described in (Samson, Bezanson, and Brown 2017).

Both the Hilbert transform, and I-Q demodulation techniques are common approaches used in ultrasonic imaging systems. The Hilbert transform returns a complex dataset where the magnitude of the signal is the signal envelope, and the imaginary part gives the signal

phase. The magnitude of the Hilbert transform of a signal *v(t)* is shown below in Equation (2-12):

$$a(t) = |H\{x(t)\}| = |\frac{1}{\pi}\int_{-\infty}^{\infty}\frac{v(\tau)}{t-\tau}d\tau| = |v(t) * \frac{1}{\pi t}|$$

(2-12)

where *a(t)* is the envelope of the signal and is equal to the convolution of the echo signal with $1/\pi t$. The red line in Figure 2-5 shows the Hilbert transform of a characteristic ultrasonic pulse (black line), where the pulse is modeled using Equation (2-13) from (SanEmeterio and Ullate 1992):

$$v(t) = C \cdot t^3 \cdot \cos(2\pi f t) \cdot e^{-kft}$$

(2-13)

where *C* represents a proportionality constant, the variable *t* represents time, *f* is the transducer's resonance frequency, and *k* is a bandwidth factor that can be adjusted to raise or lower the bandwidth of the pulse. The pulse shown in Figure 2-5 is a pulse modeled with a -3 dB bandwidth of 50%, which corresponds to k = 3.84 in Equation (2-13). A more detailed discussion of pulse bandwidth is presented in section 2.2.6.

I-Q demodulation is an alternate method for envelope detection and is described by:

$$a(t) = \sqrt{I^2 + Q^2}$$

(2-14)

where, *I* represents the discrete value of *v(t)* at time *t*, and *Q* is the value of *v(t)* with a 90-degree phase shift about the pulse center frequency. The I-Q demodulation technique, however, incurs artifacts on broadband pulses due to the presence of constituent frequencies in the signal.

The advantage of I-Q demodulation is apparent when considering waveforms sampled at less than ten samples per wavelength. Figure 2-6 shows the signal envelope produced by both the Hilbert transform (dotted line) and I-Q demodulation (red line) when sampling at four samples per wavelength. The plots show that the Hilbert transform is more sensitive to the timing of signal samples, in relation to the signal peak, than I-Q demodulation. In this example, the misalignment of samples causes a decrease in the Hilbert transform peak estimation of approximately -3 dB. To increase the precision of Hilbert transform during envelope detection, the signal must be upsampled to more than ten samples per wavelength,

which can lead to a frame rate reduction in computationally limited systems. I-Q demodulation trades reduced computational demand for errors associated with sample timing precision and signal bandwidth.
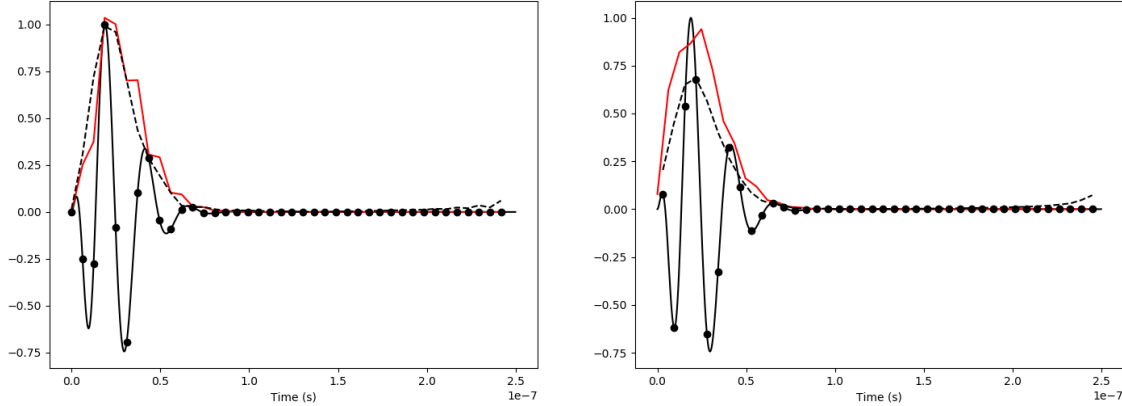
Figure 2-6: The above figures show a comparison of I-Q demodulation (red) and Hilbert transform (dashed) when capturing a 40 MHz pulse at four samples per wavelength. Though both functions work well when the samples capture the signal peak (left plot), the Hilbert transform does not work well when digitization fails to capture the peak signal. The circular markers indicate the digitized values on the signal waveforms

Both the Hilbert transform and I-Q demodulation techniques were used in this thesis; I-Q demodulation is used for processing images in Chapters 3 and 4 where computation resources were limited. The Hilbert transform was used in Chapter 5 when a more advanced beamformer was completed and computational advancements allowed for the more accurate processing technique.

2.2.5 LOG-COMPRESSION AND DISPLAY (GREY-SCALE MAPPING)

Medical ultrasound systems have a large signal range, whereby the intensity of the measured echo signals may vary by up to a factor of 10,000 (80 dB) or more. This large dynamic range needs to be displayed on computer monitors, which typically have a low dynamic range. Logarithmic compression effectively amplifies weak signals while attenuating strong signals, thereby persevering detail in both (Bushberg and Boone 2011). Though there are several methods of compression (Xiao et al. 2018), Equation (2-15) gives a typical form of logarithmic compression:

$$f(t) = 20 \cdot \log\left(\frac{v(t)}{(noise\ floor)}\right) \tag{2-15}$$

where $f(t)$ is the log-compressed version of the signal, $v(t)$. Typically, the range of displayed values are referenced to the system's noise floor. This provides an absolute dynamic range (DNR) for the RF signals, Equation (2-16):

$$DNR = 20 \cdot \log\left(\frac{maximum\ measureable\ signal}{noise\ floor}\right) \tag{2-16}$$

Figure 2-7 below, shows a comparison of a signal plotted on a linear scale and the same signal plotted on a logarithmic scale. The signal is quantified into 2^{10} bins (left) to simulate the effects of signal digitization, and this sets the dynamic range of 60 dB (right). The comparison of signal intensity plots, shown in Figure 2-7, exemplifies the normalization characteristics of logarithmic compression.
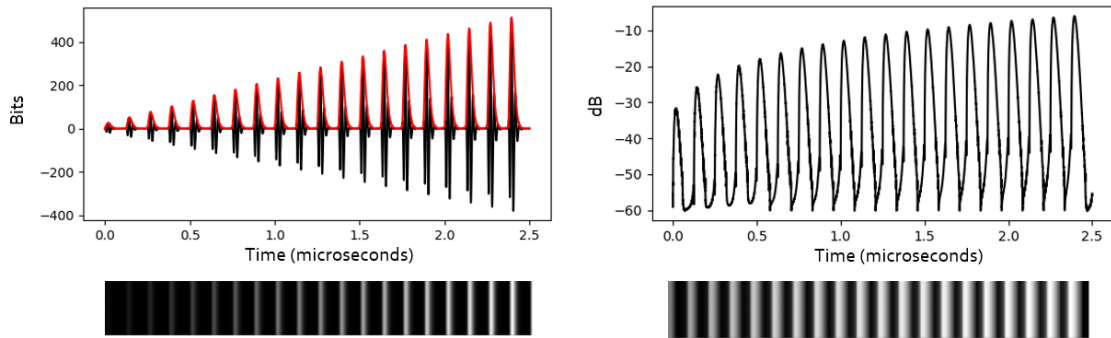
Figure 2-7: Figure showing the intensity plots of equivalent sets of data plotted on linear (left) and logarithmic (right) scales. The logarithmic compression allows for improved visualization of the characteristics of both weak and strong signals.

In general, logarithmic compression is a method that allows for signals of significantly different amplitudes to be displayed on a device with a limited dynamic range. It avoids the saturation of strong reflectors on the display while also allowing for better visualization of weak reflectors.

2.2.6 SPATIAL RESOLUTION

The acoustic beamwidth emitted from an unfocused single element transducer will remain at approximately the same width as the transducer, with a small amount of passive

focusing, and then begin to diffract and de-focus as it crosses the near-field far-field transition point (Bushberg and Boone 2011). Figure 2-8.A illustrates this effect.
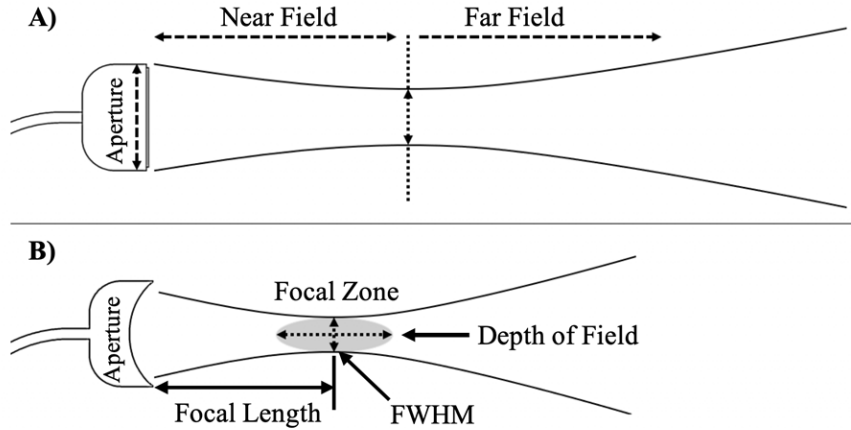
Figure 2-8: Comparison between the radiated pressure fields of (A) an unfocused planar transducer with a circular cross-section (aperture) and (B) a geometrically focused transducer (Bushberg and Boone 2011)

The near field length is a function of the transducer's aperture (d) and pulse wavelength, as described in Equation (2-17). The length of the near field is given by:

$$Near\ field\ length = \frac{d^2}{4\lambda} \tag{2-17}$$

For a focused transducer, the radiated pressure reaches a peak at its geometric focus. The focal zone of a transducer corresponds to the area in the transducer's pressure field where the acoustic pressure is within 50% of the peak pressure, and falls in the region around the focus, as shown in Figure 2-8.B. The lateral resolution of the transducer is defined as the width of the region where the signal intensity is within 50% of the peak signal pressure. The beamwidth (full-width half-max, FWHM) value for a spherically focused transducer is given by:

$$Lateral\ Resolution = \ 1.4\lambda \cdot \frac{F}{D} \approx 1.4\frac{\lambda a}{D} \tag{2-18}$$

where F is the transducer's focal length and is approximately equal to the geometric radius of curvature of the transducer a. The diameter of the transducer aperture is represented by D. The ratio of focal length to diameter is commonly referred to as F-number ($F_{\#}$):

$$F_\# = \frac{Focal\ Length}{Aperture} \tag{2-19}$$

The focal depth defines the axial region where the ultrasonic beam provides high spatial resolution. The focal depth corresponds to the distance along the pulse axis, where the pulse pressure is within 50% of the peak pressure seen at the focus. The depth of field Z_F of a geometrically focused transducer is given by:

$$Z_F = 7.2\lambda \cdot (F_\#)^2 \tag{2-20}$$

Focusing an ultrasonic pulse improves lateral resolution. However, there is a trade-off between resolution and depth of field. Resolution can be increased (beamwidth decreased) by either decreasing the F-number or decreasing the wavelength. Decreasing either will also decrease the depth of field or the axial distance covered by high spatial resolution. In general, focusing improves the system's resolution and signal to noise ratio (Cobbold 2006). Focusing can be accomplished by:

- **Geometric Focusing:** the transducer surface is curved such that the acoustic energy is focused to a specific location, as shown in Figure 2-8.B. Geometric focusing involves locating all points of the transducer such that wave-fronts emitted from each location on the transducer will arrive at the focus at the same time. In practice, a spherical geometry with a radius centered on the focal point will provide the desired geometric focus.
- **Lens Focusing:** an acoustic lens is used to focus the sound towards the focal point, just as a lens is used to focus light.
- **Beamformed Array Focusing:** an array of elements on a transducer (Figure 2-9.B) is excited at different times such that the propagating wave-fronts arrive at the focus at the same time.
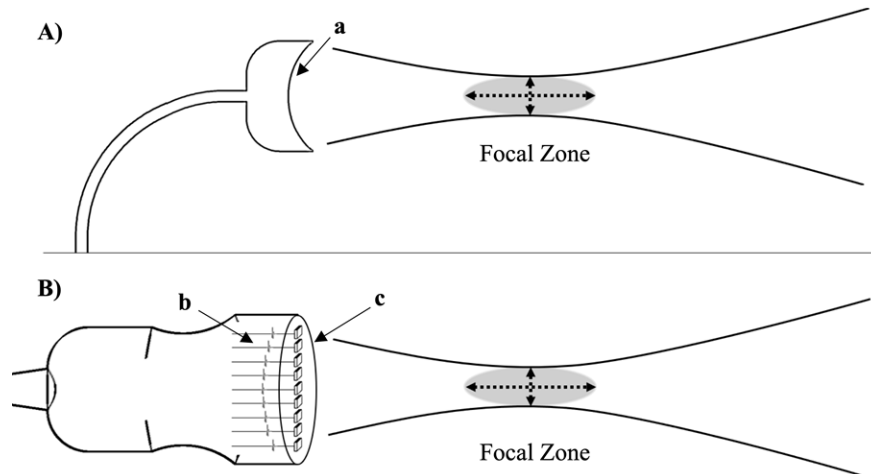
Figure 2-9: (A) A geometrically focused single-element transducer. (B) A linear array transducer. Both focusing techniques can produce a similarly shaped acoustic pulse, however, the linear array achieves this through beamforming and the location of the focal point can be adjusted. Each element (c) of the linear array can be controlled independently and the pulses timed (b) such that all pulses arrive at the focal zone at the same time.

An array-based transducer, such as that shown in Figure 2-9.B, has several advantages over a conventional single element transducer. The main advantage of these arrays is that they can adjust the position of the acoustic focus by adjusting the delay profile of the electronic excitation pulses. Therefore, with array transducers, there is no trade-off between resolution and depth of field. For an array transducer to emulate the focus of a spherically shaped transducer, a receive delay profile is required. This receive delay profile is inserted into the received channel data after the signals are digitized but before demodulation and signal processing.

Linear arrays and phased arrays allow for the scan lines to be adjusted laterally, thereby allowing for adjacent scan lines to be captured and stitched into a two-dimensional image without any motion of the transducer. Since the transducers remain stationary during the acquisition of a two-dimensional image, they can produce higher frame rates and typically avoid artifacts arising from the motion of the imaged tissue or the transducer.

The Rayleigh resolution criterion quantifies the resolution of an ultrasonic transducer. It defines the resolution of a device as the minimum center to center spacing between two point reflectors where they still appear as distinct entities (Cobbold 2006). By definition,

this point is where the acoustic pulse is within 3 dB of the peak pulse pressure for a transmit-only event, or where the acoustic pressure is within 6 dB of the peak pulse pressure for a two-way (transmit and receive) event. The formula for the resolution of a beam generated by beamforming an array transducer corresponds to the FWHM equations determining lateral and axial resolution. The lateral resolution is estimated by Equation (2-18), and the axial resolution is estimated by Equation (2-21).
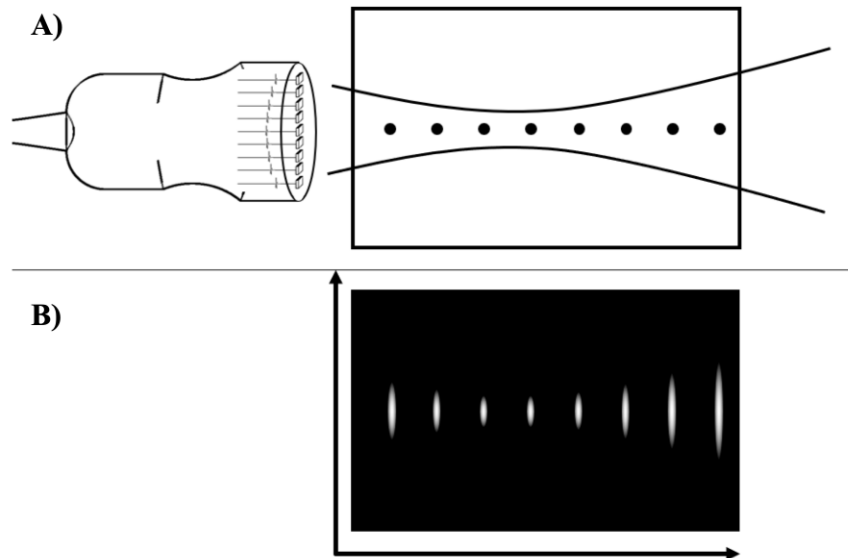
Figure 2-10: This illustrative figure shows the loss of lateral resolution as the imaged reflectors move farther from the transducers focus. A) shows a linear array transducer imaging multiple equal reflectors in a medium, while, B) shows the resulting image for a capture with only one focal depth.

Figure 2-10 shows the variation in the lateral point spread function (PSF) for various point targets located at different depths. Array transducers will typically scan the same line a few times at different focal depths and stitch them together to achieve a higher and more consistent lateral resolution throughout the field of view. The resolution has two factors, axial resolution, and lateral resolution. Axial resolution is measured along the axis of the pulse propagation and depends on the pulse frequency and bandwidth. Lateral resolution is the FWHM value of the beamwidth at the focus.

The bandwidth of a pulse relates to the total width of the frequency spectrum of the pulse. Broader bandwidth pulses correspond to a shorter envelope and hence increased resolution. Examples of narrowband versus broadband pulses are shown in Figure 2-11.
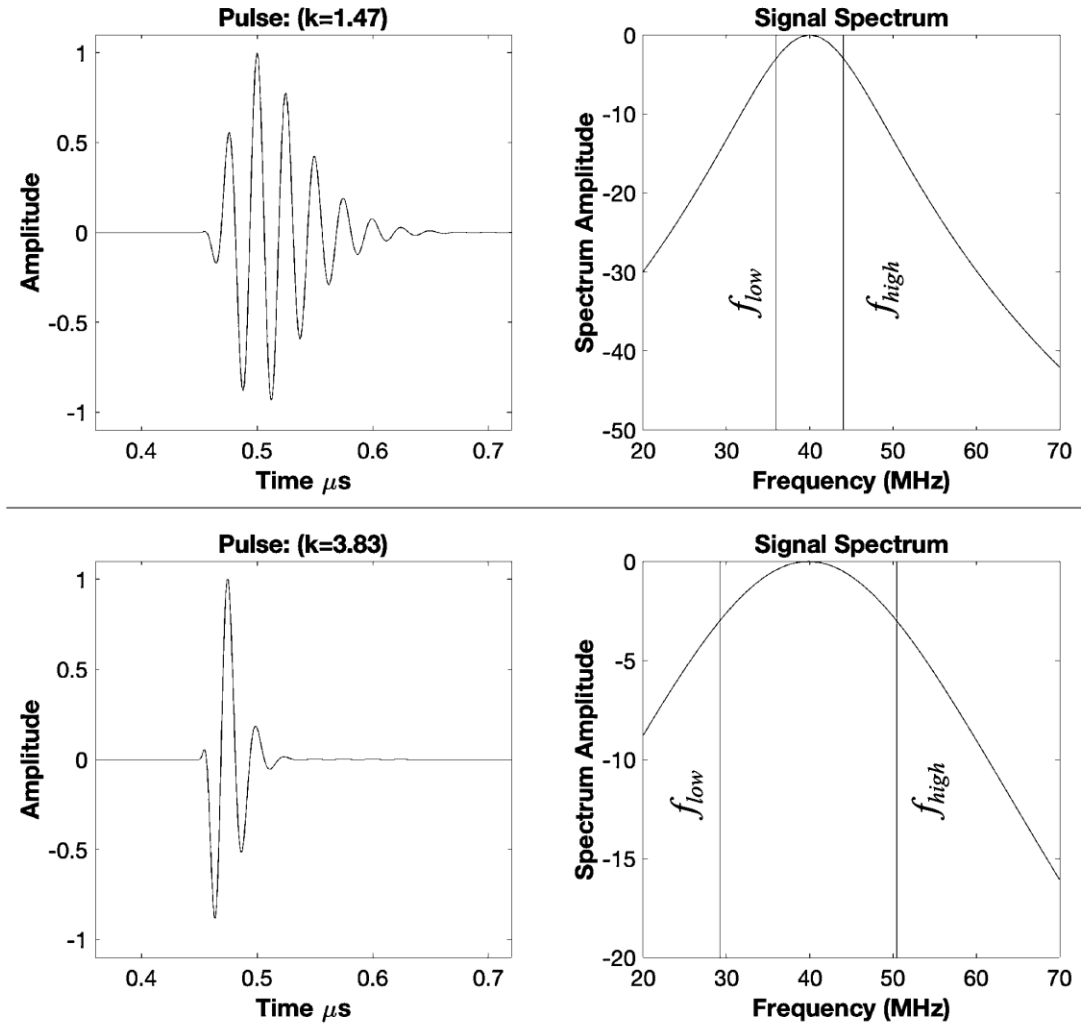
Figure 2-11: (Top) 20% -3dB bandwidth pulse contrasted against (Bottom) a 50% -3 dB bandwidth pulse. Both pulses have the same pulse frequency. The lower bandwidth pulse rings for a longer time and as such results in a longer axial pulse envelope and degrades axial resolution. Both pulses have a center frequency, f_c, of 40 MHz.

The bandwidth of a pulse is defined by Equation (2-21):

$$Bandwidth\ (-3dB) = \frac{f_{high} - f_{low}}{fc} \qquad (2\text{-}21)$$

where f_{high} is the upper -3 dB threshold of the pulse spectrum while f_{low} is the lower -3 dB threshold of the pulse spectrum and f_c is the pulse center frequency. By convention -3 dB bandwidth thresholds are used in this work when referring to one-way signals and -6 dB bandwidth thresholds are used when referring to two-way signal bandwidths.

For the pulse modeled by Equation (2-13) the axial resolution is approximated by:

$$Axial\ Resolution \approx \frac{1}{3.5} \cdot \frac{\lambda}{BW\%} \tag{2-22}$$

where the proportionality constant of 1/3.5 is experimentally determined and is a function of the distribution of the modeled pulse. For Equation (2-21) the above approximation gives an error of <5% when compared to the simulated resolution over the range of 5% bandwidth up to 90% bandwidth. However, both axial resolution and lateral resolution are highly dependent on the quality of construction of the transducers and so Equations (2-21) and (2-18) are only used as a general reference during design.

2.2.7   B-MODE IMAGING

As described in the preceding sections, conventional pulse-echo imaging begins by capturing information along a one-dimensional scan line called an A-line. Multiple adjacent A-lines are captured and stitched together to produce a two-dimensional image, referred to as a brightness mode (B-Mode) imaging. The following sections discuss the most common methods of two-dimensional image generation from adjacent A-lines.

Single element transducers: These differ from array-based transducers in that they need to be mechanically scanned to generate the adjacent A-lines. There are two common modes of translation for these transducers, linear translation (Figure 2-12.A below) or rotational translation (Figure 2-12.B). The combination of rotational translation and a single element transducer is common for intravascular imaging, where the rotational translation covers a full 360° sector from inside the artery.

Annular array transducers: Similar to single element transducers, these transducers require mechanical translation in order to generate parallel image lines that make up the B-

mode image. These arrays, however, do not have the same trade-off as single element transducers since they can be beamformed along the central axis of the annular rings.

Linear arrays: Linear arrays consist of a long line of linear elements, and the focused beam is generated from a sub-aperture of these elements. Linear arrays generate image lines perpendicular to the surface of the transducer and collect parallel image lines by multiplexing the sub-aperture down the long row of elements. Since the translation does not require mechanical translation, higher frame rates and smaller packaging can be achieved. Figure 2-12.C depicts the collection of parallel A-lines during conventional linear array imaging.

Linear phased arrays: As with linear arrays, phased arrays (also called 'linear phased arrays') consist of a linear arrangement of ultrasonic elements. The main difference is that instead of multiplexing a sub-aperture of elements, phased arrays steer the adjacent scan lines electronically. Phased arrays allow the field of view to span a much larger spatial region than the transducer aperture itself. Figure 2-12.D illustrates how a phased array generates a sector-shaped B-mode image by collecting scans lines at different steering angles.
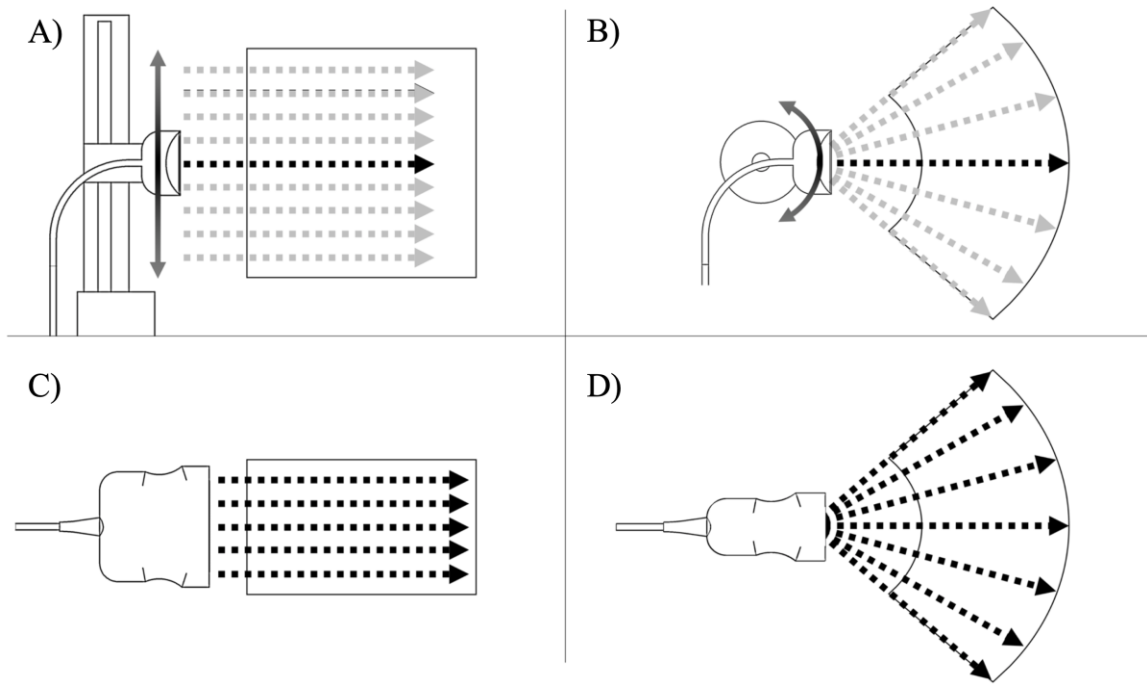
Figure 2-12: Methods of 2D image generation. A) Linear mechanical scanning, B) mechanical rotation, C) linear array with sub-aperture scanning, D) phased array with beam-steering. Though a typical ultrasonic transducer will only be able to image one image line at a time, multiple methods exist that allow the beam to be scanned and a 2D image formed. For mechanically translated transducers, this is achieved by sequential acquisitions and physical motion. For linear and phased arrays, beamformed pulses focus the ultrasonic pulse along a new vector.

For an endoscopic imaging system, a phased array transducer presents a promising solution, as in endoscopic applications, maintaining a small package size is critical to the success of the device.

2.2.8   ELEVATION FOCUSING

Both linear and phased arrays inherently lack focusing in the elevation (slice thickness) dimension. An acoustic lens is typically applied to obtain an elevation-focused 2D image slice. Therefore, the elevation focus involves a trade-off between lateral resolution and depth-of-field, as discussed above in section 2.2.6. Typically, priority goes to depth-of-field over resolution, and the elevation lens will usually have an f-number between 4 and 5. The elevation lens material is usually chosen to have an acoustic impedance matched to the imaged tissue to avoid any reflections. In low-frequency systems, this lens is usually

made from a room temperature vulcanizing (RTV) silicone material with a lower speed of sound than tissue and hence a convex shape. In high-frequency designs, the rubber is usually too attenuating, and so a low-density plastic or resin is usually implemented with a concave shape. A simple method for approximating the effective beam focus, F, is given by Equation (2-23), (Maréchal et al. 2004):

$$F = \frac{R_c}{(1 - n)} \tag{2-23}$$

where, R_c, is the radius of curvature on the lens, and n is the velocity ratio between the lens and water. The effective focus, F_e, of the lens is more accurately solved for by using the formula given by Equation (2-24) as discussed in (Maréchal et al. 2004).

$$F_e = \frac{F}{1 + \left(\frac{2}{3}\right)\left(\frac{\lambda F}{a^2}\right)^{\frac{4}{3}}} \tag{2-24}$$

where a is the elevation aperture and λ is the ultrasonic wavelength in tissue and F is given by Equation (2-23). A more detailed discussion of this topic is presented in Appendix D.

2.3 ACOUSTIC FIELD MODELING – IMPULSE RESPONSE METHOD

The Diffraction Impulse Response technique has proven to be a powerful technique for the simulation of the acoustic fields emitted by ultrasonic transducers and arrays. In Huygens' Treatise on Light (Huygens 1690), he set the basis for the impulse response technique by describing the behavior of a wave as the sum of an infinite number of wavelets (Huygens Principle).

For the acoustic version of the impulse response function, the impulse response function allows for the determination of the resulting acoustic pressure $p(\bar{x},t)$ at a point P in the medium (see Figure 2-13). Where point P has displacement $\bar{x}$ from the element, resulting from the velocity based excitation $v(t)$ of a transducer element (SanEmeterio and Ullate 1992).
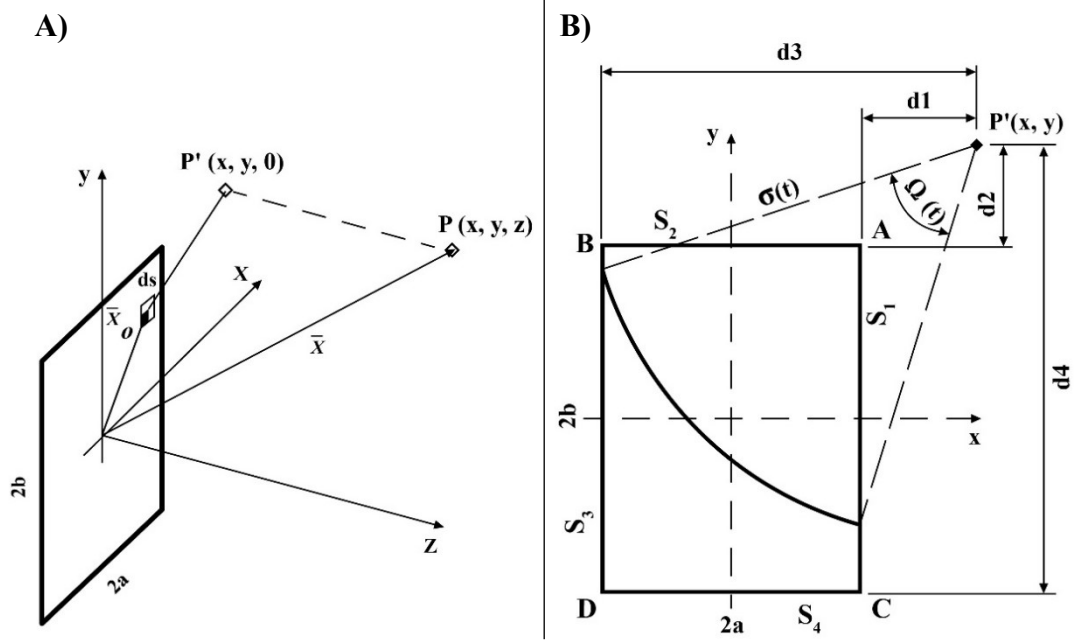
Figure 2-13: (A) Coordinate system for impulse response of a rectangular transducer. (B) Depiction of vectors and angles used in calculation when projected onto the z = 0 plane of the transducer. Image is redrawn based on the work presented in (SanEmeterio and Ullate 1992)

The resulting pressure is given by the convolution of the time-based derivative of the element's excitation signal $v(t)$, and the diffraction impulse response $h(\bar{x},t)$:

$$p(\bar{x}, t) = \rho \cdot \frac{\partial[h(\bar{x}, t) * v(t)]}{\partial t} \tag{2-25}$$

Where the impulse response $h(\bar{x},t)$, is the two-dimensional spatial convolution of the aperture function and the Green's function for the transducer's boundary conditions. The impulse response $h(\bar{x},t)$ at a horizontal displacement $\bar{x}$ from the excitation source is given by Equation (2-26) where $\beta(z,t)$ is the obliquity factor and solves to a value of two (Robinson, Lees, and Bess 1974), due to the rigid baffle condition associated with the rigid body of the transducer surrounding its elements:

$$h(\bar{x}, t) = \frac{\beta(z, t)}{4\pi} \cdot \oint_{S} \frac{\delta(t - |\bar{x} - \bar{x}_0|/c)}{|\bar{x} - \bar{x}_0|} dS \tag{2-26}$$

The simplified form of $h(\bar{x},t)$ for a planar transducer, solves to:

$$h(\bar{x}, t) = c \cdot \Omega(\bar{x}, t) \tag{2-27}$$

33

where $\Omega(\bar{x},t)$ is the sum of angles $\Gamma(t)$ in radians, falling within the active portion of the transducer at time t relative to the full circle about point $P'(x,y)$:

$$\Omega(\bar{x}, t) = \frac{\sum \Gamma(t)}{2\pi} \tag{2-28}$$

A simplified version of the methods presented by SanEmeterio et al. (1992), was developed in this work for the calculation of the $\sum \Gamma(t)$ values as only rectangular elements are used. The simplified method removes the need to use region dependent methods for the computation of $\sum \Gamma(t)$ that would otherwise depend on the location of $P'(x,y)$ relative to the excitation element. In this method, a circle is drawn about point $P'(x,y)$ of radius R at each time interval, where R is given by:

$$R = \sqrt{(c \cdot t)^2 - z^2} \tag{2-29}$$

The intersections of the circle with the $X1$, $X2$, $Y1$, and $Y2$ bounds of the rectangular element are then tabulated. The segments falling between intersections on the bounds of the element (where conditions $x_1 \leq x_i \leq x_2$ and $y_1 \leq y_i \leq y_2$ are true) are then calculated and summed as the values of $\Gamma(t)$. In the example shown in Figure 2-14, only segment $S5$ meets these criteria, and so $\Gamma(t) = \theta_{S5}$ with units of radians.

Figure 2-14: Simplified method of determining $\sum \Gamma(t)$ values. Though based on the circular test described by Jensen et al. (J.r.A. Jensen 1999), this test further simplifies the computational process for the calculation of the $\sum \Gamma(t)$ values.

Figure 2-15 shows the results of a simulation of the transient pressure waveform generated by a transducer element being excited by a waveform with a bandwidth of 50% ($k = 3.833$ in Equation (2-13) above) and a frequency of 3 MHz. These plots match Figure 11.A and Figure 11.C of (SanEmeterio and Ullate 1992) validating the calculation method. The simulation is run in a custom script, written in the Python programming language (Van Rossum and Drake 2011), using the calculation methods described above. The script is included in Appendix A as reference.

$h(\overline{x}, t)$ $\qquad$ $p_i(\overline{x}, t)$

Figure 2-15: Impulse responses (left) and transient pressure waveform (right) for a field point at $\overline{x}$ = (x,y,z) = (0,0,20) mm of a rectangular transducer of dimensions; width = 15mm and height = 24mm. The transient pressure waveform generated by the transducer element being excited by a pulse waveform with a two-way bandwidth of 50% and a frequency of 3 MHz.

The impulse response function described above allows for the calculation of the resulting pressure seen at an arbitrary point in the acoustic medium as imaged by an ultrasonic transducer. The model assumes acoustic pressure levels within the bounds required for linear propagation and summation. Our experimental work has demonstrated that, for the devices described in this work, acoustic pressure levels remain within linear thresholds. Additionally, by convolving the transient pressure field for a given point with the impulse response function for that point, the two-way radiation pattern is given, and the pressure returned to the transducer in an ideal acoustic reflection.

2.3.1 RADIATION PATTERNS

By iterating the calculations for the transient pressure levels through all points in the acoustic field of interest, it is possible to use the impulse response method to model the distribution of the acoustic energy in the imaged medium from an excited transducer element.

36
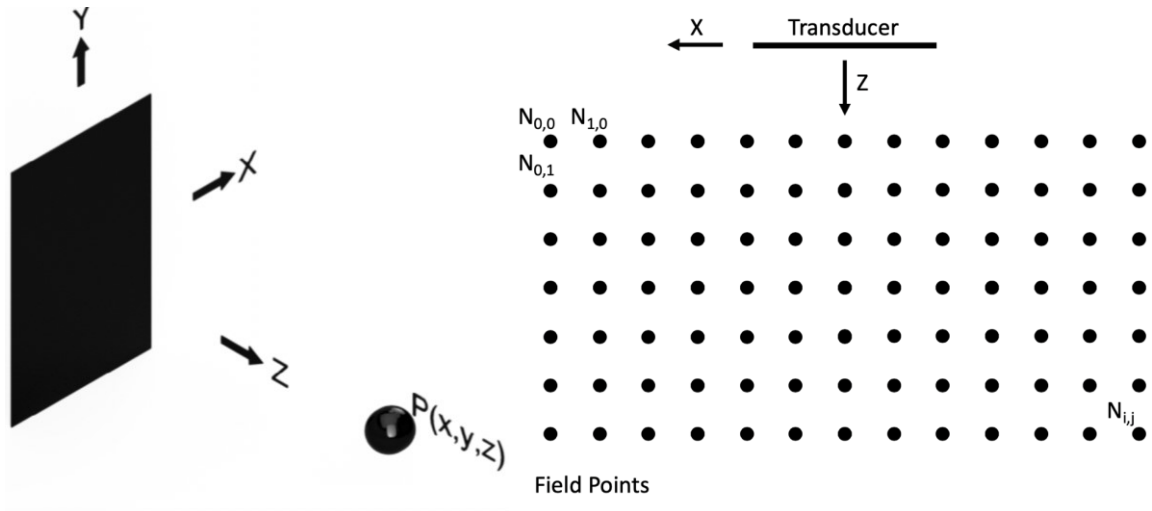
Figure 2-16: (Left) A 3D depiction of a field point P(x,y,z) in relation to an array element. (Right) A view of field points along the XZ plane representing grid points used in the simulation of two-dimensional radiation patterns

Figure 2-16 shows a coordinate system that has expanded on the single point of simulation (left) to one that includes a grid of points. When the acoustic field in front of the transducer for each spatial location, as illustrated in Figure 2-15, is modeled, we get the two-dimensional radiation pattern shown in Figure 2-17.

Figure 2-17 shows the peak value amplitude of the pressure envelope, at all time points for a field of interest, given the activation of a delay and summed set of element activations (beamformed pulse). The pressures from all active elements are linearly summed at each spatial location $P(\overline{x})$. Parameters such as the element dimensions, element beamforming delay, and the number of active elements can be modified to achieve the desired performance or to optimize the array for a given application.
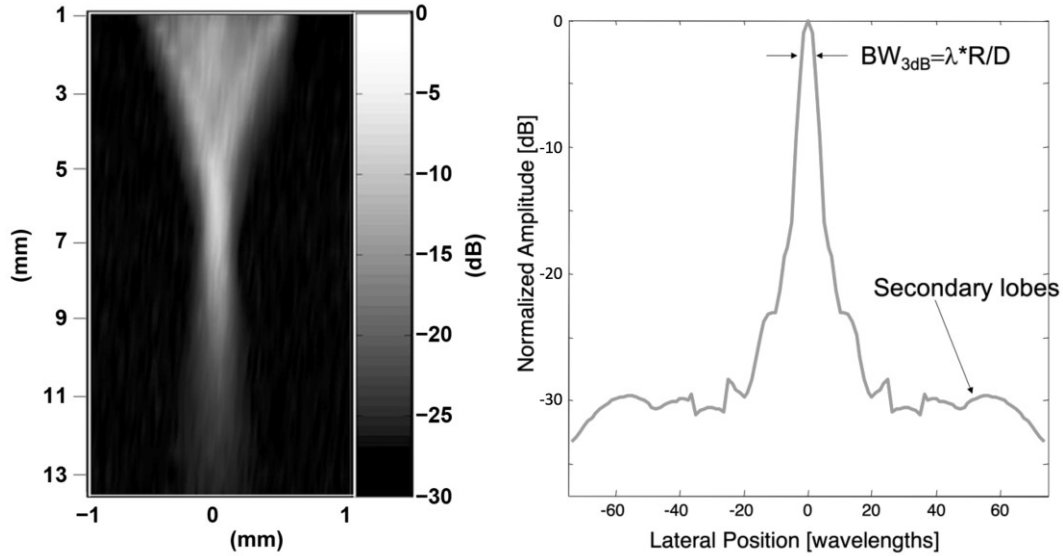
Figure 2-17: Characteristics of ultrasonic radiation of a beamformed pulse. (Left) shows the two-dimensional acoustic pressure field, with brighter areas showing regions that experience high acoustic pressures. (Right) shows the acoustic pressure taken along the y = 7mm focal depth of the two-dimensional plot.

As shown in Figure 2-17, cross-sectional slices of the acoustic radiation pattern are used to quantify parameters of the acoustic pulse related to image quality. These include beam-width (resolution), secondary-lobe levels (maximum dynamic range), and grating lobe levels (section 2.3.3).

2.3.2   ELEMENT DIRECTIVITY

This work presents the construction of ultrasonic phased arrays, therefore, the ability of the arrays to focus acoustic energy off to large angles is a critical performance metric. The directivity factor quantifies the ability of the array or its elements to transmit acoustic energy to wide angles. The directivity metrics are typically reported as the angles to which the two-way acoustic signal is within 50% (-6 dB) of the peak signal with no steering (θ = 0°). Alternatively, the directivities can be reported using acceptance angles, which are equal to the angular span between these points.

The impulse response model simulates the directivity from a transducer element using the method described above in section 2.3.1 However, the acoustic pressures are only computed for a fixed depth or radius from the element. When computing the directivity

38

function, the simulation reports the peak two-way echo envelope at each angle. This method contrasts against the radiation pattern simulations where the array focus is at a fixed point, and the simulations calculate the resulting pressures seen at the neighboring field points.
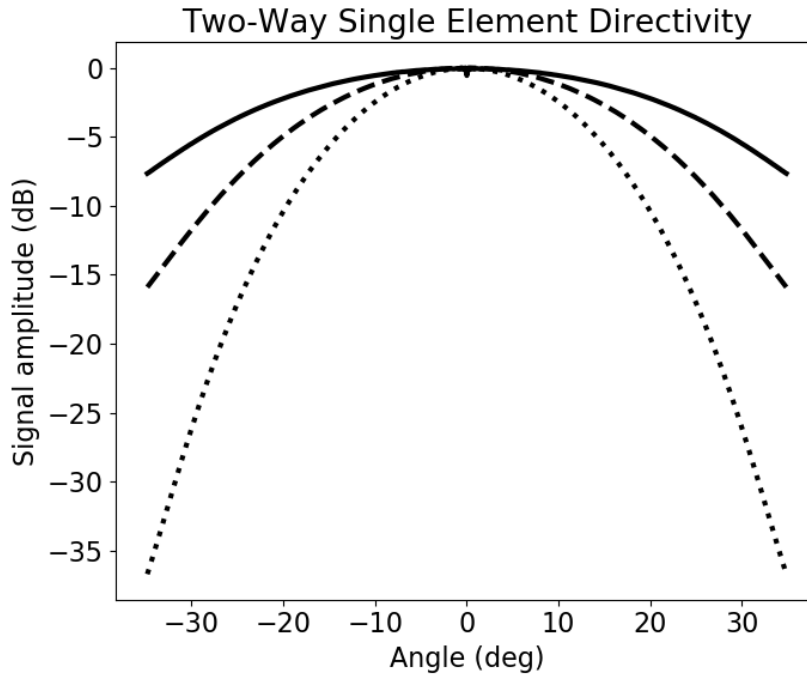
Figure 2-18: Impulse response simulations of the single element directivity of acoustic radiation from elements 55μm wide (dotted), 35μm wide (dashed), and 15μm wide (solid). Simulations used a center frequency of 40 MHz, a bandwidth of 20% and a focal depth of 6.5 mm.

The resulting plot of the angle-dependent signal amplitude is called the directivity plot. The single-element directivity is typically assumed to be a predictor of the beamformed directivity. However, the work presented in Chapter 5 suggests that this may not be a valid assumption in all cases. The simulation presented in Figure 2-18 shows several single-element two-way directivity plots, where the element width varies. A clear trend can be seen where thinner elements produce higher signal directivity.

2.3.3   GRATING LOBES

Grating lobes are an image artifact caused by the periodic nature of the array elements. As the pitch of the array increases, relative to the acoustic wavelength, the grating lobes

become stronger and occur at narrower angles. For sparse phased array transducers (where the pitch is greater than ½λ), the grating lobes can limit the width of steering angles that can be imaged. For a given pitch d, grating lobes will occur at the angle θ_i relative to the beamformed pulse (Thoen 1982):

$$\theta_i = \sin^{-1}\left(\pm \frac{\lambda}{d}\right) \tag{2-30}$$

Simulations are required to predict the amplitude of grating lobes, as their intensity is dependent on many factors such as focal depth, pulse bandwidth, element geometry, element count, and element pitch. These simulations are completed by using the impulse response function to compute the acoustic pressure seen within the imaged field when the pulse is focused to a specific angle. Figure 2-19 shows several illustrative examples of grating lobe simulations discussed in more detail in chapter 3. These simulations allow for the investigation of array parameters, such as the pitch of elements, and their effect on grating lobes.
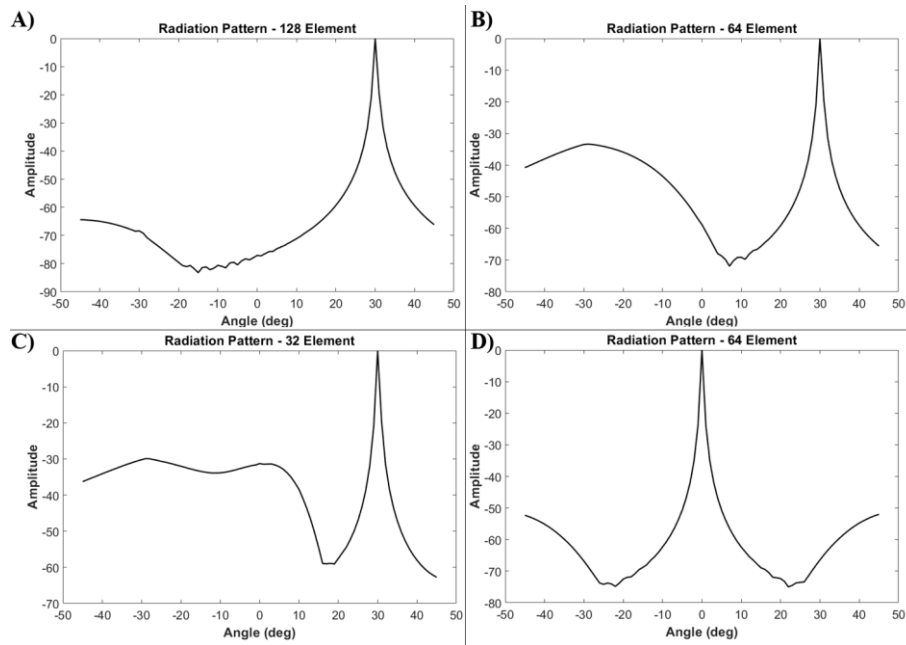
Figure 2-19: Simulation of grating lobes for various array patterns. (A) 128 element array at ½λ pitch. (B) 64 element array with 1λ pitch. (C) 32 element array at 2λ pitch. (D) 64 element array at 1λ pitch, focused to 0°. The signal peak at 30° represents the focused signal and the signal lobes around 0° to -40° represent the grating lobe

Figure 2-19 shows simulations of the radiation patterns produced by ½λ, 1λ, and 2λ element pitches. The simulations used a 50% two-way pulse bandwidth and an $F_\#$ of 2.5. From these figures, we can see that arrays with 128 elements at ½λ pitch have excellent performance. Arrays with 64 elements start to show significant grating lobes when the pulse is steered to the edge of the image (+ 30°). Yet, the grating lobes fall outside of the central region of the image window.

2.3.4 ELECTROMECHANICAL TRANSDUCER MODELING (KLM)

A typical transducer is shown in Figure 2-20. A typical transducer will include: coax cable, a backing layer that provides structural support to the transducer and acoustic damping, the piezoelectric element that generates the electromechanical transduction, and acoustic matching layers that aide in the transmission of the acoustic pulse into the tissue.
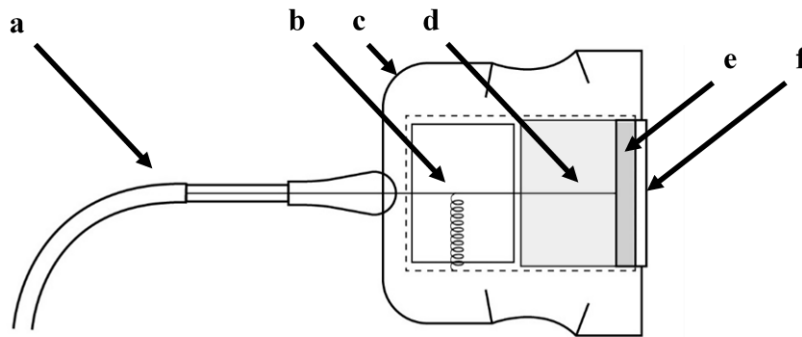
Figure 2-20: Standard components of an ultrasonic transducer. The acoustic array stack-up refers to the combination of backing layer, piezoelectric element, acoustic matching layers and lens. The housing is composed of a cable assembly (a), a ground connection to electrical shielding (b) and transducer body (c). The acoustic array stack-up refers to the combination of backing layer (d), piezoelectric element (e), acoustic matching layers and lens (f). This image is adapted from Fig 16-8 in (Bushberg and Boone 2011).

The design of the casing and ground shielding is typically based on general electrical design practice. The design aims to provide a functional device that meets the needs of the clinical environment with regards to the level of emitted electromagnetic energy and immunity to electromagnetic noise.

A primary challenge in the design of ultrasonic transducers is the matching of the acoustic properties of the high acoustic impedance piezoelectric ceramics and crystals to the low

impedance materials being imaged (water and tissue). In a method similar to electrical impedance matching in RF circuitry using electrical matching networks, acoustic matching layers can be used to match between the two very different acoustic impedances.

Theoretically, the matching layer between the two layers of different impedances can be matched with a quarter wavelength thick layer of impedance, Z_{o2}, given by:

$$Z_{o2} = \sqrt{Z_{o1}Z_{o3}} \tag{2-31}$$

where Z_{o1} is the acoustic impedance of the piezoelectric layer, and Z_{o3} is the impedance of the tissue. While this matching layer impedance maximizes the intensity transmitted at the center frequency of operation, it does not increase the bandwidth very effectively. Because of this, other studies have developed more complicated empirical models that consider bandwidth. A common acoustic impedance chosen for a single quarter wavelength matching layer is provided by Desilets et al. (1978):

$$Z_{o2} = \sqrt[3]{Z_{o1}Z_{o3}^2} \tag{2-32}$$

Additionally, the use of dual matching layers can further improve transducer performance by allowing for greater bandwidth and sensitivity of the transmitted acoustic waves (Qian and Harris 2014). According to Desilets et al. (1978), the optimal acoustic impedances for dual quarter wavelength matching layers are:

$$Z_{ML1} = \sqrt[7]{Z_{o1}^4 Z_{o3}^3} \tag{2-33}$$

$$Z_{ML2} = \sqrt[7]{Z_{o1} Z_{o3}^6} \tag{2-34}$$

where Z_{ML1} and Z_{ML2} correspond to the first and second quarter wavelength matching layers between the piezoelectric substrate (Z_{o1}) and tissue (Z_{o3}).

In high-frequency transducers, the feature sizes of the components are quite small, and it is challenging to apply thin films of materials reliably to the array stack. However, thin-film vacuum deposition techniques have been developed for the semiconductor industry and present an attractive option when compared to traditional lamination techniques (Brown et al. 2014). In this study, each matching layer is formed by the combination of a

soft springy material and a dense material. This combination creates a mass-spring resonance as opposed to the quarter wavelength resonant cavity (Brown et al. 2014; Toda and Thompson 2010)

One of the most effective methods of modeling piezoelectric elements is using the electrical lumped parameter model established by Krimholtz, Leedom, and Matthaei referred to as the "KLM model" (Krimholtz, Leedom, and Matthaei 1970). In the design of a transducer, many components need to be considered, such as the coaxial cable properties, the acoustic backing layer, and the matching layers. Conveniently, all of these additional elements can be easily represented by electrical components and integrated with the KLM model.

In this work, the acoustic array stacks were designed using a two-port KLM model based on the original work by Krimholtz et al., and improvements by Desilets et al. and Lockwood et al. (Desilets, Fraser, and Kino 1978; Lockwood and Foster 1994; Krimholtz, Leedom, and Matthaei 1970). Figure 2-21 shows a schematic diagram of the KLM electrical model of a piezoelectric element. The input port is on the electrical side at v3, and two mechanical output ports are representing the front (v2) and the back (v1) of the piezoelectric element. This 3-port model converts to a 2-port model by shunting off the backport with a backing layer load (represented by a resistor). Each matching layer connects to the front port; these are represented by mechanical transmission lines of a quarter wavelength. Following the matching layer transmission lines, the tissue models as a shunt resistor following the matching layer transmission lines.

$$CO = lw/(\beta_{33}^{\ S}\ t)$$

$$v\quad = v_l^{\ D} = (C_{33}^{\ D}/p)^{\frac{1}{2}}$$

$$Zo\ = plwv_l^{\ D}$$

$$\emptyset\ = (1/2M)\ cosec\ (tw/2v_t^{\ D})$$

$$X1 = Zo\ M^2\ sin\ (tw/v_t^{\ D})$$

$$M = h_{33}/(wZo)$$
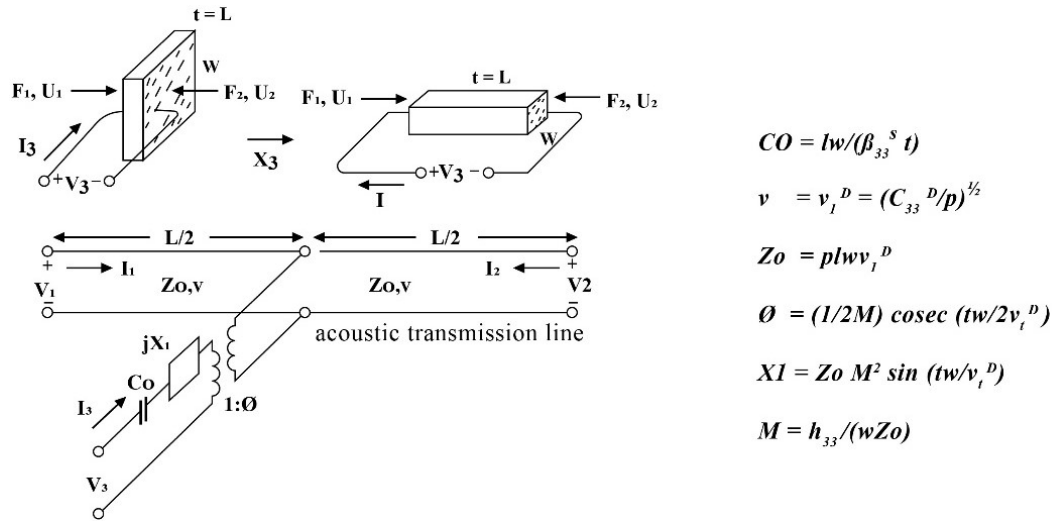
Figure 2-21: Equivalent circuit model for a thickness-expander plate (piezoelectric wafer) and length expander bar (piezoelectric composite). This is the KLM model diagram for the simulation of the acoustical performance of an ultrasonic transducer. This figure is a redrawing based on Fig. 2 in the publication "New equivalent circuits for elementary piezoelectric transducers" (Krimholtz, Leedom, and Matthaei 1970)

KLM transducer modeling can be a very effective method for designing matching layers for the optimization of bandwidth and sensitivity. Figure 2-22 shows the simulation of a transducer without a matching layer (top row), with a single quarter wavelength matching layer (bottom row). Simulations show the two-way pulse-echo received when excited with a monocycle electrical stimulation. These figures exemplify how the bandwidth and sensitivity increase with proper matching layer design. Sensitivity quantifies in terms of "insertion loss", which is the ratio of echo voltage over the electrical stimulation voltage.
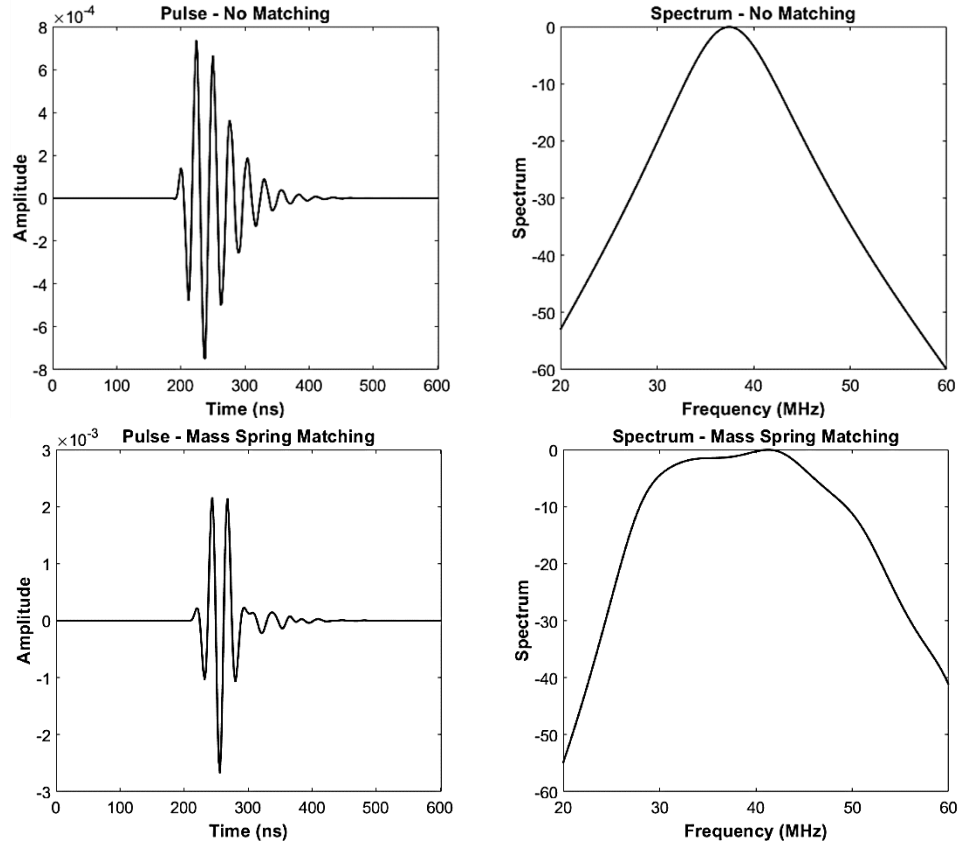
Figure 2-22: Shows the result of KLM simulations predicting the performance of a 49μm transducer with (top row) no matching layer, and (bottom row) a pulse from an array with dual-layer mass-spring matching configuration

Figure 2-22 shows the predictive power of the KLM model and simulates the performance of a transducer element using different matching layer techniques. From the plots, we see that a dual-layer mass-spring matching layer obtains nearly an order of magnitude better sensitivity, and improves the transducer's bandwidth from 25% to 45%.

2.4 FABRICATION OF HIGH-FREQUENCY TRANSDUCER ARRAYS

High-frequency ultrasonic arrays generate higher resolution images than low-frequency arrays and can, therefore, resolve finer tissue structures. However, for ultrasonic arrays, these advantages come at the cost of increased fabrication complexity, higher signal attenuation (decreased imaging depth), and greater demands on the electronics of the ultrasonic system. Specifically, the electrical system must provide higher precision in terms of the timing of pulse transmission and signal acquisition events. Additionally, the amount of data

45

collected per unit time increases proportionally to the frequency, and so the computational hardware required for signal conditioning and image display experiences increased demands.

However, the advantages of high frequency ultrasound are compelling enough to justify the development of commercial systems (L.W. Wang et al. 2018), and the establishment of research groups working to utilize these advantages (Lucas et al. 2014).

2.4.1 METHODS OF HIGH-FREQUENCY ARRAY ELECTRICAL INTERCONNECTION

One of the most critical areas of design in the development of a high-frequency array is the electrical interconnect. The electrical interconnect technique directly effects:

- The overall package size of the transducer
- The bond-yield, where an ineffective process will produce arrays with many elements that cannot be activated electrically (dead elements)
- Parasitic components or resistances, that dampen the acoustic output of the transducer

Wire-bonding: The work presented in (Brown et al. 2007) and (Foster et al. 2000) present a technique whereby an array is wire-bonded to a flexible circuit board, with copper traces layered on a polymer membrane. After the bonds are completed, the assembly of the piezoelectric wafer, wire-bonds, and the circuit board's bonding pads are locked in-place using an epoxy. From here, the electrical interconnect is bent back and fitted within the transducer housing.

Anisotropic Solder: In addition to wire-bonding techniques, anisotropic conductive epoxies have been used (Jonathan M Cannata et al. 2011; Schiavone et al. 2017; A.L. Bernassau et al. 2009). In these techniques, the piezoelectric wafer is aligned over a flexible circuit board with fine electrical traces. The connection between the array elements and the traces is then completed using an anisotropically conductive epoxy. Where the epoxy contains small pillars of conductive material (silver metal) that is cured under a magnetic field that causes the conductive pillars to align in the direction between the transducer die and the traces on the flexible printed circuit board interconnect. The pillars are designed to be

narrow enough so that they cannot connect between elements, and the magnetic field must be strong enough to ensure that all pillars are oriented correctly.
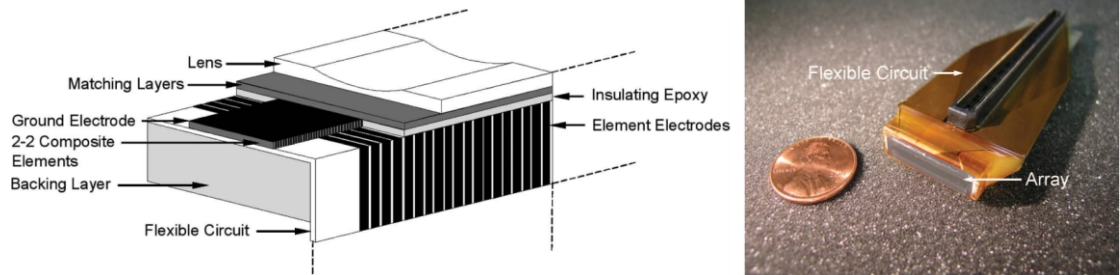
Figure 2-23: (Left) Internal view of transducer showing the electrical interconnection method connecting the cable assembly to the array stack. (Right) Packaging technique required to fit the interconnect within a transducer housing. Images obtained from Fig 4 and Fig 6 of (Jonathan M Cannata et al. 2011) figures reprinted with permission

Sputtering Interconnect: Another technique for the application of electrical bonds between the transducer array stack and the interconnect is detailed in (Jonathan M Cannata et al. 2006) and is shown in Figure 2-23. The interconnect is aligned with the piezoelectric substrate, and a sputtered layer of metal completes the electrical connection.

Fanouts to electrically bonded wires: Another technique commonly seen on experimental arrays in the literature (A. L. Bernassau et al. 2012; Liu et al. 2012) is the completion of electrical interconnects by fanning out the array pattern to a larger solderable area. Though this technique does not appear to be practical for commercial fabrication, it has the advantage of allowing for a quick design iteration and the facilitation of testing.

Electrode Patterning: At frequencies of 30 MHz and below, scratch dicing of a conductive electrode can produce viable electrodes. However, at higher frequencies, the features become smaller, and techniques must allow for the fan-out of the electrode patterns to achieve reliable electrical interconnections. As such, above 30 MH, laser etching of the electrode or photolithographic electrode processing can be used to produce the required patterns and bonding surfaces.

2.4.2 HIGH-FREQUENCY ARRAY CONSTRUCTION

An essential factor in the fabrication of a high-frequency transducer is the fabrication of the piezoelectric layer on which the electrical elements are defined. The simplest piezoelectric layer to construct is a kerfless piezoelectric wafer that is fabricated by dicing a block of the piezoelectric material to the desired size, lapping to the required thickness, and then photolithographically patterning the desired array elements on the monolithic substrate. However, arrays based on unkerfed (kerfless) wafers show high levels of mechanical coupling between elements, which is considered to be detrimental to the performance of kerfless arrays in existing literature. In order to reduce crosstalk between elements, the piezoelectric substrate is typically cut or kerfed into a composite material so that neighboring elements remain mechanically isolated. Additionally, composites can alter the oscillatory mode of the piezoelectric wafer so that it changes from a monolithic plate-mode oscillator to a bar-mode oscillator (Figure 2-24.left), or a pillar-mode oscillator (Figure 2-24.right) (K. K. Shung, Cannata, and Zhou 2007) with higher electromechanical coupling (k_t) and a better impedance match to tissue.

2-2 Composite   1-3 Composite
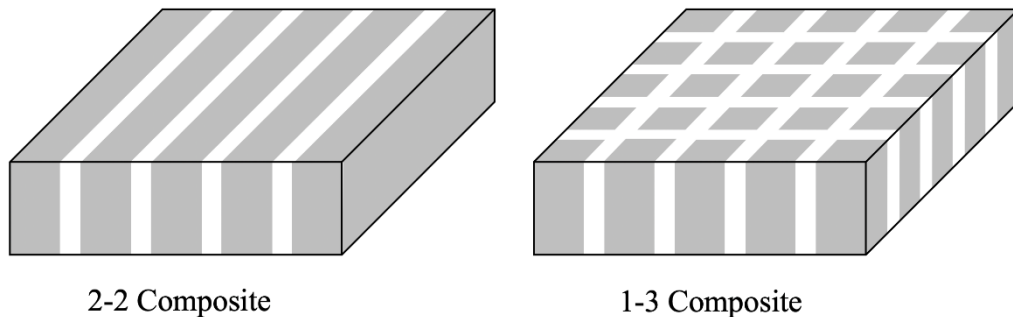
Figure 2-24: 2-2 composite (left) and 1-3 composite (right), the grey areas represent the piezoelectric material and the white areas represent the filler material (typically a soft epoxy).

The machining of the piezoelectric wafer to generate the mechanical isolation between elements presents a significant challenge since the kerfs need to be extremely fine in order to avoid lateral and spurious resonance modes within the operating band of the transducer. For high-frequency substrates, very fine kerfs are desired, on the order of 5-10 μm, and the pillars or strips of the remaining piezoelectric material can be very delicate.
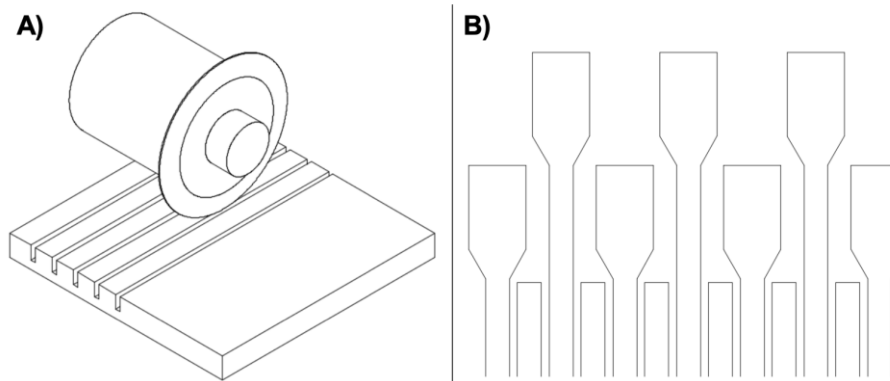
Figure 2-25: Isometric view showing the process by which a sample is diced for illustrative purposes. The width of the kerf is determined by the blade width, with 10μm blades being the smallest width available. A) The sample is fixed to a vacuum chuck, and dicing saw blade rotates at high-speed machining slots into the sample. A precision positioning stage controls the positioning of the sample relative to the blade allowing for a high level of accuracy in cut depth and position. B) Electrode fanout pattern from array elements to bonding pads.

Dice and Fill: The standard method of composite generation involves the dice and fill technique whereby the piezoelectric wafer has parallel kerfs cut into the surface at a defined pitch forming a 2-2 composite, as shown in Figure 2-25 and Figure 2-26. The kerfs are then filled with a soft epoxy to provide strengthening of the matrix and to allow for a continuous surface for the array's electrodes. If a 1-3 composite is desired, the wafer is rotated 90°, and the kerf/fill process is repeated. Though conceptually reasonably straightforward, the dice-and-fill technique has several limitations. Mainly, the kerfs must be linear and span from one end of the wafer to another, and the kerfs can only be as thin as the thinnest possible dicing saw blade of 10 μm (Disco, Japan). A 10 μm blade width is usually too large for high-frequency arrays. For example, a typical 40 MHz array might have an element pitch of 38 μm (1λ), and two strips of piezoelectric material are usually required per element to avoid lateral modes. This means that of the 38 μm element region, 20 μm will be removed, and additionally, the saw blades apply stresses to the piezoelectric material during cutting that cause micro-cracking that propagates a few microns laterally into the piezoelectric from the kerf. This micro-cracking can severely degrade the efficiency in converting electrical to mechanical energy since only a small percentage of active undamaged piezoelectric material remains.

49

2-2 Composite
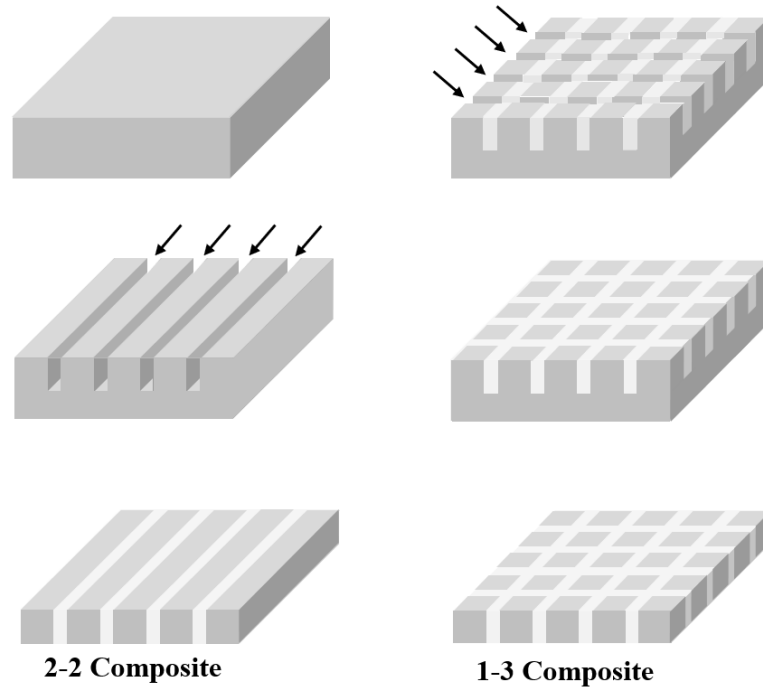
1-3 Composite

Figure 2-26: Dice and fill process whereby a 2-2 or 1-3 composite wafer is created. Wherein a bulk piezoelectric wafer is diced and the kerfs are filled with a soft epoxy. For a 1-3 composite, the wafer is rotated by 90° and the kerfs are redone along the orthogonal axis. The final wafers are inverted and lapped to thickness removing the unmachined portion of the wafer

Deep reactive ion etching (DRIE), alternatively, has provided a method of machining composite materials that allows for finer features than conventional dice and fill techniques (J. Zhang et al. 2015). In DRIE, photolithography is used to apply a mask to the piezoelectric wafer in areas that the designer wants to keep material. The wafer is then placed in a reactive ion etcher, where a plasma environment is created that etches the wafer's surface and removes material. The process doesn't physically stress the material to the same level as machining but requires careful design as the etching process is highly dependent on multiple factors (Ivan, Agnus, and Lambert 2012). Metallic masks are used to block the reactive plasma from etching the wafer where piezoelectric material is needed. This is usually a very long process and relatively expensive.

Laser micromachining is conceptually similar in many ways to reactive ion etching in that the piezoelectric wafer is etched by a non-mechanical method. However, the laser is focused on a small spot, and its position can be precisely controlled. Therefore, laser

micromachining does not require the application of a mask. Additionally, when compared to DRIE, laser micromachining is more convenient for rapid prototyping (Ivan, Agnus, and Lambert 2012), however the types of lasers required to machine lead-based ceramics, with this precision and no thermal damage, are quite costly.

Interdigitally bonded composites, as presented by Cannata et al (Jonathan M Cannata et al. 2011), utilize a construction method that helps to circumvent the traditional kerf-width limitations of the dice-and-fill technique. The two piezoelectric wafers are machined with pillars that fit into the kerfs of the other wafer; when the wafers are slotted and epoxied together, the remaining kerfs can be smaller than the width of a dicing saw blade.

Thin-film deposition and sintering techniques allow for the creation of the composite material at the same time as machining the wafer to the desired thickness and shape. Typical deposition techniques utilize suspensions of piezoelectric grains in an organic solvent that are spread onto a surface and baked to remove the solvent, thereby leaving only the piezoelectric material (M. Lukacs, Sayer, and Foster 2000). Additional methods, presented in (Pang et al. 2006) allow for the formation of kerfs in the deposited layers, allowing for the kerfing of annular arrays or the creation of composites. This technique allows for the production of thickness-controlled coatings and can avoid damage to the ceramic during the lapping process (M. Lukacs, Sayer, and Foster 2000).

Lapping is a conventional fabrication technique of grinding the wafer to a precise thickness. The use of lapping techniques is ubiquitous throughout fabrication focused literature related to ultrasonic devices. For the fabrication of high-frequency transducers, finer slurries with lower removal rates allow for greater thickness control and minimize surface damage. The thickness of a piezoelectric substrate controls its oscillatory frequency, and so the lapping process must be undertaken with care.

Vacuum deposited thin-film matching layers allow for the acoustic matching layers to be deposited using vacuum deposition techniques, as described in (Brown et al. 2014); the use of vacuum deposition bypasses standard bonding techniques that involve the application of adhesive layers, which can further degrade transducer performance and add unwanted acoustical effects.

Composite piezoelectric wafers, as described in the previous section, also allow for improved sensitivity of the ultrasonic transducer, resulting in increased transmission pressures and higher sensitivity with regards to received signals.

For the fabrication of miniaturized high-frequency ultrasonic arrays reactive ion etching, and laser micro-machining techniques stand to provide the highest resolution featuring of piezoelectric wafers. However, both these techniques are associated with high equipment and processing costs. In this work multiple array construction techniques are utilized with the most advanced construction method involving laser micro-machining and vacuum deposited acoustic matching layers. Though the laser micro-machining is effective, the work presented herein also developed techniques to produce semi-kerfed and kerfless arrays that reduced or removed the need for some of the most challenging micro-machining stages associated with endoscopic arrays. These techniques allow for reduced manufacturing costs, improved yields, and in the case of kerfless arrays, they may also allow for secondary imaging modes with a larger field-of-view.

2.5 SUMMARY

Minimally invasive surgical procedures require a high-resolution endoscopic device that can provide depth-resolved images from an endoscopic form factor. Recent developments in high-frequency ultrasonic array technologies present a unique opportunity to realize a device that satisfies the desirable goal of endoscopic applications. However, there are significant challenges associated with the development of such a device that this work addresses in the subsequent chapters. Specifically, this work addresses the fabrication or machining of the micro-scale transducer elements and the miniaturization of a high-frequency array into an endoscopic form factor. Miniaturization of such an array requires a novel electrical interconnect solution, as well as a trade-off between packaging size, number of elements, image resolution, and sensitivity.

CHAPTER 3:

DESIGN, FABRICATION AND PERFORMANCE EVALUATION OF A 40 MHZ ULTRASONIC PHASED-ARRAY ENDOSCOPE

In this chapter, a 40-MHz, 64-element phased-array transducer, packaged in a 2.5 x 3.1 mm endoscopic form-factor, is discussed. The array was a forward-looking semi-kerfed design based on the piezoelectric single-crystal of composition (Pb(Mg$_{1/3}$Nb$_{2/3}$)O$_3$–32%PbTiO$_3$), commonly referred to as PMN-PT. The PMN-PT substrate was patterned with an element-to-element pitch of 38 μm. A novel technique of wire-bonding the array elements to a polyimide flexible circuit board was developed to achieve a miniaturized form-factor. The circuit board was oriented perpendicular to the forward-looking ultrasound beam, thus reducing the overall package size.

A technique of partially dicing into the back of the array was implemented to improve the directivity of the array elements (semi-kerfing). The array was fabricated with a single layer of poly(vinylidenefluoride-co-trifluoroethylene) (P(VDF-TrFE)) as an acoustic matching layer and a polymethylpentene (TPX) lens for passive elevation focusing to a depth of 7 mm. The two-way -6 dB pulse bandwidth was measured to be 55%, and the average electromechanical coupling (k_{eff}) for the individual elements was measured to be 0.62. The one-way directivities from several array elements were measured to be ± 20°, which was shown to be an improvement over an identical kerfless array. The -3 dB elevation focus resulting from the TPX lens was measured to be 152 μm at the focal depth, and the focused lateral resolution was measured to be 80 μm at a steering angle of 0°.

To generate beam profiles and images, the probe was connected to a commercial ultrasound imaging platform which was reprogrammed to allow for phased array transmit beamforming and receive data collection. The collected radiofrequency (RF) datasets were then

processed offline using a numerical computation script to generate sector images. The radiation pattern for the beamformed transmit pulse was collected along with images of wire phantoms in water and tissue-equivalent medium with a dynamic range of 60 dB. Finally, ex vivo tissue images were generated of porcine brain tissue.

3.1 PREAMBLE

This chapter is primarily based on my first peer-reviewed journal article (Bezanson, Adamson, and Brown 2014) and includes information from the conference proceedings (Bezanson, Adamson, and Brown 2013; Bezanson et al. 2012), all works were published through the UFFC division of IEEE. This chapter is a mostly unaltered replication of the journal article but has been updated to remove information already presented in Chapter 2. Some additional content has been added to the final discussion section to lay the investigative foundation for the following chapters.

3.2 INTRODUCTION

In recent years, there has been significant progress in developing fully sampled, forward-looking high-frequency linear-array transducers (Ritter et al. 2002; Jonathan M Cannata et al. 2006; Brown et al. 2007; J. Cannata, Williams, and Shung 2005; Yang et al. 2012; J. M. Cannata et al. 2008; Carey et al. 2009; Wu et al. 2009; Marc Lukacs et al. 2006; Q. Zhou et al. 2010; Liu et al. 2012; Jin et al. 1998) with some groups developing complete imaging systems (Foster et al. 2009; Bantignies et al. 2011; L. Zhang et al. 2010; Hu et al. 2010; Sun et al. 2007; Wygant et al. 2005). Although the elements are of conventionally proportioned dimensions in these linear arrays, the overall packaging of the transducers is still relatively large because the array aperture must be as large or larger than the desired field-of-view and substantial space is required for the array interconnect, thus limiting the application of these arrays to topical use in which images are generated from outside the body.

As previously discussed, there are many applications in which high-resolution ultrasound images are desired from a probe with a small endoscopic form-factor (e.g., intravascular, laparoscopic, surgical guidance, auditory, etc.), which are better suited to a phased-array transducer (Pederson et al. 2010; Yeh, Oralkan, Ergun, et al. 2005; Midtbø et al. 2012;

Dausch et al. 2008; Yeh, Oralkan, Wygant, et al. 2005; Dauchy and Dorey 2007; D. Zhou et al. 2011; Zipparo et al. 2008; Yeh et al. 2006). Although there has been commercial success in the development of phased arrays packaged into an endoscopic form-factor, such as the AcuNav (Acuson Corp., Mountain View, CA), ImageMate (EP Med Systems Inc., West Berlin, NJ) and ViewFlex™ (St Jude Medical, St Paul, MN) (Silvestry and Wiegers 2005; Stephens et al. 2009), these systems and other experimental systems have been either lower in frequency (Pederson et al. 2010; Dausch et al. 2008; Zanchetta et al. 2002; Z. Wang et al. 2005) or in the form of a sparsely sampled ring array (Yeh, Oralkan, Ergun, et al. 2005; Midtbø et al. 2012; D. Zhou et al. 2011; Demirci et al. 2004).

We have demonstrated that using the central 64 elements of a 50 MHz linear-array probe (MS700, Visualsonics Inc., Toronto, ON, Canada), high-quality fully sampled phased-array images can be generated with an element pitch close to 1λ (Torbatian et al. 2010; Torbatian, Adamson, and Brown 2012; Torbatian et al. 2011) by using an appropriate grating lobe suppression technique, as described in (Stephens et al. 2009). Because this previously established element pitch is acceptable for phased-array imaging within a $\pm 35°$ field-of-view, the largest remaining challenge in building a practical high-frequency phased array is to reduce the packaging of the array and interconnects into a miniaturized endoscopic form-factor.

This study presents novel fabrication techniques for the construction of miniaturized high-frequency phased arrays in endoscopic form-factors, along with a thorough characterization of an array's performance. A novel technique of wire bonding the array elements to the thickness dimension of flexible circuit boards was used to reduce the interconnect size, and a semi-kerfed technique was used to increase the element directivity and maximum beam-steering angle. Electrical tests were conducted to determine the element impedances and crosstalk levels. Three-dimensional radiation patterns were collected with a needle hydrophone, and phantom targets were imaged along with ex vivo tissue as a final step in the characterization process.

3.3 ARRAY DESIGN

As mentioned, during a previous study (Torbatian et al. 2011), we were able to successfully generate high-quality phased array images with the central 64 elements of the MS700, a 40 to 50 MHz linear array transducer, and the Vevo 2100 system (FUJIFILM VisualSonics, Toronto, Canada), provided our grating lobe suppression technique was used (Torbatian et al. 2010; Torbatian, Adamson, and Brown 2012; Torbatian et al. 2011).

The results of that study were used as a guide for designing our phased-array endoscope transducer. Because we had already verified that we could generate phased-array images with linear-array pitch, we decided to use a similar array pitch and element count in our phased-array endoscope design to maintain a relatively large aperture for good lateral resolution. Only 64 elements were used to minimize the overall size of the probe. We desired an elevation focus at 7 mm, because this depth is applicable to a wide range of endoscopic imaging applications (e.g., intra-cardiac, neurosurgical, laparoscopic, surgical guidance, auditory, etc.). The elevation aperture was calculated based on an elevation f-number of 4.5 (within the conventional range of elevation f-numbers). After considering trade-offs between probe size, resolution, channel count, and slice thickness, the final design was chosen to be 64 elements at 38 µm pitch, 45 MHz center frequency, and 1.5 mm elevation aperture. A single 12 µm polyvinylidene fluoride-trifluoroethylene P(VDF-TrFE) matching layer was selected as the quarter-wavelength matching layer. Krimholtz-Leedom-Matthaei (KLM) models were run with this design and predicted an on-resonance electrical impedance magnitude of $80\,\Omega$, impedance phase of $0°$, a pulse center frequency of 45 MHz, and a fractional bandwidth of 50%.

The final feature of our phased array is the selection of $0.68\text{-Pb}(Mg_{1/3}Nb_{2/3})O_3\text{-}0.32PbTiO_3$, also known as (PMN-32%PT), as the piezoelectric substrate. Although the Ms700 transducer, which was based on a lead zirconate titanate ceramic (PZT-5H), produced good quality pulses with no lateral modes; this is a result of the MS700 array elements being sub-diced. Noting that the lateral frequency coefficient N_{31} of PZT-5H is approximately 1400 Hz·m and the thickness-mode frequency coefficient is $N_T = 2000$ Hz·m, non-sub-diced PZT-5H array elements that are 28 µm wide (10 µm kerfs at 38 µm pitch)

will exhibit a lateral mode for the individual elements at approximately 50 MHz, which is well within the operating band of a 45 MHz thickness mode.

As our manufacturing capabilities for diced array stacks are limited to 10 µm wide kerfs, therefore, we were not able to sub-dice our 28 µm elements because this would leave insufficient active element area and drastically reduce sensitivity. Although PMN-32%PT has a very similar N_T to PZT-5H, it has a nearly three times lower N_{31} ($\sim$700 Hz·m provided by manufacturer). For our desired element dimensions, this puts the lateral resonance of array elements made from PMN-32%PT at 25 MHz, which is below the operating band of a 45 MHz thickness mode. This feature makes use of PMN-32%PT as a key element in the success of our phased array design because it removes the need for sub-dicing the array elements.

$$f_c = \frac{N_t}{thickness} \qquad (3\text{-}1)$$

It should be noted that N_T is only an approximation of the thickness-mode frequency coefficient for a semi-kerfed array element and that N_{33} could also have been a valid approximation. N_T represents the thickness mode expander coefficient, and N_{33} represents the length mode expander coefficient that would have been used for a fully kerfed array composite. Equation (3-1) gives the relation between thickness, expansion coefficient and oscillation frequency. The required thickness can then be solved for a given frequency given tabulated values for N_T or N_{33}. As an operating frequency of 45 MHz was desired a wafer thickness of 49 µm was used.

3.4 FABRICATION

The fabrication process began by chemically etching the electrodes off a 10 mm x 10 mm x 150 µm substrate of PMN-32%PT single crystal (APC International ltd., Mackeyville, Pa). The sample was then lapped down to 140 µm to provide a uniform surface for photolithography. Photolithography was performed on the surface of the lapped substrate using a standard lift-off process to create 12 individual array patterns on a single 10 x 10 mm substrate. The array patterns consisted of 64 linear array elements that were 28 µm wide (38 µm pitch). Each of the elements fanned out to staggered wire bonding pads in a manner

very similar to a previously investigated linear array design (Brown et al. 2007). After the photoresist was developed, a 1.2 μm layer of aluminum was sputtered onto the substrate, and the remaining photoresist was dissolved with acetone, leaving a set of twelve 64-element electrode patterns (the electrode pattern is shown in Figure 3-1.B).
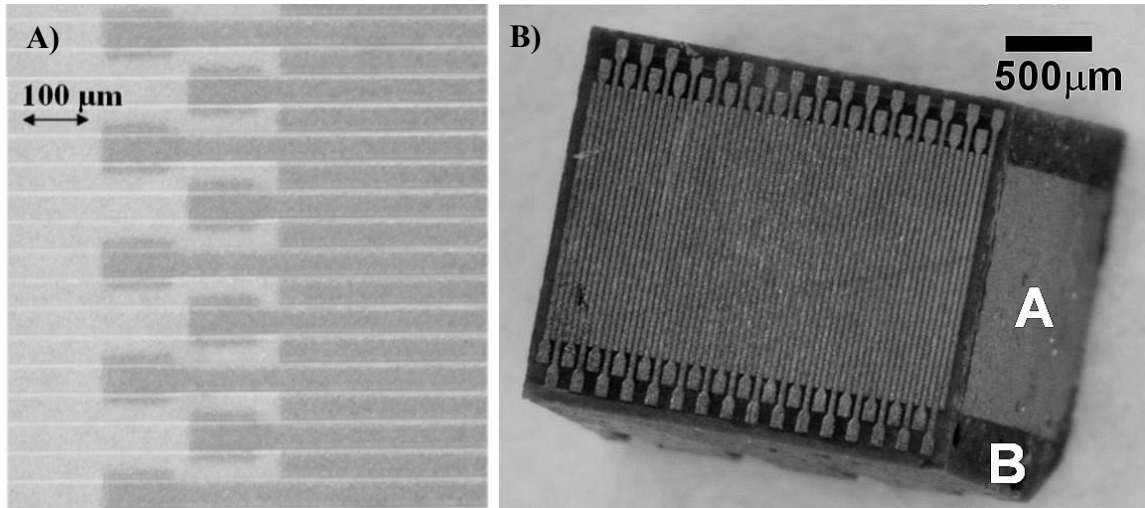
Figure 3-1: A) Kerf alignment over element pattern. The transparency of the thin PMN-PT crystal allows for alignment of the kerfs with the electrode pattern on the opposite side of the wafer. B) Photograph of one of the individual arrays with a backing layer. Section A represents the conductive backing and Section B shows a nonconductive and acoustically attenuating material that forms the backing material under the array bonding pads.

The substrate was then mounted on a glass carrier plate with the array patterns facing down and the substrate was lapped to a few micrometers more than the final thickness of 47 μm. A micro dicing saw (DAD3202, disco Technologies, Tokyo, Japan) was used to cut 10 μm wide semi-kerfs, 20 μm ± 3 μm deep into the back of the substrate, opposite the element electrodes. The cuts were carefully made such that they were aligned between the element electrodes located on the opposite side. Figure 3-1.A shows a photomicrograph of a section of the array at this point in the fabrication process. The photograph is taken from the backside of the wafer, but the electrode pattern can still be clearly seen through the relatively transparent substrate. By limiting the kerfs to less than the full thickness of the wafer, the photolithographic electrode pattern on the opposite side remained undisturbed but the mechanical coupling between elements was decreased and the element directivity was increased. The kerfs were then filled with 301 epoxy (Epoxy Technology Inc., Billerica, Ma)

and after curing, the sample was lapped a few micrometers further to the final thickness of 47 μm. A final layer of aluminum was then sputtered onto the wafer to act as the ground electrode.

Small-diameter 50 μm wires were attached to each corner of the ground electrode using Epotek H20E conductive epoxy (Epoxy Technology Inc., Billerica, Ma) and the ground electrode was re-sputtered. This removed the reliance on conductive epoxy alone to form the ground connection and subsequently reduced the high-frequency (>50 MHz) impedance of individual elements by up to 20 Ω over previous versions of the array that relied solely on conductive epoxy to complete the ground connection. Although the conductive epoxy performs well for connections at lower frequencies, it was found to be inductive at higher frequencies and is therefore not ideal for use in high-frequency applications. A thick layer of EE129 conductive epoxy (Epoxy Technology Inc.) was then applied to serve as an acoustic backing layer for the array elements and as a redundant ground connection (section A of Figure 3-1.B). The embedded grounding wires were fed out the backside of the array stack (not shown in Figure 3-1.B). The conductive epoxy over the wire bonding pads was diced away using a micro-dicing saw to prevent this region from being piezoelectrically active. An insulating epoxy was then used to fill the space over the wire bonding pads (section B of Figure 3-1.B) and the heights of the backing epoxies were machined down to 3 mm. Each of the 12 array/backing layer stacks were then diced out and released from the glass carrier. A photograph of one of the array patterns with backing layers attached is shown in Figure 3-1.B.

To minimize the lateral dimensions of the packaged probe, we designed and had fabricated two custom polyimide flexible circuit board interposers (Microconnex, Snoqualmie, WA) such that they could be mounted along the sides of the array parallel to the forward-looking ultrasound beam and perpendicular to the array face. As we required a means of wire bonding from the array wire bonding pads on the front face of the transducer to the edge of the flex-circuit (in the thickness dimension), we designed 6-layer flex-circuit boards that allow connection to the elements on either side of the array. Each flex-circuit had 32 traces terminating at individual vias near the end of the board, as shown in Figure 3-2.A
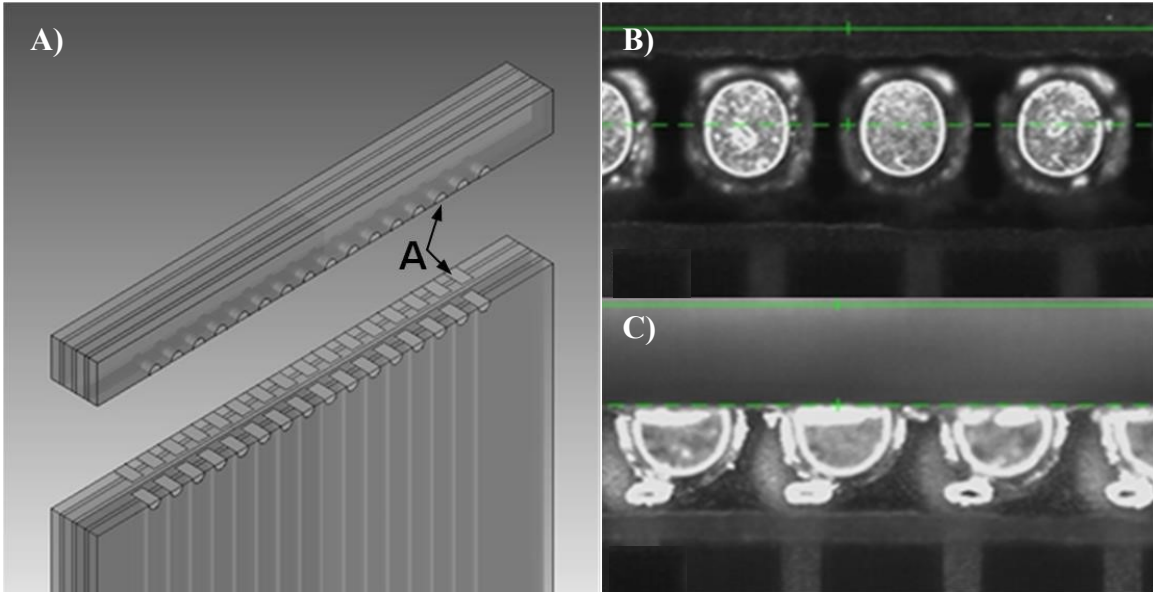
Figure 3-2: A) Exploded diagram of the custom flex-circuit design with solid filled vias that are bisected into wire bonding pads (A). B) (a) Solid filled vias before dicing and (b) solid filled vias after dicing through the central portion

The vias on the flex circuits were designed to be filled with solid copper. By cutting through the flex circuit board and bisecting the solid filled vias, we could create a series of flat exposed copper pads in the thickness dimension of the flex traces. a wire bond connection could then be made between the wire bonding pads on the array and the bisected vias, thereby connecting the array to the traces in the flex circuit. Figure 3-2.A shows the conceptual design of the sectioned flex circuit and vias. To fabricate this, the circuits were aligned on the dicing saw and cuts were made through the middle of the solid vias Figure 3-2.A. When viewing these flex-circuits in the thickness dimension, the vias that were diced in half created flat semi-circular wire bonding pads connected to individual traces on the circuit board (Bezanson, Adamson, and Brown 2015). To reduce crosstalk between elements, the array's fan-out pattern and the layering of the flex-circuits were designed so that neighboring elements would be on different circuit boards and next-to nearest neighbor elements (by example, element 1 and element 3) would be on opposite layers of the same flex with a ground plane in between.

After outsourcing the fabrication of the flex-circuits (Microconnex, Washington, United States) and dicing the solid vias in half, the next step was to align and epoxy the two flex-

circuit boards onto opposite sides of the transducer stack such that the diced vias were aligned with the wire-bonding pads fanning out from the array pattern. A jig was machined to hold the flex-circuits and transducer stack upright in front of the wire-bonding tool. 15 µm-diameter aluminum wire bonds were then used to connect the bonding pads on the array to the diced-via bonding pads on the flex-circuit. After wire bonding and removal from the jig, the grounding wires on the backside of the array were soldered to grounding pads on the surface of the flex-circuits and the sides of the assembly were encapsulated in insulating epoxy. Figure 3-3.A shows a photograph through a microscope of the endo-scopic array at this stage of fabrication.
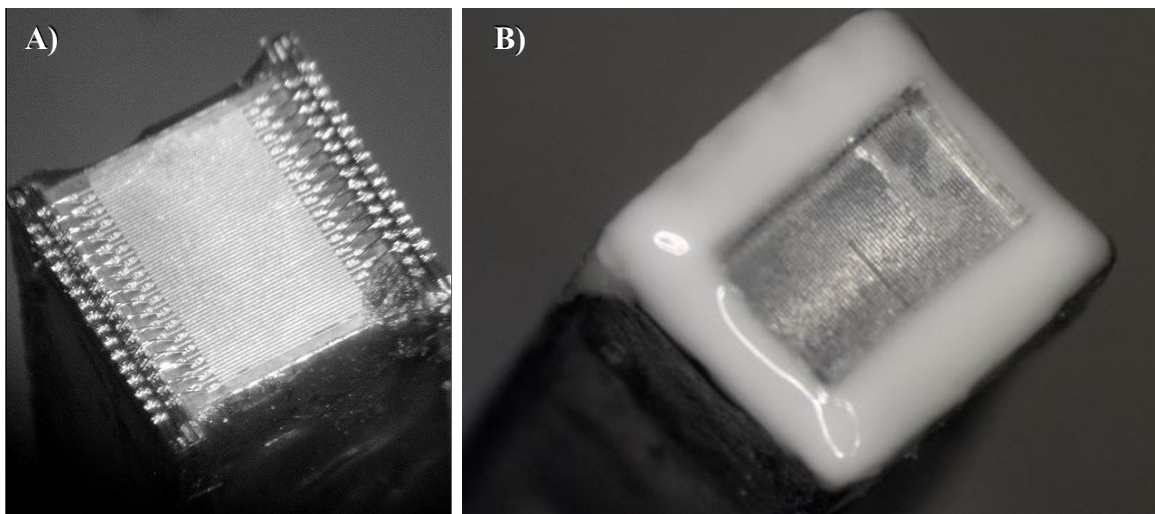
Figure 3-3: A) Photomicrograph of the front face of the endoscopic array transducer. The wirebonds are still exposed at this stage of fabrication and can be seen connecting the array elements to the solid vias on the flex circuit. B) Photograph of the front face of the endoscopic array transducer. The wire bonds have now been encapsulated with alumina-loaded 301 epoxy and the matching layer/lens combination has been aligned and epoxied to the front face of the transducer

The wire bonds were then encapsulated with a thick insulating epoxy consisting of a 30% by volume mixture of 3 µm alumina powder and Epotek 301 (Epoxy Technology Inc.) insulating epoxy. A matching layer/lens combination was then bonded onto the front face of the endoscope with a thin layer of unloaded Epotek 301. The matching layer was a 12 µm-thick layer of piezoelectric copolymer P(VdF-TrFE) film and the lens was a piece of polymethylpentene (TPX) that was machined with a cylindrically concave 2.2 mm radius of curvature, according to the methods described in section 2.2.8. This curvature creates a

passive elevation focus at a depth of approximately 7 mm according to theory (Maréchal et al. 2004; Cobbold 2006; H. Wang et al. 2001). A photograph of the front face of the packaged endoscope after the wire bond encapsulation and lens/matching layer application is shown in Figure 3-3.B and an illustrative example of the full array stack-up is shown in Figure 3-4.
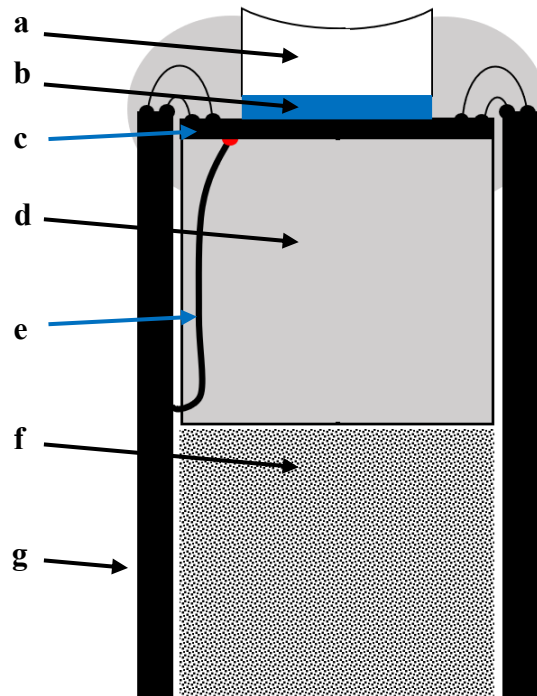
Figure 3-4: A depiction of the array stack-up used within the developed ultrasonic transducer. The acoustic lens (a) focuses the sound energy emitted by the piezoelectric wafer (c) and transmitted by the acoustic matching layer (b). The electrical interconnects (g) are bonded to the array elements through wirebonds and the acoustic backing layer (d) provides structural support and acoustic tuning for the array. The electrical return path is completed through a ground wire (e).

After encapsulation, 64 micro-coaxial cables with 50 Ω characteristic impedance were directly soldered to soldering pads on the proximal end of the flex cable. These coaxial cables had an outer diameter of only 400 μm and therefore did not add significantly to the size of the packaged endoscope. A photograph of the fully packaged endoscope is shown in Figure 3-5, where the 64 coax cables can be seen exiting the proximal end of the flex-circuit. The dual flex circuits were mounted into a small plastic housing that was fabricated using a

low-cost 3D printer (Jones et al. 2011). The function of this housing was to provide support for mounting the flex-circuits and an ergonomic handle to hold during imaging procedures.

Figure 3-5: Photograph of the fully packaged endoscope with the 64 micro-coaxial cables exiting the proximal end of the flex circuits and passed through the rapid-prototyped plastic housing

3.5 PERFORMANCE CHARACTERIZATION

The electrical impedance of individual array elements was measured using an RF impedance analyzer (4294A, Agilent Technologies Inc., Santa Clara, CA). The average and standard deviation of the impedance magnitude across the elements was 62 ± 13.5 Ω at the resonance frequency of 45 MHz. The average and standard deviation of the peak impedance phase across the elements was 1.5° ± 6.7°. Elements adjacent to the element under test were left unconnected. We were unable to find any clear correlation between impedance and the location of elements in the array, so it is likely that the element-to-element variation in impedance is associated with physical variations in components such as the cable assembly, or it may result from the random chipping of the array elements during the dicing process. It should be noted that multiple arrays were built over the course of this work and the arrays would typically have a few inactive elements. The inactive elements were typically open connections caused by either small cracks in the crystal substrate that

would form under the bonding pads during wire bonding, or through delamination of the bonding pad during wire bonding.

Figure 3-6 shows the impedance magnitude and phase of the individual array elements as collected by an Agilent 4294A impedance analyzer (Agilent, Santa Clara, USA).
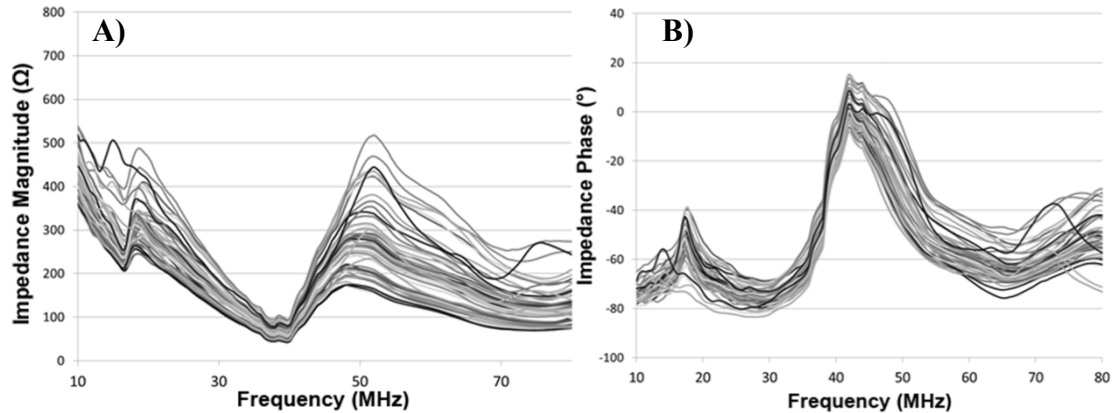
Figure 3-6: A) Impedance magnitude of individual array elements. B) Impedance phase of the individual array elements (61/64 active)

From the measured resonance and anti-resonance frequencies, the average thickness-mode electromechanical coupling coefficient (k_{eff}) was calculated to be 0.62 (Cobbold 2006; M. Kim, Kim, and Cao 2006). The impedance traces also reveal an additional resonance located near 20 MHz. This is our expected lateral mode, as discussed in Section 3.3 and falls well outside our operating band, as predicted from the low lateral frequency coefficient of PMN-32%PT. Although the variation of the on-resonance impedances is relatively small, there is a substantial increase in the variation of the anti-resonance impedances (or in general as the frequency is increased). This increased variation is potentially caused by the increasing effect of stray capacitances resulting from physical variability in the flexible circuit and cabling assembly. These electrical variations would have less of an effect at lower frequencies.

The pulse-echo response of the array was measured by recording the reflection from a quartz flat placed in a water bath, 7 mm in front of the array. Ten random elements across the array were measured individually. An average center frequency of 42 MHz was found with a 6 dB bandwidth of 55%. An oscilloscope screen capture of the pulse-echo response

and magnitude of the pulse spectrum for element 32 is shown in Figure 3-7. The pulse-echo response was also measured for an array without matching layer and lens. Although the signal amplitude was similar after the addition of a lens and matching layer, the bandwidth increased from 38% to 55% and the elevation focus narrowed to 152 µm. It is difficult to directly measure the insertion loss for a single element for this transducer without compensating for a relatively complex diffraction pattern. This occurs because the lens (with matching layer attached) has a focus at 7 mm, and at this depth, an individually pulsed element will have enormous diffraction losses.
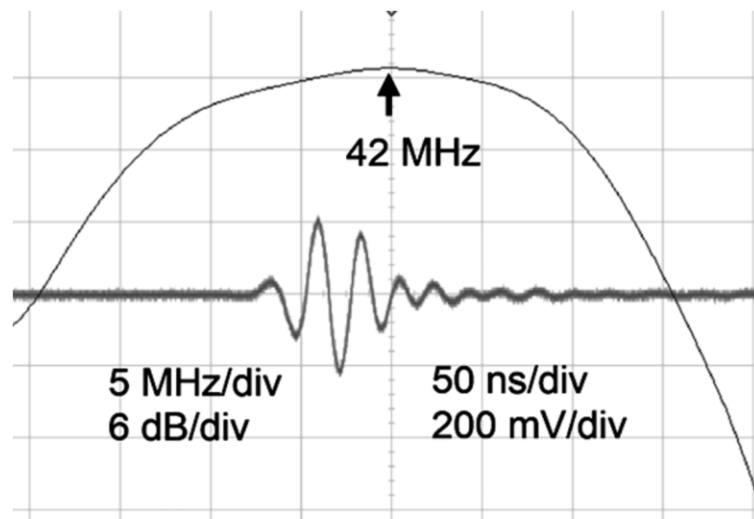
Figure 3-7: The pulse-echo response of a single element off a quartz flat located at a depth of 7 mm in a water bath. Both the time-domain pulse (center) and pulse spectrum (top arc) are shown

To obtain a quantitative assessment of sensitivity, we compared the one-way pressure measured with a needle hydrophone when a single element on our array was pulsed at a fixed voltage, to the pressure obtained when a single element on the VisualSonics MS700 was pulsed with the same voltage. Under these conditions, the average pressure received by the needle hydrophone was 24 kPa/V_{p-p} with the standard deviation between elements of 5.5 kPa/V_{p-p}, approximately twice the magnitude measured from a single element on the MS700. When compared with a previously developed 29-MHz PZT-5H array developed by Lukacs et al. (2006), we see that our array has 2.5 times higher average signal sensitivity

but with a much higher standard deviation of 23%. This is in comparison with the 4% standard deviation measured by Lukacs et al. (2006).

The increased sensitivity of the PMN-32%PT array is to be expected given the higher d_{33} coefficient of PMN-32%PT, in comparison to PZT-5H. The higher variability of the element signal sensitivity, in our array design, is believed to result from the finer features of our 45 MHz array, where imperfections during fabrication will have a larger effect. Additionally, the single-crystal structure of PMN-32%PT makes the piezoelectric wafer more prone to crack generation and propagation.

When considering the element to element variability it is important to note that the standard kerf width can vary between 10 μm to 14 μm depending on the conditioning of the dicing saw used for semi-kerfing, this factor alone could cause a 15% difference in the size of an element's active area. Additionally, friction between the blade and the piezoelectric wafer can cause local heating damage, micro-cracking or chipping of the wafer. In future work, quantification of the exact source of variability in element to element sensitivity is recommended, as well as the development methods to reduce the overall variation and damage. Though unexplored in this work, a quantification of factors producing mechanical damage within the crystal structure of PMN-32%PT wafers during fabrication may help to further explain this variability. It is also worth noting that in this work, semi-kerfed arrays were used to minimize the mechanical damage to the piezoelectric wafer and reduce sensitivity related variations between elements and that kerfless arrays may provide further improvements.

The peak electrical/mechanical crosstalk was measured by exciting a single element and recording the peak signal generated on neighboring elements. There was less than -28 dB of combined electrical and mechanical crosstalk to the nearest neighboring element, and less than -32 dB for the next-to-nearest neighboring element. All further elements beyond the first two neighbors possessed crosstalk levels below 40 dB. In this test only the excited element and the monitored element were connected, neighbouring elements were left unconnected.

Wide element directivity is desired in phased-array imaging to improve the image field of view. The element directivity was measured by scanning a hydrophone (Precision Acoustics Ltd., Dorset, UK) within the azimuth plane along an arc equidistant from a single element. To investigate the relation between directivity and kerf parameters, three identical arrays were constructed with varying kerf depths and compared with a VisualSonics MS700 40 to 50-MHz linear-array transducer. Specifically, the arrays were 1) a kerfless array with a monolithic substrate under the element electrodes, 2) an array with 10 μm wide by 10 μm deep semi-kerfs 3) an array with 10 μm wide by 20 μm deep semi-kerfs and 4) the fully kerfed VisualSonics MS700 40 to 50-MHz linear-array transducer, which has similar element pitch and center frequency. The directivity patterns of 8 elements were measured on each array; the patterns were averaged together and are summarized in Table 3-1 below. The one-way directivity patterns as a function of measurement angle are subsequently shown in Figure 3-8. To keep the plot in Figure 3-8 concise, the data from the array with the 10 μm kerf depth is omitted, but the curve falls between the kerfless and 20 μm-kerf directivity plots as expected.
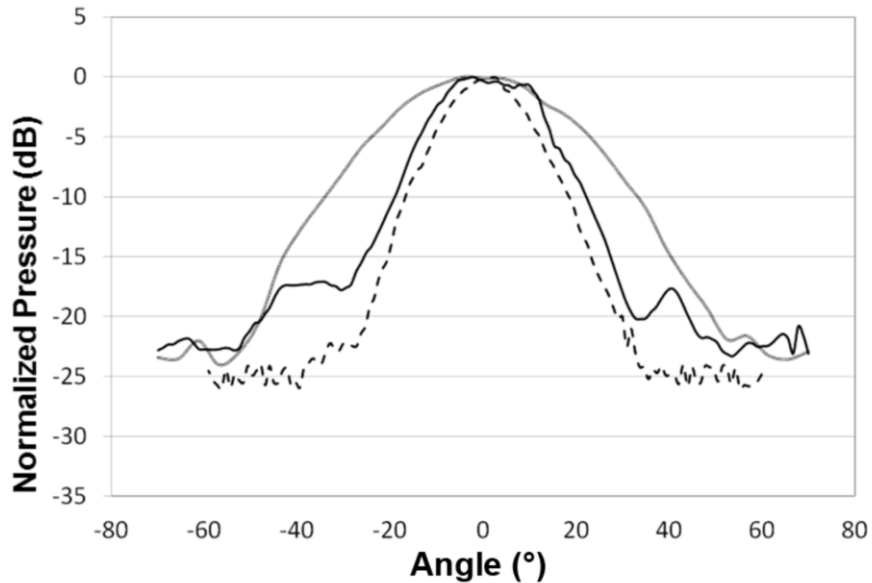
Figure 3-8: Measured one-way directivity patterns comparing the 20-µm deep semi-kerfed PMN-PT (solid gray) array with a kerfless PMN-PT array (solid black) and the commercially available VisualSonics MS700 array (dashed) with similar element pitch.

The fact that all our phased arrays have higher directivity than the MS700 is promising as we have previously demonstrated that the central 64 elements of the MS700 linear array can generate high-quality phased-array images between ±35° (Torbatian et al. 2010; Torbatian, Adamson, and Brown 2012; Torbatian et al. 2011). It should also be noted that the hydrophone is a 40 µm transducer which is wider than the array elements and is therefore expected to have poor directivity itself. This will cause the hydrophone to underestimate the one-way directivity pattern, possibly making the measurements closer to those of a two-way directivity pattern.

The geometric elevation focus was measured by scanning a needle hydrophone in a three-dimensional grid in front of the array and slicing the resulting data in the elevation plane. Figure 3-9 shows the resulting image generated by plotting the normalized peak demodulated signal at each point in space for a single element.

68
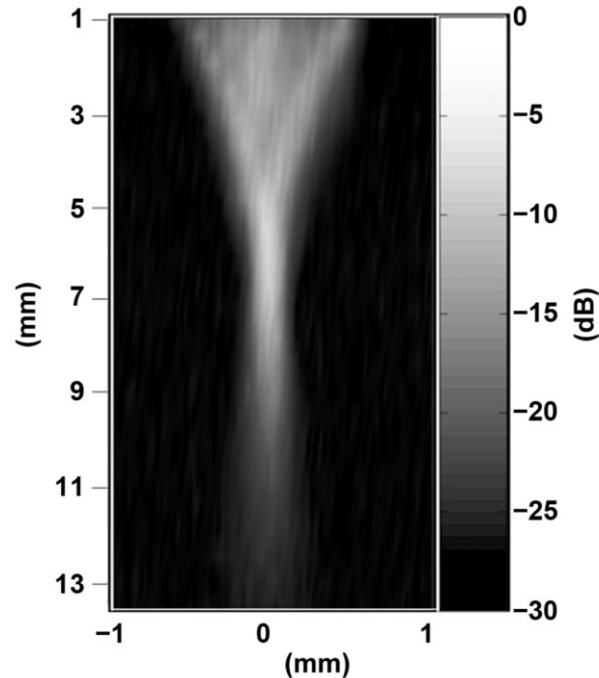
Figure 3-9: Experimental one-way elevation beam profile for a single element within the 40-MHz semi-kerfed PMN-32%PT array with 20 μm deep semi-kerfs. The beam was measured by scanning a needle hydrophone in a grid along the elevation plane. In this view, the array is located in the hydrophone tank at the 0 mm position and is pulsing downwards to the focus at ~7 mm

From the elevation beam profile, the geometric elevation focus was measured by determining the 3 dB one-way beamwidth at the elevation focus. The beamwidth was measured to be 152 μm at a depth of 7 mm. All 64 elements of the array were then connected to a VisualSonics Vevo 2100 imaging platform which had been reprogrammed to allow for phased-array transmit beamforming and single-channel receive data collection.

The focused beamwidth and 30 dB secondary lobes were then measured and the effects of steering angle on beamwidth are shown in Figure 3-10. Scripts were also written in MATLAB® (The MathWorks Inc., Natick, MA) that utilized the impulse response of the rectangular array elements to predict the focused radiation pattern of the array at various steering angles using methods similar to those described in (SanEmeterio and Ullate 1992) and (Lockwood et al. 1996). The simulation results are plotted along with the experimental data in Figure 3-10. The measurements were collected at a depth of 6 mm because this is a

transmit focal zone pre-set in the Vevo system and could not be moved precisely to the elevation focus at 7 mm.
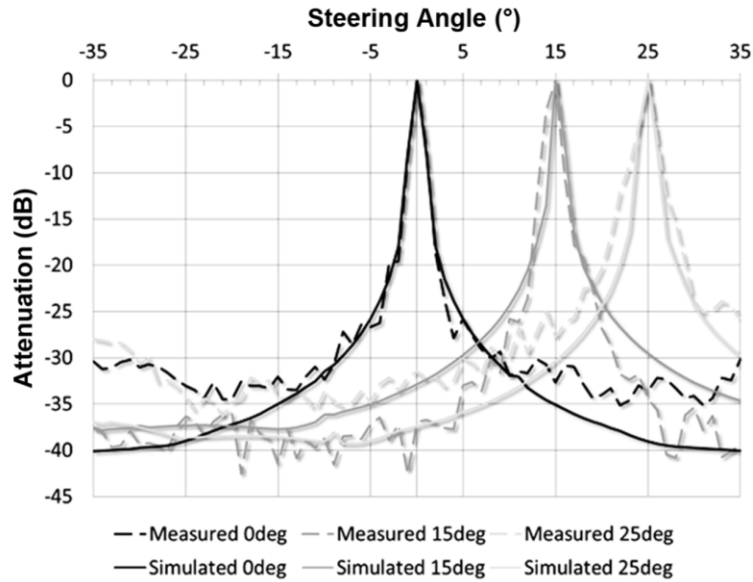
Figure 3-10: Experimental and simulated focused one-way lateral beam profiles for a 40 MHz 1λ pitch semi-kerfed array made from PMN-32%PT

At a steering angle of 0°, the 3 dB beamwidth (lateral resolution) was 80 μm and the 30 dB secondary lobes were located at ± 840 μm. With a steering angle of 15°, the lateral resolution was 134 μm and the 30 dB secondary lobes were at ± 690 μm. At a steering angle of 25°, the lateral resolution was measured to be 138 μm and the 30 dB secondary lobes grew to ± 1.74 mm, as shown in Table 3-1. These values agree well with the theoretical predictions of the impulse response simulations shown in Figure 3-10, with discrepancies in the prediction of -30 dB secondary lobes being attributed to measurement error resulting from positioning and alignment error in the test setup.

Table 3-1: Experimental and lateral beam profiles as a function of steering angle

Steering Angle	-3 dB beamwidth		-30 dB secondary lobes	
	Measured	Predicted	Measured	Predicted
0°	80 μm	92 μm	± 840 μm	± 1008 μm
15°	134 μm	136 μm	± 690 μm	± 1190 μm
25°	138 μm	140 μm	± 1740 μm	± 1466 μm

3.6 IMAGING RESULTS

After characterization of the pulse-echo responses, directivities, and focused beam profiles, the final step in proving the phased array technology is to generate images of phantoms and ex vivo tissue. This is an important step in the characterization because transducers often have very good water tank performance but have insufficient signal-to-noise performance when imaging highly attenuating tissues. To our knowledge, these are the first images generated by a forward-looking fully sampled high-frequency (40 MHz) phased-array endoscope.

Through a collaboration with VisualSonics Inc., we were able to reprogram the VisualSonics Vevo 2100 imaging system such that it could transmit beamforms off to various steering angles and collect the data one channel at a time. The individual channel data was then transferred to a desktop computer and receive beamforming was performed offline using a MATLAB® script. This procedure was identical to that previously described, when generating phased-array images with the central 64 elements of the MS700 linear-array transducer (Torbatian et al. 2010; Torbatian, Adamson, and Brown 2012).

The first images tested were of 25 μm wire targets situated in a deionized water bath. Multiple wires are mounted in stepped increments of 1 mm (Figure 3-11). Next, images were generated of a 6% gelatin (G2500-1KG, Sigma, St. Louis, MO)/4% silicon dioxide (s5631-500G, Sigma) tissue-equivalent phantom. This phantom was constructed according to the process outlined in (Ryan and Foster 1997) and the properties were verified to be a close match to tissue following the techniques described in (Cook, Bouchard, and Emelianov

2011). The wire phantom in tissue-equivalent phantom is shown in Figure 3-11.B. Note that the axial resolution is degraded when imaging wire phantoms due to wave mode conversion of the ultrasonic pulse into shear waves propagating along the length of the wire phantoms, causing an elongation of the pulse reflection and a subsequent reduction in axial resolution. Therefore, even though the array has finer axial resolution than lateral resolution, this artifact degrades the axial resolution to the level of the lateral resolution.
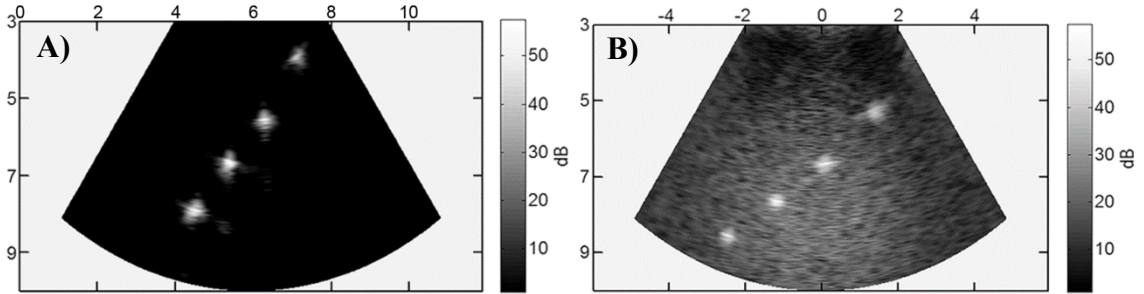
Figure 3-11: 25-µm wire phantom imaging results, A) phantom mounted in a deionized water bath, plotted with 60 dB dynamic range, and B) phantom mounted in tissue-equivalent medium plotted with a 60 dB dynamic range

Finally, to investigate the soft-tissue imaging abilities of the probe, cadaveric porcine brain tissue was imaged. A potential application of this endoscope is imaging the sulci during tumor resection surgery. If the lateral cross-section of the endoscope is small enough, then the probe can be inserted into the sulci of the brain through a small hole in the skull and the amount of remaining tumor can be imaged in a minimally invasive manner. Figure 3-12.A shows the experimental imaging setup of our endoscope *'A'* and sulcus *'B'* of the porcine brain. The endoscopic form-factor of the probe allows it to be partially inserted into the sulci of the brain without the need for removal of healthy brain tissue.
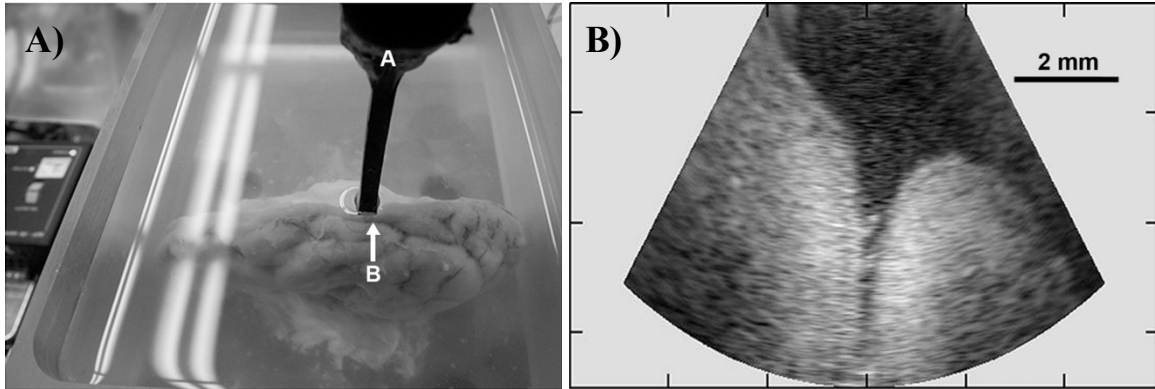
Figure 3-12: Porcine brain tissue imaging setup and resulting image. (A) Shows a photograph of the setup of the probe (feature 'a') as it is positioned over the central sulcus (feature 'b') of the porcine brain. B) A typical image showing the view of the central sulcus as seen by the probe, plotted with 55 dB dynamic range

3.7 DISCUSSION AND CONCLUSIONS

A phased array intended for high-frequency medical ultrasound imaging was successfully developed and packaged into an endoscopic form-factor. The array has 64 elements with a 38 μm element-to-element pitch and operates at a center frequency of 42 MHz. The array was a photolithographic semi-kerfless design and was fabricated on a PMN-32%PT substrate. A novel method of dicing solid vias within a multilayer flexible circuit was used to create wire-bonding pads that minimized the packaging size of the endoscope. A single matching layer and TPX lens were adhered to the front face of the transducer, providing increased bandwidth and elevation focus. Because the TPX lens is thicker than the wire bonds, the face of the array can come into direct physical contact with the test object. However, the use of an acoustic coupling medium such as water immersion or gel is still required.

One of the most important features in the fabrication of this phased array endoscope is the small packaged size of 2.5 x 3.1 mm. For high bond reliability, the minimum elevation footprint for the wire-bonding pad pattern is 350 μm per side, with individual bonding pads measuring 140 x 70 μm. It would be challenging to reduce this any further, as can be seen in Figure 3-3. The thickness of the flex-circuit boards (400 μm) is more than we originally estimated, but this is limited by what could be manufactured. The number of layers in our flex-circuit could be decreased from six to four, but this may result in increased electrical

73

crosstalk. The last option for decreasing the elevation dimension is to reduce the elevation aperture. For any possible reduction in the azimuth dimension to be made, there would need to be a reduction in the number of elements because of the constraints of the wire bonding fanout, and hence the resolution would be lowered, and secondary lobe levels increased. This is apparent from Figure 3-3, which shows the array elements coming to within about 100 μm of the edge of the endoscope. The option of simply reducing the size of the elements instead of the number of elements could result in a lower azimuthal dimension; however, it would increase the elevation or interconnect dimension because more bonding pad rows would be required in the fan out to compensate for the decreased element pitch. In general, it would be very difficult to decrease the size of this phased-array endoscope without some sacrifice in image quality.

The performance of the phased array was excellent and agreed very closely with the theoretical predictions. The electrical impedance magnitude showed a nearly pure real impedance on resonance with an average impedance magnitude of 65 Ω, which makes it a good match to 50 Ω coaxial cables. The lateral modes fell well below the operating bandwidth of the transducer, as we predicted based on the frequency coefficients of PMN-32%PT. The transducers individual elements produced pulses with a two-way bandwidth of 55%, a directivity of ± 20°, and an elevation beamwidth of 152 μm. This is very close to the theoretically predicted beamwidth of 157 μm based on the diffraction limit. A possible explanation for the elevation resolution exceeding theory is that the radius of curvature of the lens may be slightly less than the 2.2 mm design radius. Another possible explanation is that the speed of sound for TPX may be slightly different from the literature value of 2200 m/s (H. Wang et al. 2001), or it could be due to the small amount of play in our motorized measurement system.

The transducer array was connected to a reprogrammed VisualSonics Vevo 2100 imaging platform to allow for phased array transmit beamforming and individual channel receive data collection. One-way focused radiation patterns were collected at angles of 0°, 15°, and 25° using a needle hydrophone. These radiation patterns were plotted over the top of the theoretical impulse response radiation patterns and were in very close agreement. The measured lateral resolution at 0° was 81 μm, which agrees very well with the theoretical

diffraction limit of 87 μm. Again, we measured a resolution slightly better than the diffraction limit, but this slight discrepancy can be attributed to a small amount of play inherent to the motorized measurement system. Using a reprogrammed VisualSonics system as a phased array beamformer is not practical for in vivo imaging because scans take between 20 min and 6 hours depending on which beamforming strategy is used. Therefore, another major challenge in the development of a high-frequency phased array imaging system is the development of a suitable electronic beamformer.

As a final characterization of the transducer array, images were generated of wire phantoms and ex vivo tissues. Images of 15 μm wire phantoms staggered by 1 mm intervals in a water bath demonstrated that the array was beamforming correctly within the ± 35° beam-steering window with the expected depth of field. Images of 15 μm wire targets separated by 1 mm in a tissue-mimicking material demonstrated that the transducer array was sensitive enough and possessed adequate signal-to-noise ratio to generate high-quality images in an attenuating, scattering medium. The endoscope was also used to generate ex vivo images of a porcine brain. Specifically, it was used to generate images of the brain from within the sulcus, demonstrating that this type of phased array endoscope has great potential in real-world endoscopic applications.

Although the image quality was relatively good, grating lobe image artifacts can be seen in Figure 3-12.B at wide angles, where features at the edges of the image are blurred. These grating lobe artifacts arise from the use of a larger than conventional element pitch (1λ) for a phased array transducer, where a pitch of 0.5λ to 0.75λ would be more conventional. Some adaptive beamforming techniques have previously been developed to address this issue (Torbatian 2012), however these require substantial processing power to achieve real-time frame rates. An alternative passive approach to grating lobes suppression is investigated in chapter 4.

CHAPTER 4:

HIGH-FREQUENCY PHASED ARRAY WITH VERNIER ELEMENT SPACING FOR GRATING LOBE SUPPRESSION, FABRICATION AND PERFORMANCE

This chapter presents the design, fabrication, and characterization of a 50 MHz phased array with a Vernier element geometry for grating lobe suppression. The Vernier array was based on a 128-element transducer with half-wavelength pitch, where every third element was used for transmitting, every fourth element was used for receiving, and unused elements were left inactive. The Vernier array design utilizes a different pitch for the transducer elements within the transmit and receive apertures. In theory, this causes the grating lobe artifacts from transmit and receive events to fall at different locations, preventing the constructive interference of the transmit and receive grating lobes.

The array design is a forward-looking kerfless design based on a PZT-5H substrate with an element-to-element pitch of 19 μm. The probe was packaged in a 2.5 mm by 3.1 mm endoscopic form-factor. The array was fabricated with a single P(VDF-TrFE)-copolymer matching layer and a polymethyl-pentene (TPX) lens for passive elevation focusing to a depth of 6 mm. To generate beam profiles, images, and videos, the transducer was connected to an in-house developed 64-channel, high-frequency phased array beamformer. Near real-time radiation patterns and images were collected at a frame rate of 10 Hz. The performance of the Vernier array was directly compared to that of the previously developed phased array transducer with approximately one wavelength pitch. Both transducers possessed similar two-way beamformed pulse bandwidths of 60%. At large steering angles, the Vernier array suppressed the grating lobe levels 15 dB over the previously developed phased array, in relation to the beamformed signal intensity. However, as a result of the

sparseness of the Vernier array, the measured two-way sensitivity was 18.2 dB lower than the phased array with the fully active aperture. Experimental measurements were in good agreement with the theoretical predictions of 20 dB grating lobe suppression and 22 dB lower sensitivity than the phased array. Comparison images were generated of wire phantoms in a water bath as well as wire phantoms situated in a tissue phantom in order to assess the trade-off between lower grating lobe levels at the expense of lower sensitivity.

4.1 PREAMBLE

This chapter is based on my first author publication (Bezanson, Leadbetter, and Brown 2014). The contents of this chapter remain mostly unaltered. However, some additional figures and discussions related to simulations and their results have been added. Additionally, some details on the methods of array fabrication have been omitted for conciseness, as they have been covered in previous chapters.

4.2 ARRAY DESIGN

In the previous chapter, the successful development and characterization of a 64 element, one-wavelength pitch, high-frequency (45 MHz) forward-looking phased array transducer packaged into a miniaturized form-factor (3.1 x 2.5 mm) was discussed. A novel solution to the array interconnect was introduced, whereby we were able to wire-bond to the thickness dimension of a flexible circuit board situated in-line with the forward-looking ultrasound beam. This allowed us to avoid any additional space requirements for a flex circuit bend radius in the endoscope packaging (as discussed in Chapter 3), and the technique and flex circuits were implemented for the Vernier array.

The previously developed array, described in Chapter 3, consisted of 64 elements with one-wavelength pitch, which is considered unconventionally large for a phased array with relatively wide steering angles. As a result, the images suffer from relatively large grating lobe artifacts. The most straightforward method of suppressing these grating lobe artifacts (without sacrificing aperture/resolution) would be to simply decrease the element pitch to approximately half-wavelength by doubling the number of elements in the array to 128. Unfortunately, doing this would at least double the amount of space required for the

interconnect, making the endoscope too large for many applications requiring such a miniaturized device. Even with our novel interconnect technique designed to minimize packaging, nearly 50% of the cross-section is dedicated to the 64-channel interconnect. Other approaches to suppressing grating lobes in a large pitch phased array involve signal processing techniques similar to ones we have implemented previously (Torbatian, Adamson, and Brown 2013). However, grating lobe suppression algorithms are computationally intensive and lead to decreased frame rates. In this study, a Vernier array design has been investigated as a technique to help suppress grating lobes. The technique allows for grating lobe suppression without sacrificing resolution, the number of interconnected elements, or the frame rate (Von Ramm, Smith, and Thurstone 1976; Brunke and Lockwood 1997). The Vernier array design has never been fabricated or suggested before for a high-frequency array. However, this work proposes that it could be a solution that minimizes the number of elements in the interconnect, while at the same time suppressing grating lobe artifacts.

In the past, there has been considerable research on developing two dimensional (2D) arrays. In 2D arrays, moving to a sparse design dramatically reduces the total number of interconnects required. From this research, several techniques have been developed that optimize the radiation patterns resulting from sparse arrays (Von Ramm, Smith, and Thurstone 1976; Brunke and Lockwood 1997) while maintaining as few electrical interconnects as possible. One of the most effective of these is the Vernier array, where transmit and receive elements are spaced with different element pitches (Brunke and Lockwood 1997). The transmit and receive aperture both generate grating lobes (regions of constructive interference), but in such a manner that they are out of phase and so cancel out the two-way radiation pattern. In our Vernier design, we have spaced 128 elements at ½λ pitch. There are transmit elements on every 3rd element and receive elements on every 4th element. Resulting in 43 transmit elements and 32 receive elements, since many elements are shared this results in an array with 64 active elements. This configuration is depicted in Figure 4-1, where the red elements are used for transmitting, the green elements are used for both transmit and receive, and the blue elements are used for receiving only. Our Vernier array pattern was designed to fan out to a 64-element interconnect, identical to our previously

developed 64 element phased array (Bezanson, Adamson, and Brown 2014) and requires no extra packaging when compared to the array described in Chapter 3.
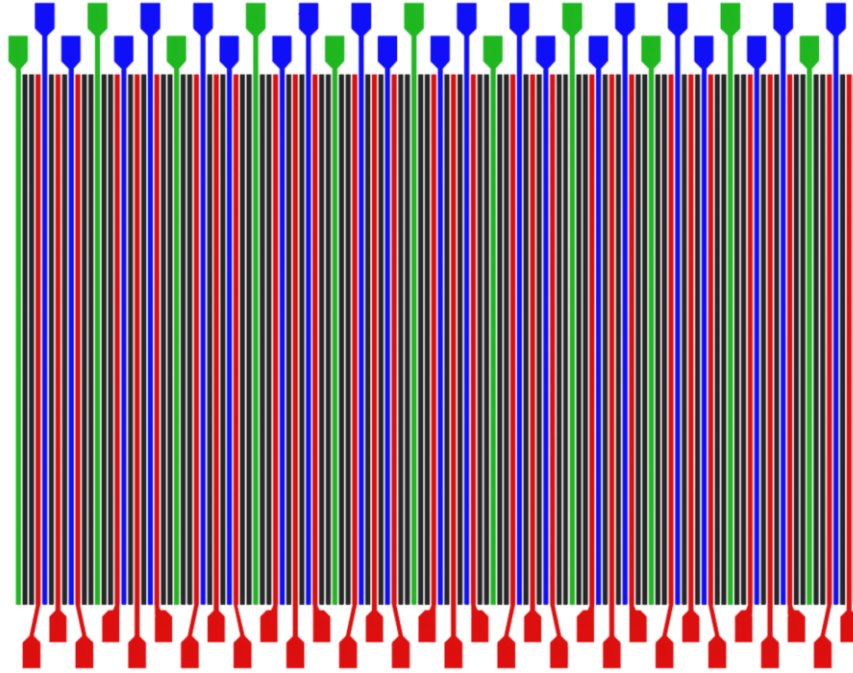
Figure 4-1: 128 element Vernier Array Pattern, red elements are used for transmit events, blue for receive, and green elements are common to both. Grey elements are unused; there are 64 total electrical connections

When considering the design of a Vernier array for the reduction of grating lobes, it is important to note that grating lobes occur at the angles described by Equation (4-1):

$$\emptyset_i = sin^{-1}(\pm \lambda / d) \tag{4-1}$$

where d is the pitch of the elements, λ is the wavelength and ϕ_i is the angle from the central axis where the grating lobe will appear (Cobbold 2006).

From Equation (4-1) it can be seen that it is possible to have the grating lobes generated during the beamformed transmit event, fall in the regions of destructive interference that occur during the receive events by changing the relative pitch of the two groups of elements. Though non-periodic array patterns have been investigated, they have been shown to be less effective than the Vernier array patterns in the reduction of grating lobes (Brunke and Lockwood 1997).

4.2.1 SIMULATIONS

Impulse response simulations were run, according to the methods laid out in section 2.3, on several methods of reducing grating lobes and the results are summarized in Figure 4-2. The ideal case is captured in Figure 4-2.A where the radiation pattern of a 128-element array with ½λ pitch element spacing is shown. The array has a sharp intensity fall-off around the pulse focus at 30° with the grating lobe remaining below -60 dB relative to the pulse intensity at the focus. Though the performance of this array is significantly better than all other configurations, it requires 128 active elements and, therefore, 128 electrical interconnections. Due to the packaging constraints of the array, we are only able to achieve 64 active elements in the required cross-section. The performance of an array with 64 active elements is shown in Figure 4-2.B, and the grating lobe signal intensity of approximately -30 dB at -30° can be seen.

To optimize the performance of the array while constraining the design to 64 active elements, both pseudo-random (Figure 4-2.C), and Vernier array configurations (Figure 4-2.D) were simulated using the impulse response method. For the simulation, the pseudo-random array model was based on a 128-element array, with half of its elements removed. The remaining elements were then shifted by a random amount between -0.5 and +0.5 of an element's pitch. The random nature of the simulation meant that each simulation was slightly different. However, the averaging effect across the array stack meant that most runs followed the trend shown in Figure 4-2.C.

The 128 element design used elements at a ½λ spacing of 19 μm with an electrode width of 10 μm. All simulations were completed for PZT-5H substrates at 49 μm thick and with an electrode height of 1.52 mm. The 64 element array design used 1λ spacing of 38 μm with an electrode width of 28 μm. The elements simulated in both the pseudo-random and Vernier array designs were 10 μm wide, but with custom spacings as described previously.

80
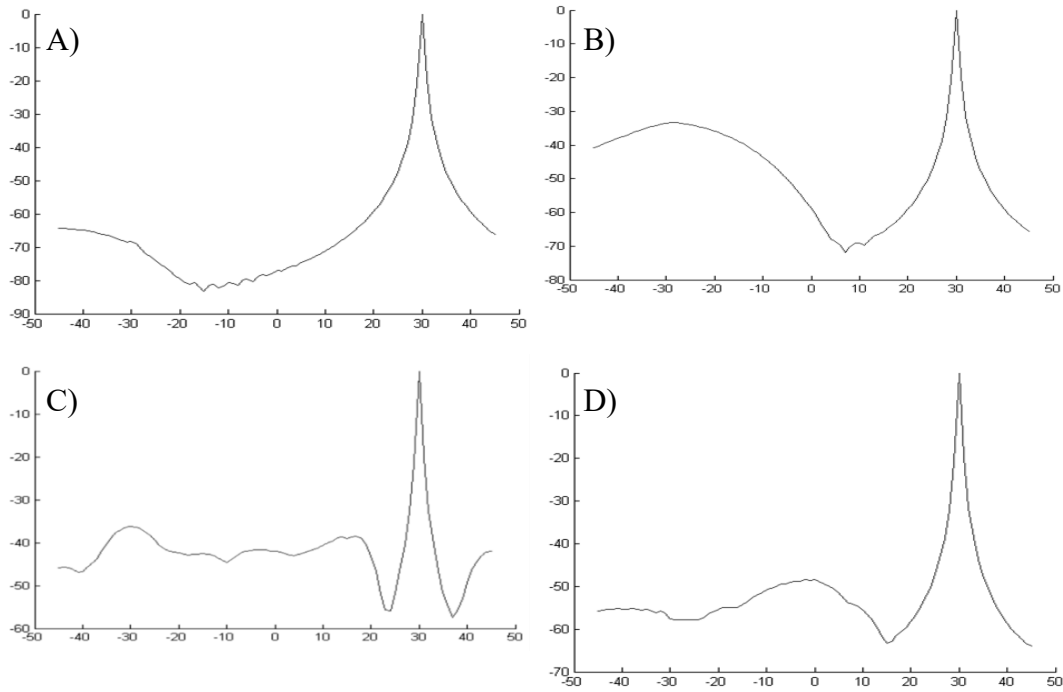
**Figure 4-2: Impulse response simulations of various array configurations focused on + 30°
showing grating lobe effects and predicted noise floor levels. A) 128-element array with
½λ pitch, B) 64-element array with 1λ pitch, C) 64-element array with randomized el-
ement pitch, and D) Vernier array with ½λ pitch and 64 active elements, every 4th ele-
ment of the 128 element pattern used on transmit and every 3rd element used on receive.
X-axis scales are in degrees, and Y-axis scales are in dB**

The pseudo-random arrays showed a broadening of the grating lobe image artifact, while
the Vernier array showed a significant level of grating lobe attenuation. Accordingly, the
Vernier array design was chosen for further investigation.

4.2.2 BEAMFORMER SETUP

To drive the Vernier array, an in-house developed 64 channel phased array beamformer
was use with transmit and acquisition timings that were tailored for the Vernier array ge-
ometry. A Virtex-5 FPGA was used for the generation of pulse triggers, and the return
signals were digitized by multiplexing the echo signals into a two-channel 500 MHz PCIe
digitizer card (AlazarTech, Canada). Because only 2 receive channels could be digitized at
once, the transmit events would be repeated 16 times for each focal zone allowing for data
to be digitized on all 32 receive channels of the Vernier array. Though this technique was
16 times slower than if all channels were digitized simultaneously, it allows for

dramatically reduced hardware complexity while still allowing frame rates up to 10 Hz. Transducers were driven by up to ± 50 V and the pulse frequency was set to 45 MHz with a fractional bandwidth of 80%.

4.3 METHODS

To complete the evaluation of the Vernier array, and to have a traditionally constructed array to contrast its performance against, the respective transducer designs were fabricated and then characterized. The methods of fabrication are presented and discussed in the following sub-sections.

4.3.1 FABRICATION

To minimize the lateral dimensions of the packaged probe, we used a similar design to that described in Chapter 3 with two custom polyimide flexible circuit board interposers (Microconnex, Snoqualmie, United States) mounted along the sides of the array, parallel to the forward-looking ultrasound beam and perpendicular to the array face. The 4-layer flexible circuit boards were designed such that each had 32 traces terminating at solid filled vias near the proximal end of the boards. To create a surface for wire-bonding, the 32 terminating vias were diced in half, creating bonding pads on the thickness dimension of the flex-circuits, as shown in Figure 3-3.

The individual array patterns were 2.4 mm x 2.1 mm and were spaced with 500 μm gaps between patterns along the piezoelectric substrate. Both the Vernier array and the reference 64 element array were constructed using an identical process, but with different masks being used during photolithography to differentiate the array element electrodes, and the reference array being patterned with 10 μm wide by 20 μm deep semi-kerfs between elements following photolithography.

The fabrication process used high-resolution positive photolithography and wet etching on a 15 mm^2 PZT-5H substrate (3203HD, CTS Corp, USA) with 1.5 μm copper electrodes. Once the array electrodes were defined, the substrate was flipped over and lapped to the final thickness of 44 μm. Additionally, 50 μm diameter grounding wires were attached to each corner of the arrays back face using EE129 (Epoxy Technology, United States)

conductive epoxy. A 0.5 µm ground electrode was applied over the back face using an electron beam evaporator (Mantis Deposition, United Kingdom), and a mask was used to prevent the ground electrode from coating inactive areas of the array such as behind the bonding pads.

The backing layer was made from 301 Epotek Epoxy (Epoxy Technology, USA) which had been mixed with 3 µm aluminum oxide powder (Logitech, Scotland) to bring the acoustic impedance to 6 MRayls (H. Wang et al. 2001). The array was then aligned with the interconnect flex-circuit, and array elements were then wire-bonded to the electrical interconnect using 17 µm aluminum wire. The grounding wires were soldered to the flex circuits, and as a final stage, a 12 µm P(VDF-TrFE) matching layer was bonded to the front face along with a TPX lens to achieve the elevation focus. The TPX lens was cast with a 1.9 mm radius of curvature to obtain the desired 6 mm focus.

4.3.2 CHARACTERIZATION

To characterize the kerfless Vernier array endoscope, electrical tests were conducted to determine the element impedances, radiation patterns were collected, and phantom targets were imaged using an in-house developed high-frequency phased-array beamformer. All characterizations of the Vernier array's performance were done in direct comparison to the previously developed phased array transducer described in Chapter 3.

4.4 RESULTS AND DISCUSSION

To validate the Vernier array, a characterization of the array's performance was completed and compared with identical tests done using a previously developed and similarly constructed phased array transducer.

4.4.1 ELECTRICAL IMPEDANCES

The electrical impedances were measured using an Agilent 4294A impedance analyzer (Agilent, Santa Clara, USA) as shown in Figure 4-3. An on-resonance impedance of 135 Ω was measured with a standard deviation of 5.8 Ω for the 64-element Vernier array.
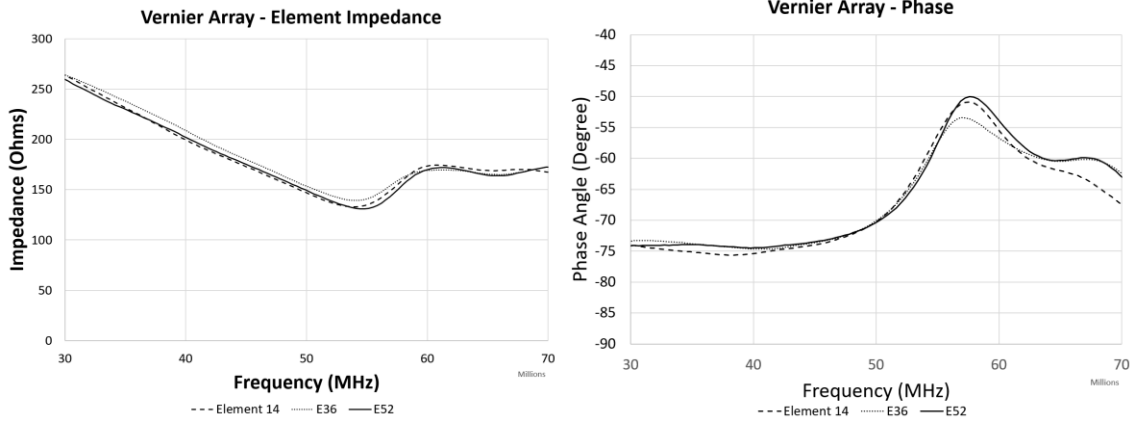
Figure 4-3: Vernier array element impedances (left) and element phase data (right) from three characteristic elements spanning the array. Impedances were collected using an impedance analyzer and the array tips were submerged in water to emulate the loading effect of tissue during imaging

An impedance of 62 Ω with a standard deviation of 13.5 Ω was subsequently measured for the 64-element 1λ pitch phased array. The Vernier array elements are half of the width of the phased array elements, and so a higher impedance is expected.

4.4.2 PULSE-ECHO BANDWIDTH AND SENSITIVITY

For the remainder of the transducer characterization, the in-house developed phased array beamformer and custom real-time software were used for characterization and array performance measurements. The first measurement characterized the two-way beamformed pulse bandwidth and sensitivity. The Vernier array was transmit-beamformed to a focal depth of 6 mm at a 0° steering angle, and then dynamically receive beamformed along the 0° angle. Unfortunately, an absolute insertion loss measurement could not be made as the minimum pulse-echo reflecting off a quartz flat was large enough to saturate the pre-amplifiers in the beamformer. In place of an absolute sensitivity measurement, the beamformed pulse was instead reflected off a 15 μm aluminum wire phantom situated in a water bath, and this was directly compared to the receive beamformed pulse from the one-wavelength pitch phased array, as shown in Figure 4-4.

84
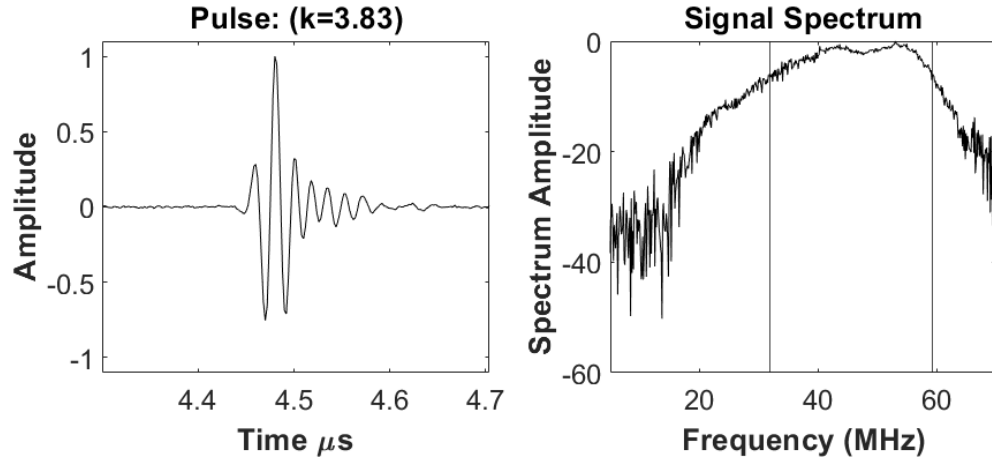
Figure 4-4: Pulse-echo of the beamformed signal from the Vernier array and signal spectrum. The -6 dB bandwidth is 68%, and the peak-peak amplitude is 1500mV$_{p-p}$ and has been normalized in the above plot

Theoretically, since the Vernier array is only using 43/128 elements on transmit and 32/128 elements on receive, it should lose approximately 9.5 dB of sensitivity on transmit and 12 dB of sensitivity on receive totaling -21.5 dB relative to a fully sampled phased array. By directly comparing the amplitudes of the two-way beamformed pulses, the Vernier array was found to be -18.2 dB less sensitive than the phased array, which is in good agreement with the theoretical prediction.

A possible reason for the Vernier array being slightly more sensitive than predicted is that since the elements are narrower than the elements in a stock array, they have a higher ratio of their perimeter to their cross-sectional area. Electrical edge effects around the edge of the elements may effectively broaden the active area of the element due to the use of the kerfless piezoelectric wafer in these arrays, as shown in Figure 4-5. Since the electrodes within the reference 64 element arrays are wider than the Vernier array electrodes, the Vernier array elements may experience a greater. Thereby causing a proportionally higher level of recruitment of the piezoelectric wafer in the Vernier array and moderately increasing the array's sensitivity relative to the reference array.
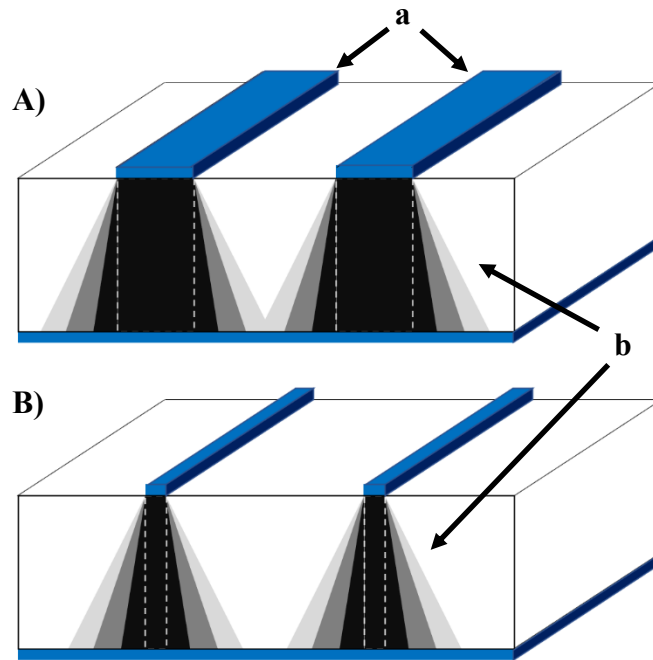
Figure 4-5: An illustrative example demonstrating the electrical field edge effects around array elements in a kerfless piezoelectric wafer. It is conjectured that the amount of material recruited by the electrical field edge effects would be proportionally greater around narrow elements (B) than around wider elements (A). In this illustration the array electrodes are shown by feature (a) and the recruited portion of the piezoelectric wafer is shown by feature (b)

4.4.3 TWO-WAY BEAM PROFILES

Qualitatively, it is apparent that the Vernier array has significantly lower grating lobe levels with respect to the main lobe than the one-wavelength pitch phased array. Figure 4-6 (a) and (b) show comparison images of a 15 μm aluminum wire phantom situated in a water bath collected at a 10 Hz frame rate and displayed with a 45 dB dynamic range. The wire phantom is situated at a 30° steering angle. There is a large grating lobe artifact for the phased array with one-wavelength pitch, which is not present for the Vernier array.
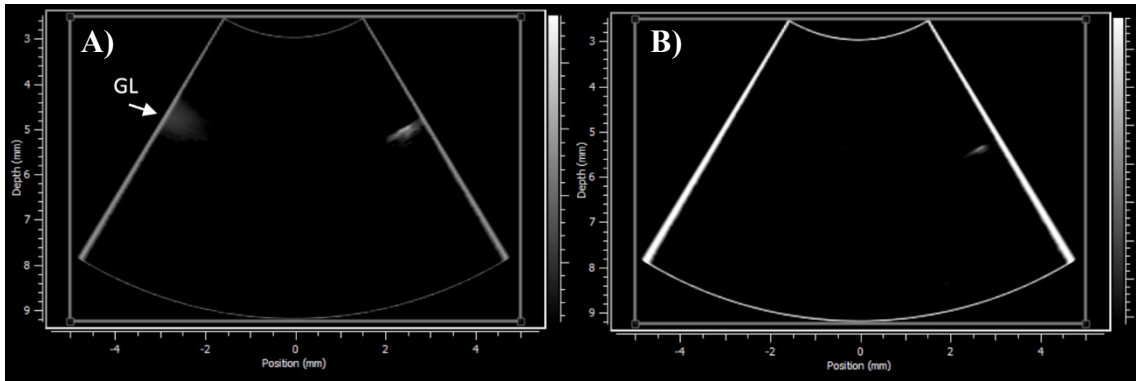
Figure 4-6: Real-time images of a wire phantom in a water bath for one-wavelength pitch semi-kerfed phased array (A) and kerfless Vernier array (B). In this test the Vernier array design demonstrates significantly reduced grating lobe image artifacts (feature 'GL')

More quantitatively, we can plot the maximum of the demodulated RF lines for the two images producing the two-way radiation pattern, as shown in Figure 4-7 (a) and (b). This allows us to directly compare the measured radiation patterns to the theoretical impulse response simulations for both the phased array and the Vernier arrays (SanEmeterio and Ullate 1992).
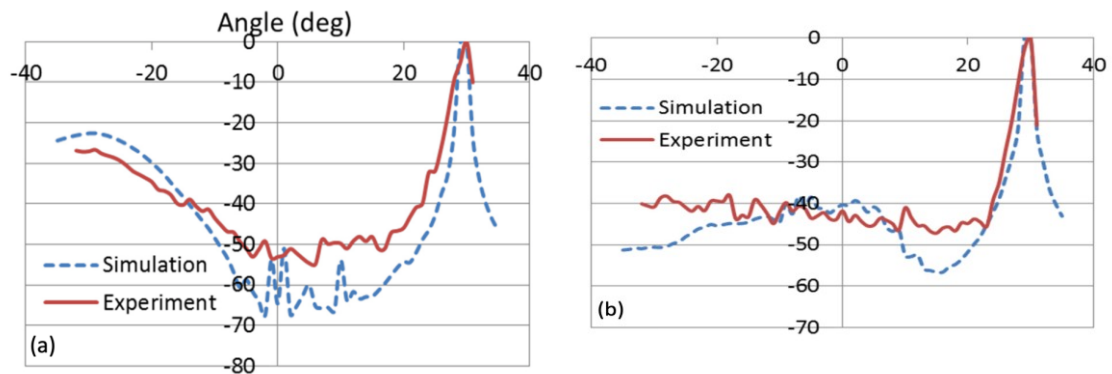
Figure 4-7: Two-way radiation pattern off a wire phantom in a water bath for (a) one-wavelength pitch phased array and (b) Vernier array at a steering angle of 30 degrees

The measured radiation patterns for both the one-wavelength pitch phased array, and the Vernier array are in good agreement with the theoretical impulse response simulations. The impulse response simulation predicts that the amount of grating lobe suppression for the Vernier array should be approximately 20 dB. However, we measured a maximum of 15 dB grating lobe suppression. The slight discrepancies between the measurements and the

87

theoretical predictions are expected since we are simulating an infinitely small point re-flector but are experimentally measuring with a wire phantom. Another possible reason for the discrepancies is the fact that these are kerfless arrays, which typically have slightly elevated secondary lobes and slightly broader main lobes (Morton and Lockwood 2002).

In order to assess the effect of the reduced sensitivity with the Vernier array, a tissue-mim-icking phantom was imaged. The tissue phantom contained several 50 μm diameter nylon wires, and an example of the resulting images is shown in Figure 4-8 (a) and (b). Figure 4-8 (a) shows an image of the tissue phantom generated with the one-wavelength pitch phased array, and Figure 4-8 (b) shows a tissue phantom image generated with the Vernier array. Both images were displayed with a 50 dB dynamic range. It is clear when these images are compared, that the low sensitivity of the Vernier array dramatically reduces the penetration depth into a tissue-mimicking phantom. The nylon wires at 8 mm are barely detectable with the Vernier array although good SNR is seen with the phased array.
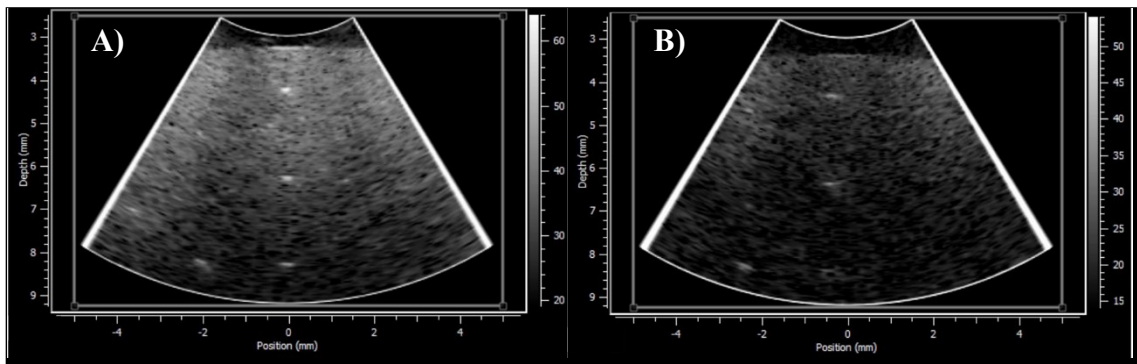
Figure 4-8: Nylon wires embedded in a tissue-mimicking phantom for (A) the one-wavelength pitch phased array and (B) the sparse Vernier array. In highly attenuating mediums such as tissue, the reduced sensitivity of the Vernier array design degrades imaging preformance

It is worth noting that the dark bands and strong signal at angles between 20° to 30° in Figure 4-8 were determined in a later study to be due to the use of semi-kerfed and kerfless arrays during this study. For more information please see Chapter 5.

4.5 CONCLUSIONS

A 50 MHz sparse Vernier array was fabricated, and its performance was compared to a 64 element one-wavelength pitch phased array. The Vernier array was successful in suppressing the grating lobes 15 dB lower than the phased array while maintaining resolution that was as good as or better than the phased array. The relative sensitivity of the Vernier array was measured to be 18.2 dB lower than the phased array showing a limited ability for the Vernier array to image deep into a tissue-mimicking phantom. The low sensitivity of such a sparse array will ultimately limit the suitability of this array to low attenuation imaging applications.

Lastly, it is again interesting to note that the signal strength remains relatively strong at wide steering angles, suggesting that the directivity is better than one would expect from a kerfless design. The better-than-expected directivity is thoroughly investigated in Chapter 5.

CHAPTER 5:

EVALUATION OF KERFLESS ULTRASONIC PHASED ARRAYS

Evaluations of kerfless arrays with high levels of element-to-element mechanical coupling have qualitatively shown that these arrays produce broader directivity patterns than expected. Images generated with kerfless arrays were expected to show low signal levels at wide steering angles, but instead, significant signal levels were seen. Following these observations, the performance of kerfless arrays was therefore investigated and compared to a similarly constructed but fully kerfed and sub-diced array. A simulation model was constructed based on the impulse response method that includes the effects of the lateral coupling associated with kerfless arrays. The resulting model was in good agreement with experimentally measured array data.

5.1 PREAMBLE

This study is intended for publication in the IEEE-UFFC journal as a peer-reviewed journal and is currently in the process of being prepared for submission.

5.2 INTRODUCTION

Kerfless ultrasonic arrays are constructed without mechanical separation (kerfs) between the elements of the array. The array elements are defined solely by electrode patterning on the surface of a monolithic piezoelectric substrate. These arrays are attractive for high-frequency transducer designs with micro-scale element dimensions since they are simpler to fabricate. It is much easier to define high-resolution array elements by electrode patterning only, as opposed to micro-machining kerfs, and then applying an electrode pattern. Micro-machining phased arrays with oscillatory frequencies at 40 MHz and above requires

features that are so small that they approach the sizes of the molecular grains or domains of many conventional piezoelectric ceramics and crystals.

As with conventional low-frequency ultrasound array designs, it is typically necessary to sub-dice the array elements in order to avoid unwanted lateral modes. Sub-dicing the elements pushes lateral resonances to higher frequencies than the fundamental operating mode but imposes significant challenges and constraints on how the arrays are machined onto the piezoelectric substrate. For example, the 40 MHz phased array described in Chapter 3 has array elements that are 30 μm wide and about 50 μm thick. Cutting a 30 μm wide element in half without damaging the piezoelectric substrate is beyond the capability of most micro-dicing technologies. Because of this, kerfless arrays show improved element-to-element uniformity and present a more robust manufacturing process. Ultimately, the use of kerfless array techniques at higher frequencies can lead to higher yields and remove limitations on element sizes (Bezanson, Adamson, and Brown 2014; Wu et al. 2009).

Though kerfless arrays have several advantages during fabrication, several investigations into the performance of kerfless arrays have suggested that these arrays have poor element directivity (Morton and Lockwood 2002; Bezanson, Adamson, and Brown 2014; R. Chen et al. 2014; J. Cannata, Williams, and Shung 2005). These initial studies suggest that kerfless designs would not perform well for endoscopic transducers, where a high-directivity is required to image a large field of view.

Despite the previous work suggesting kerfless arrays were not suitable for phased array imaging, a high-frequency kerfless phased array was fabricated during an exploration of low-cost design techniques. When tested on tissue phantoms, these arrays show adequate levels of signal out to angles of $\pm\,32°$ without excessive levels of signal attenuation, contradicting expectations. The goal of this study was to gain a fundamental understanding of the performance trade-offs associated with kerfless designs and to demonstrate that kerfless phased arrays can generate images at wide steering angles without dramatically compromising image quality.

An impulse response model was developed that incorporated acoustic emissions from the laterally propagating waves that are inherent to a kerfless design. In addition to simulations,

a 45 MHz kerfless array, and a comparable 40 MHz array, with sub-diced and fully kerfed elements, were fabricated using a new laser dicing technique. The newly developed model showed good agreement with experimental results.

5.3   BACKGROUND AND MOTIVATION

An impulse response model was developed that incorporated acoustic emissions from the laterally propagating waves that are inherent to a kerfless design. In addition to simulations, a 45 MHz kerfless array, and a comparable 40 MHz array with sub-diced and fully kerfed elements, were fabricated using a new laser dicing technique. The newly developed model showed good agreement with experimental results.

Laser dicing of the array features was possible due to the recent acquisition of a purpose-built precision laser. This laser allows for finer features than can be achieved with conventional dicing techniques and removed many of the associated manufacturing constraints. However, kerfless arrays were still seen as a promising area of investigation as laser micromachining remains an expensive and time-consuming process. A comparison of the piezoelectric wafers in kerfless and fully kerfed arrays is shown in Figure 5-1.
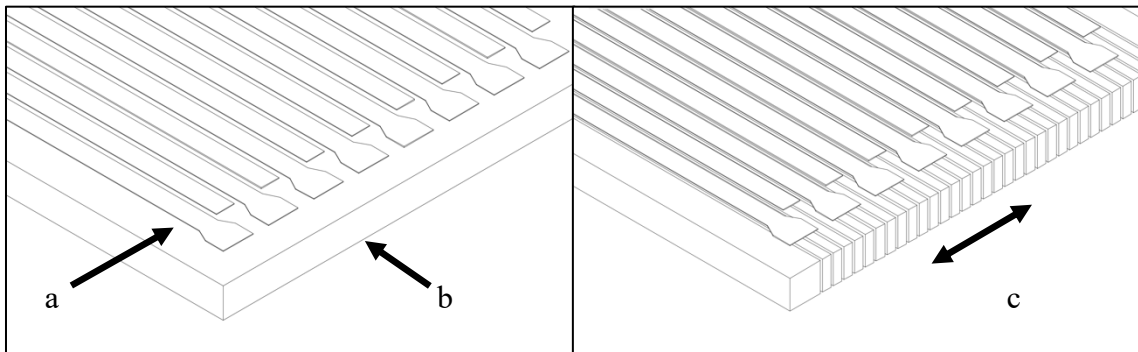
Figure 5-1: (Left) view of a kerfless linear array with electrical elements (a) patterned on the top surface of a uniform piezoelectric wafer (b). (Right) A kerfed and sub-diced array where the piezoelectric material is machined, and the gaps filled with soft epoxy. The patterned electrodes are featured with a slight fanout to facilitate wire-bonding of electrical interconnects. The kerfs prevent the lateral transmission of vibrations between elements, in the direction of (c).

Previous investigations (Morton and Lockwood 2002; Bezanson, Adamson, and Brown 2014; R. Chen et al. 2014; J. Cannata, Williams, and Shung 2005), have supported the

conventional theory of poor directivity for kerfless arrays. Two of these studies have measured element directivity from kerfless PMN-PT single-crystal arrays (Bezanson et al. Chen et al.), and two have measured PZT-5H ceramic arrays (Cannata et al. Morton et al.). Table 5-1 below summarizes the element directivity for the four studies.

Table 5-1: Summarized results for reported kerfless array directivities

Study	Directiv-ity (-6 dB)	Element Features (Width/Pitch/Frequency)	Notes
(Bezanson, Adamson, and Brown 2014)	± 15°	30 μm / 38 μm / 40 MHz	Kerfless PMN-PT
(J. Cannata, Williams, and Shung 2005)	± 11°	N/A / 100 μm / 32 MHz	Kerfless PZT-5H
(Morton and Lockwood 2002)	~ ± 9.5°	25 μm / 30 μm / 50 MHz	Motorola 3203HD
(R. Chen et al. 2014)	± 6°	25 μm / 33 μm / 40 MHz	Kerfless PMN-PT

All four of these studies concluded that kerfless arrays would not be able to image at wide steering angles effectively. However, the directivity measurements were done by pulsing a single array element and not by measuring the beamformed signal intensity. In addition, most of these studies only measured one-way directivity with a scanned hydrophone, with the exception being Morton et al., but where directivity was only measured to ± 15°.

This study presents the development of two forward-looking high-resolution arrays, where both designs provide an endoscopic form-factor. The process for fabrication of the designs is presented, and the performance is characterized. The simplified construction process provided by the kerfless array design was notably easier and faster to construct than the kerfed array. During the initial testing of the two designs, images of tissue phantoms were collected and are shown in Figure 5-2.

The kerfless array demonstrated much better directivity than the previous literature suggested. However, the kerfless array images showed dimming between 15 to 20°. The peak signal intensity for the kerfless array was significantly higher than the kerfed array, and so

the areas of dimming were able to be restored by applying an angle dependant gain (Figure 5-14 on page 111). Lastly, it should also be noted that the kerfed (and sub-diced) arrays have broader bandwidth pulses that contribute to higher axial resolution in these comparison images. So, despite the kerfless arrays performing better than expected, the sub-diced and fully kerfed arrays still present the best images at 40 MHz.
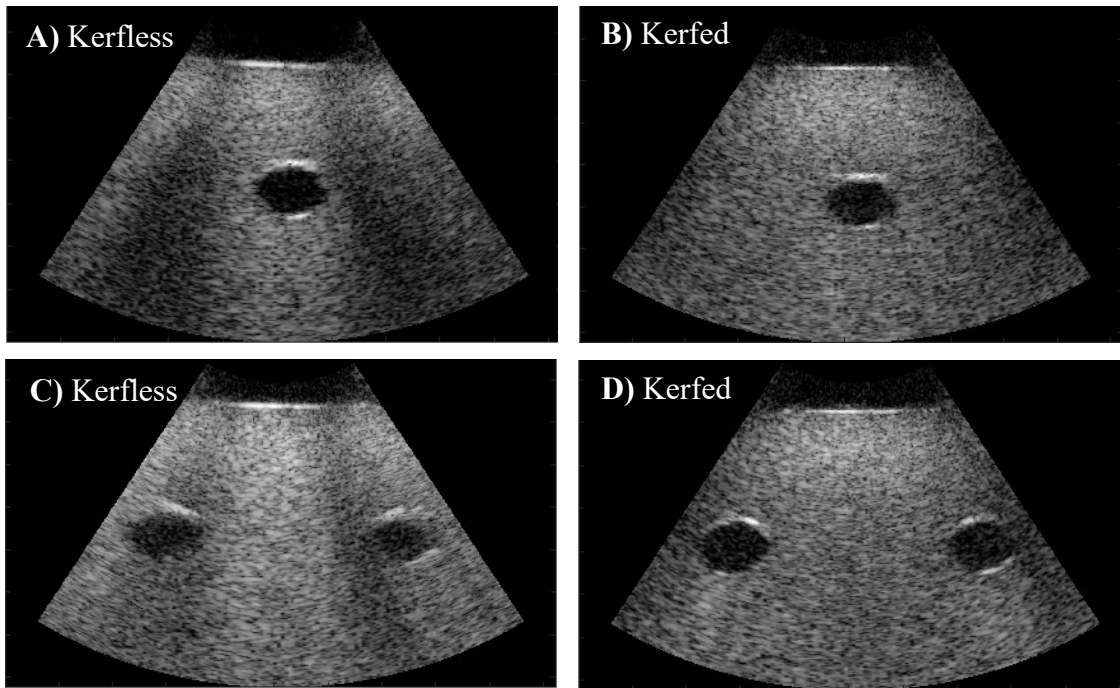
Figure 5-2: Tissue phantom in water with 0.7 mm internal voids as imaged by an (A) 45-MHz kerfless endoscopic array and (B) 40-MHz fully kerfed and sub-diced array. Images (C) and (D) show the images captured by the respective arrays for a phantom with a set of voids spaced 5 mm apart. Kerfless array images (A & C) show attenuated regions between ± 15 to 20°. However, the kerfless array images show strong signal at wider angles. Images collected with a 64-channel parallel beamformer configured for phased array pulse echo imaging as described in section 2.2.1

Single element directivity patterns were simulated using a conventional impulse response method to shed light on the unexpectedly wide directivity for the kerfless array. Figure 5-3 compares the modeled directivity to the experimental performance for both kerfless and fully-kerfed array designs. Though the fully-kerfed array performs similarly to the simulation, the kerfless array experimentally shows a sharp drop off similarly to the impulse response model, but then a subsequent increase in signal at angles past ± 20°. The simulation for the kerfless array was done by increasing the width of the single element to correspond

to the lateral clamping from the neighboring piezoelectric substrate. The single-element data for the kerfless array has nulls that correspond to the same steering angles as the dim regions in the beamformed tissue phantom images (Figure 5-2).
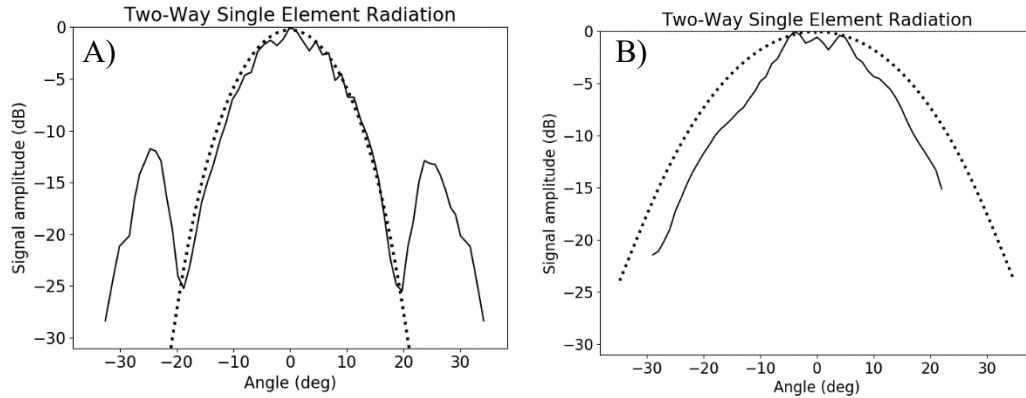
Figure 5-3: Shows the predicted versus measured directivity of a single element within the kerfless array (A) and a fully-kerfed and sub-diced array (B). The simulated directivity of the kerfless array (A – dotted line) was calculated using the impulse response function and an effective element size twice as large as the element electrode. When simulating the impulse response of the fully-kerfed and sub-diced array, an effective element size of the array electrode and the neighboring epoxy filled kerf was used to achieve the modeled fit as shown (B – dotted).

The initial simulation techniques were based on the previously developed impulse response model (SanEmeterio and Ullate 1992; Franco et al. 2011). The work presented in this study incorporates adaptations to the model that are necessary to accurately simulate and explain the observed performance of the kerfless arrays.

5.4   METHODS

The following sections provide a review of the current implementation of the impulse response model and propose an updated model for the simulation of acoustic radiation patterns for kerfless arrays where strong lateral coupling is present.

5.4.1   CONVENTIONAL SIMULATION METHOD

A Python script was developed based on the impulse response method as described in (SanEmeterio and Ullate 1992) and which was further optimized by the incorporation of the simulations techniques described in (Zou et al. 2016). From the simulation techniques

presented by Zou et al. (2016), the method of applying a circular test to the simulation geometry was taken. This idea was then simplified by applying the process described in section 2.3 and Figure 2-14.

The conventional simulation method, used initially in this work, implements the impulse response method to calculate the resulting pressure seen at spatial field points when the elements in the array are pulsed. For single element directivity patterns, the model only activates a single central element. For beamformed acoustic patterns, the model activates all elements in the array, with appropriate timing delays for focusing to a field point of interest, and the resulting pressures are summed linearly. The beamformed directivity plots are obtained by repeating the process while changing the delay profile to refocus to a new steering angle until the full range of steering angles is completed. The simulated pressure amplitude was normalized to the $0°$ steering angle for both the single-element case and the beamformed case.

The basic geometry of the impulse response simulations is shown in Figure 5-4, where the simulation calculates the acoustic pressure transmitted by the array elements $E_{1:N}$. The impulse response function from each array element to each point in the field is calculated, and the convolution of the impulse response with the transducer's excitation function is used to find the resulting pressure waveform at each point along $X_{1:I}$

The results of this model, for the single element directivity, are shown by the dotted lines in Figure 5-3. The model was adjusted to fit the experimental results by increasing the element width in the simulation to emulate the lateral clamping inherent to kerfless arrays. Therefore, the simulation accounts for lateral effects that broaden the active portion of the array element. However, this model does not provide a mechanism for including the propagation of a lateral waves within the piezoelectric wafer and the effects of the acoustic waves emitted, into the imaged medium, by those lateral waves.
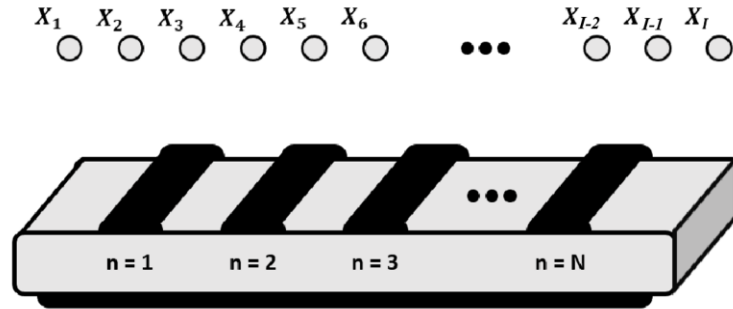
Figure 5-4: An illustrative example of the simulation geometry used to predict the acoustic radiation patterns emitted from ultrasonic arrays. Points X_1 to X_I represent the field points spanning the focus of the array. The acoustic pressure seen at a given focal point is obtained by summation of the acoustic pressure waveforms emitted by each active element in the ultrasonic array

With the standard simulation method, two-way radiation patterns are computed by taking the acoustic pressures seen at each field point along $X_{1:I}$ and re-convolving with the impulse response function, calculating the pressure returned to the array's elements.

5.4.2   A NEW SIMULATION METHOD FOR KERFLESS ARRAYS

It is hypothesized that kerfless arrays differ significantly from conventional arrays due to the high levels of mechanical coupling between adjacent elements. Since the conventional simulation failed to predict the experimental behavior accurately, we theorized that the existing simulation method was failing to consider a significant acoustic characteristic of kerfless arrays – the propagation lateral waves after an element pulses and the acoustic waves emitted by these lateral waves as they travel across the piezoelectric wafer.

The fit between the fully-kerfed directivity data and existing simulations suggested that this characteristic is not significant in the fully-kerfed array designs. We hypothesized that the wide directivity of kerfless arrays and destructive null in their directivity pattern were related to how acoustic emissions from lateral waves within the piezoelectric wafer were interacting with the primary acoustic pulse of each element. The following section presents an adaptation to the conventional impulse response model for the inclusion of the effects of lateral waves and compares the results to experimental datasets from physical arrays.

In the kerfless model, it is theorized that the vertical motion of an array element causes a lateral contraction in the piezoelectric wafer due to the Poisson effect whereby a vertical

97

expansion would cause the active portion of the wafer to contract laterally. Therefore, as an element is activated within a kerfless array (Figure 5-5.B), this generates a lateral wave that travels along the array causing neighboring elements to emit acoustic waves (Figure 5-5.C and Figure 5-5.D). It is important to note that because of the Poisson effect, the activation of neighboring elements will have an inverted amplitude relative to the main pulse.
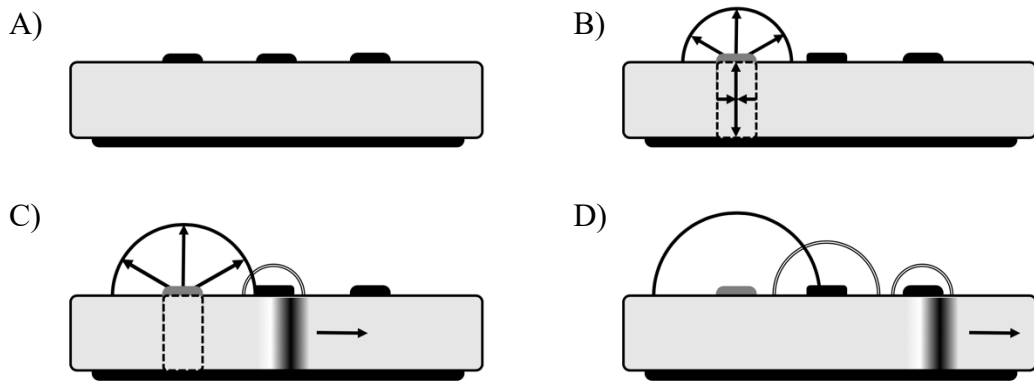
Figure 5-5: Shows the general principle of the updated kerfless model, where an element of an ultrasonic array (A) is excited, causing the radiation of an acoustic wave. The vertical expansion of the ultrasonic element causes the lateral compression of the active portion of the array's piezoelectric. This lateral wave then propagates along the kerfless piezoelectric wafer (C) causing the acoustic excitation of adjacent elements and the emission of acoustic waves with inverted amplitude (C) and (D) from neighboring elements

Figure 5-6 shows a simplified two-dimensional model of the resulting acoustic emissions described in Figure 5-5, where the array elements are modeled as point-sources on the piezoelectric wafer's surface. The simplified simulation in Figure 5-6 models the one-way acoustic pressure at all field points in the 2D pressure field resulting from the firing of a point source (Figure 5-5.A) and the interference of the resulting wave with the waves (Figure 5-5.C) of inverted amplitude emitted from the lateral wave along the piezoelectric wafer (Figure 5-5.B).

It is worth noting that Figure 5-6, and the simulation used to create it, only exist to help describe and communicate the model discussed in Figure 5-5. Though Figure 5-6 may help

to give an intuitive sense of the effects that are being modeled, it has been heavily simplified. Figure 5-6 omits the effects of the impulse response function, and it does not simulate to the focal depth of the transducer. Despite these simplifications, this illustrative example begins to show why attenuation is seen in the single element directivity patterns at 15 to 20° and how the lateral coupling can constructively interfere with the main element pulse to cause the signal intensity to increase at angles past 20°.
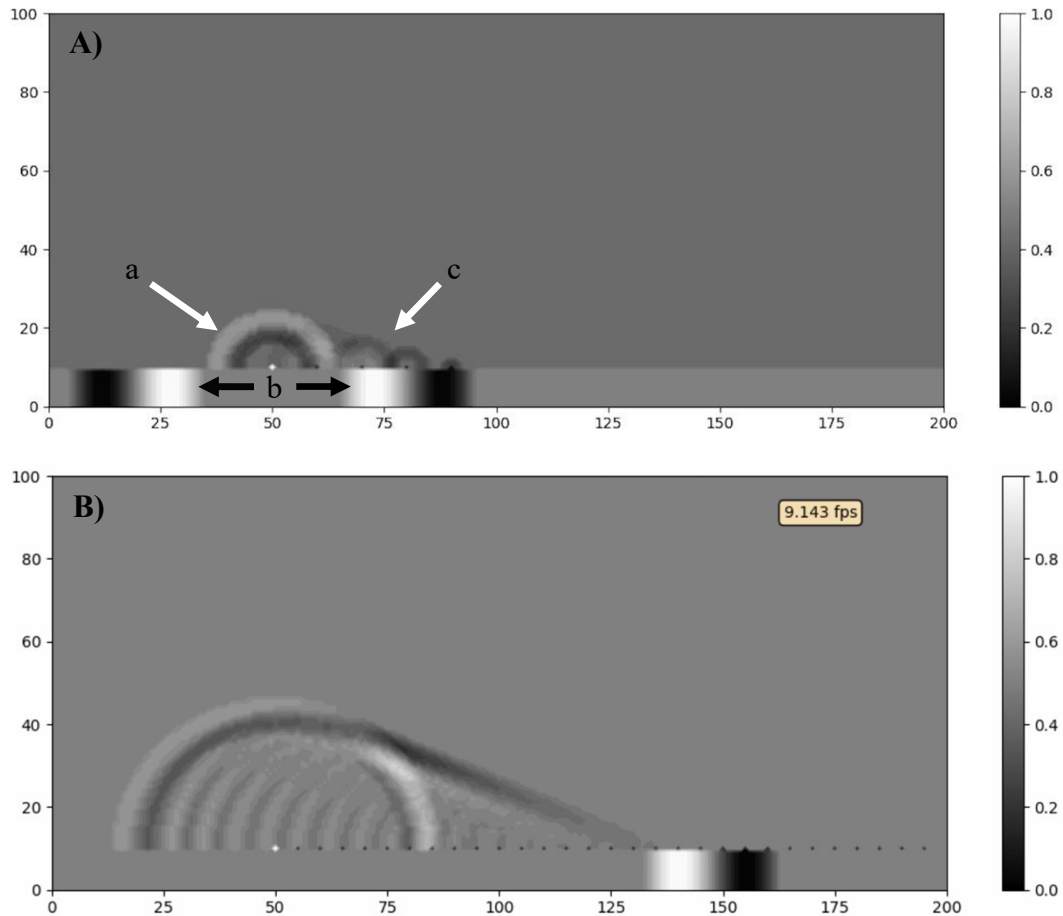
Figure 5-6: Simulation of the acoustic radiation patterns of a kerfless array element when the lateral coupling is taken into consideration. The lateral wave within the piezoelectric material causes the emission of a plane wave that interferes with the spherical wavefront from the initial element pulse.

In this model, the acoustic emissions from neighboring elements result in a plane wave of inverted amplitude to the main element pulse, angled according to Equation (5-1):

$$\theta_{plane} = sin^{-1}\left(\frac{c_{water}}{c_{piezo}}\right) \qquad (5\text{-}1)$$

The acoustic component due to the lateral coupling of an element to its neighboring elements is modeled as having attenuation α_{mech}, and a propagation velocity c_{piezo}, which corresponds to the lateral speed of sound in the array's piezoelectric material. Therefore, the time delay from one element's excitation to the excitation effect on neighboring elements is offset by a time delay corresponding to:

$$T_{offset} = \frac{(array\ pitch) * (n - n_x)}{c_{piezo}} \qquad (5\text{-}2)$$

When the impulse response model is updated to account for the lateral coupling, the resulting directivity pattern shown by the dashed line on Figure 5-7.B is predicted for a single element in a kerfless PZT-5H array. The step by step computational process for the updated model is described in Table 5-2. The lateral modes are accounted for by summing the pressures at a given point X_i from, firstly, the main element and, secondly, the laterally coupled emissions with inverted amplitude, attenuation, and timing offsets.
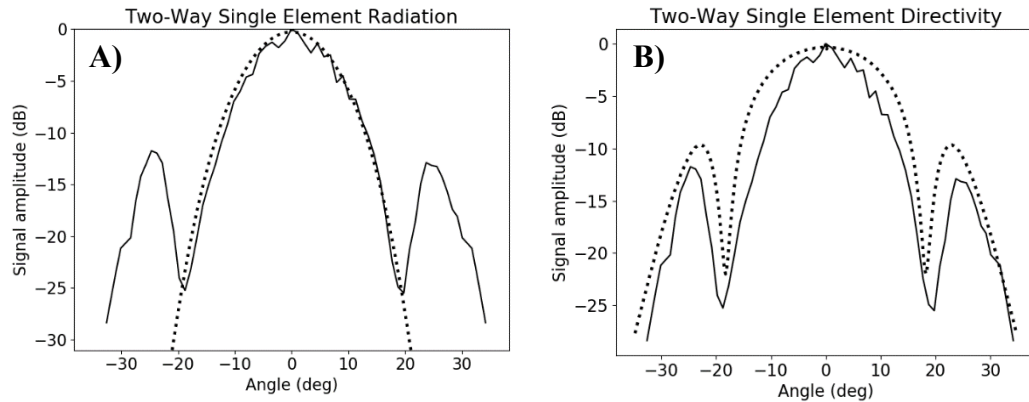
Figure 5-7: (Left) Shows the conventional impulse response simulation model's prediction for a single kerfless array element radiation and compares it to the measured data (solid). (Right) Shows the measured single element directivity (solid) and compares the simulated result (dotted) for a kerfless array when the lateral coupling is taken into consideration. The single-element simulations utilize an attenuation factor of -5.5 dB per lateral element with regards to the lateral wave.

The simulations shown in Figure 5-7 were run with an attenuation factor of -5.5 dB per lateral element for the lateral wave, a lateral speed of sound of 4580 m/s for the PZT-5H

piezoelectric wafer, as obtained from (K. K. Shung, Cannata, and Zhou 2007). As can be seen in Figure 5-7, we achieve a very close match between the simulated element directivity and the experimentally measured directivity. The simulation predicts the destructive nulls and the increased signal amplitude at the wider angles. To model the directivity of the array elements an element width of 38 μm was used for the kerfless array and the actual element width of 28 μm was used for the kerfed array.

Table 5-2: Computational process

Step	Step Description	Notes	Eqn Ref:
1	Determine the transmit velocity profile at each element in the array	$V_{(t)0} = Ct^3 e^{-kft} \cos(2\pi ft)$	(5-3)
2	Calculate resulting acoustic pressure seen at all field points from excitation of active elements	$P_{i,n} = \rho \dfrac{\partial V_{(t)}}{\partial t} * h_{(n \to i)}$	(5-4)
3	Sum acoustic emissions from lateral waves	$P_{i,n,p} = -\rho \dfrac{\partial V_{(t)}}{\partial t} * h_{(n \pm p) \to i}$	(5-5)
4	Calculate resulting acoustic pressure seen at each field point from all active elements and laterally coupled elements	$P_i = \sum P_{i,n,p}$	(5-6)
5	Calculate the resulting two-way pressure at each element of the array	$P_n = P_i * h_{(i \to n)}$	(5-7)
6	Add beamforming delays to determine the acquired signal	$P_t = P_n(t + t_{delay})$	(5-8)
7	Apply the Hilbert transform of the received data to determine acoustic signal intensity	$I_t = abs \left(\dfrac{1}{\pi} \int_{-\infty}^{\infty} \dfrac{P_t(\tau)}{t - \tau} d\tau \right)$	(5-9)

5.4.3 ARRAY FABRICATION

To verify the simulation results, a high-frequency kerfless array and a fully kerfed and sub-diced array were constructed and tested out of a PZT-5H piezoelectric substrate. The fully kerfed and sub-diced array was fabricated so that performance degradation, from the lateral coupling, could be investigated. The two arrays were fabricated from the same piezoelectric wafer, and as a result, the fully-kerfed and sub-diced array had a slightly lower center frequency since the sub-dicing lowers the speed of sound in the thickness dimension. The final frequencies were 40 MHz for the kerfed array and 45 MHz for the kerfless array.

The first step in the fabrication process was to sputter a 1.5 μm layer of copper (Mantis Sputtering and E-Beam Deposition System, Mantis, UK) onto a 200 μm thick wafer of PZT-5H. The wafer was prepared for sputtering by lapping with 3 μm slurry on a PM5 lapping machine (Logitech, UK) and seeding the surface with a 500 nm layer of chrome through E-Beam evaporation (Mantis Sputtering and E-Beam Deposition System, Mantis, UK). Once the electrode was deposited, the wafers were mounted to a glass disc using a thin layer of crystal bond (Logitech, UK) at 125 °C and 2 kg bonding pressure. The sample thickness was measured before and after bonding to ensure the bonding layer thickness was less than 1 μm.

After bonding, the PZT-5H wafers were lapped to their final thickness of 50 μm using 3 μm slurry on the PM5 lapping machine. At this stage, a layer of Kapton tape was placed over the wafer and patterned using a 355 nm pico-second laser, Oxford Series-A (Oxford, UK). The tape mask was removed from the active area of the ultrasonic arrays, and a 1.5 μm ground electrode layer of copper, with a 500 nm seed layer of chrome, was applied using the Mantis deposition system.

With the ground electrode applied, the Kapton mask was removed, and alumina loaded insulating epoxy (2-grams Al-O3 to 1-gram Epo-Tek 301 epoxy) was applied over passive areas of the wafer. Once the insulating epoxy layer was set, a conductive epoxy (E-Solder No 3022, vonRoll USA) backing was applied to a thickness of 2 mm. The wafer and backing layer assembly block was then released from the glass disc and mounted in the pico-second laser dicing system for patterning of the ultrasonic array electrodes. The wafer was

sized to allow for nine arrays to be fabricated: six kerfless array patterns and three sub-diced and fully kerfed patterns.

The array patterns were identical in geometry to the photolithographically patterned arrays described in Chapter 3, with 64 elements spaced at a 38 μm pitch and a small electrode fan-out to wire-bonding pads. To pattern the ultrasonic array electrodes, the laser was programmed with a drawing exchange format (DXF) file detailing the desired electrode geometry for the arrays and produced using AutoCAD Fusion 365 (AutoDesk, USA). For the three sub-diced and fully kerfed arrays, the laser was programmed to complete a kerfing pass after completing the array electrodes with a 3 μm kerf-width for both the sub-dicing and element separation passes, shown Figure 5-8 (right). The one-of-a-kind custom-built laser dicing system was not accessible during the previous studies described in Chapters 3 and 4. The array kerfs are then filled with Parylene-C (Specialty Coating Systems, USA) during the application of the acoustic matching layers.
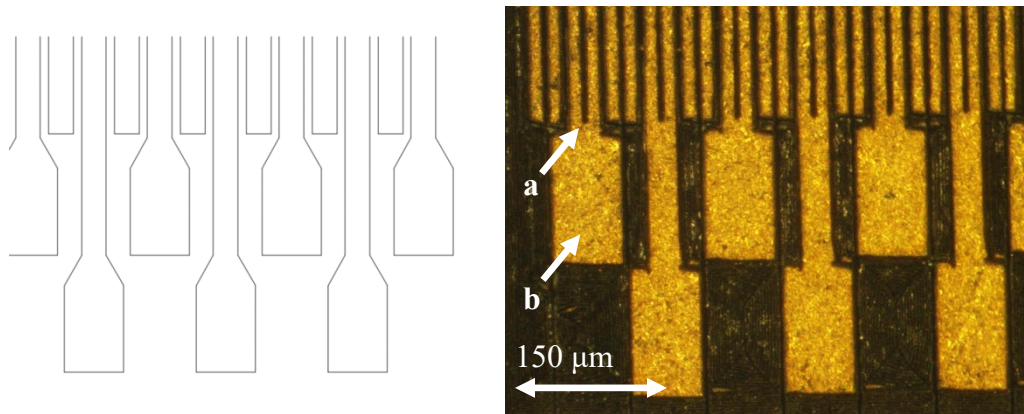
Figure 5-8: (Left) Draft of corner quadrant of array pattern with bonding pads for kerfless array, with no sub-dicing of array electrodes. (Right) A laser patterned array with kerfed and sub-diced array elements. The kerfs (a) stop short of the wire-bonding pads (b) in order to prevent poor quality adhesion during the wire-bonding process.

The arrays blocks with backing layers were then diced out of the wafer block and mounted to a custom PCB interposer, as discussed by Bezanson et al. (2014). Matching layers were then deposited using alternating layers of Parylene-C and copper that emulates a dual ¼λ layer design using a mass-spring resonance. Initial layer thicknesses were determined using the methods presented in (Brown et al. 2014) and as discussed in Appendix D. The layer thicknesses were then modeled using the KLM model and adjusted to achieve a two-way

pulse-echo bandwidth of 50%. The layer thicknesses and composition are listed below in Table 5-3.

Table 5-3: Array matching layer thicknesses

Layer	Thickness (μm)	Material
Kerfed - Spring	2.0	Parylene
Kerfed - Mass	2.8	Copper
Kerfed - ¼λ Matching	11.0	Parylene
Kerfless - Spring	2.4	Parylene
Kerfless - Mass	3.0	Copper
Kerfless - ¼λ Matching	12.0	Parylene

The use of a vacuum deposition mass-spring and ¼λ matching layer technique was selected due to the high-frequency (40 MHz) of the arrays. At these frequencies, the imperfections associated with traditional bonded matching layer application procedures become a significant impediment to the operation of the transducer. As a side note, the conformal nature of the Parylene C spring layer resulted in the array kerfs filling with Parylene C during vacuum deposition.

Following the application of matching layers, a resin lens (Alumilite Water-Clear, Alumilite Corporation, USA) with a speed of sound of 2300 m/s, was cast onto the distal end of the array, with a specific radius of curvature, R_c, for a focal depth of 6.5 mm. The process for determining the required radius of curvature is originally discussed in section 2.2.8, and a characteristic example is presented in Appendix D.

When completed, the arrays were connected to a 64 channel in-house developed beamformer through a commercially available ultrasonic cabling solution, the 128 channel Comfort+ cable (TE Connectivity, USA). The distal end of the cable is connected to the array's electrical interconnect using surface mount mezzanine connectors. The cable provides a 75 Ω characteristic impedance and has a total length of 2.4 m.

5.5 Array Testing Methods and Results

The arrays were tested for directivity to ensure a good fit with the expanded model. Radiation patterns were also collected at various angles to ensure adequate performance for imaging. The electrical impedances of the array elements were collected to ensure a good electrical fit with the drive electronics. Additionally, the pulse-echo waveforms were measured to ensure that the pulse waveform used for simulation was a good match to the actual pulse waveform.

5.5.1 Pulse-Echo

The pulse-echo data was captured for both kerfless and fully-kerfed array designs. The data was collected by positioning a wire-phantom at the transducer focus and pulsing a single element using a single channel pulser-receiver. The pulser received the return signal, applied +23 dB of signal amplification, and output the resulting waveform to an MSOX-3104 oscilloscope (Keysight Technologies, USA) for data capture. The FFT was calculated using the built-in FFT function on the oscilloscope and saved to a USB drive with the pulse-echo waveform. Pulse echo signal intensity and spectrum data were plotted using Excel™ (Microsoft, USA), Figure 5-9.
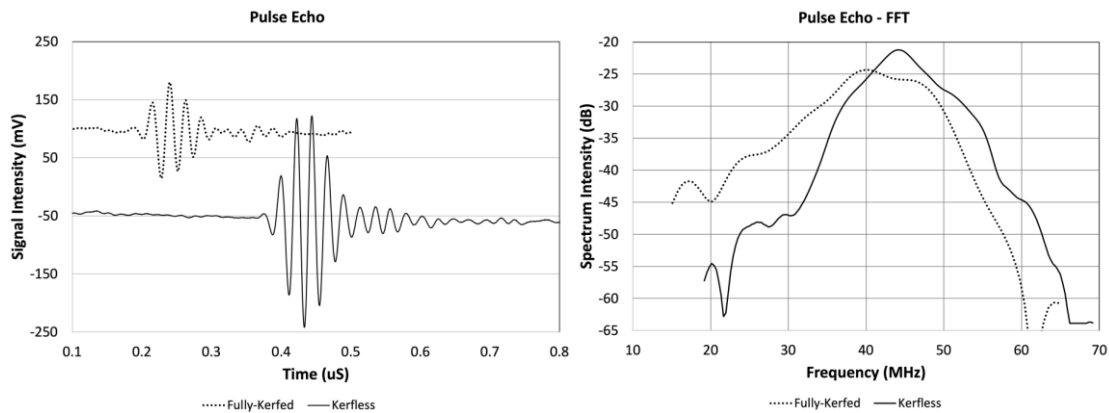
Figure 5-9: Sub-diced versus kerfless array single element pulse-echoes (left) and spectrum (right) captured off of a wire phantom located at the focal depth of 6.5 mm and with a steering angle of 0°

The single element pulse-echo from a kerfless array showed a peak-peak pulse amplitude of 364 mV, whereas the sub-diced and fully kerfed array showed a peak-peak pulse

amplitude of 165 mV. The sub-diced array showed a -6 dB bandwidth of 40%, whereas the single element kerfless array pulse-echo data showed a reduced pulse bandwidth of 26%. The measured bandwidth was significantly lower than the 50% bandwidth predicted with the KLM model. It is suspected that the reduced bandwidth resulted from the use of a long cable assembly, connecting the array to the beamformer and narrowing the bandwidth around the transducer's resonance frequency. In future designs, a cable model can be developed and incorporated into the design of the matching layer system to improve the pulse bandwidth and axial resolution further.

5.5.2 SINGLE ELEMENT DIRECTIVITIES

Single element directivities were measured by attaching the ultrasonic array to a three-dimensional positioning stage and aligning the ultrasonic array above a 25 μm aluminum wire phantom in water located at the lens focus of 6.5 mm, Figure 5-10. The wire was aligned at the focus, with the wire perpendicular to the image window, appearing as a point reflector. The array was connected to a single channel pulser (Daxsonics Ultrasound Inc, Canada) and pulsed. The pulser received the return echo, applied amplification, and the signal was passed to an MSOX-3104 oscilloscope (Keysight Technologies, USA) for signal amplitude measurement. The positioning stage was used to scan the array laterally, and the signal amplitude was collected at angles between ± 32° in 2° steps but scanned at a constant depth in order to remain at the lens focal depth.
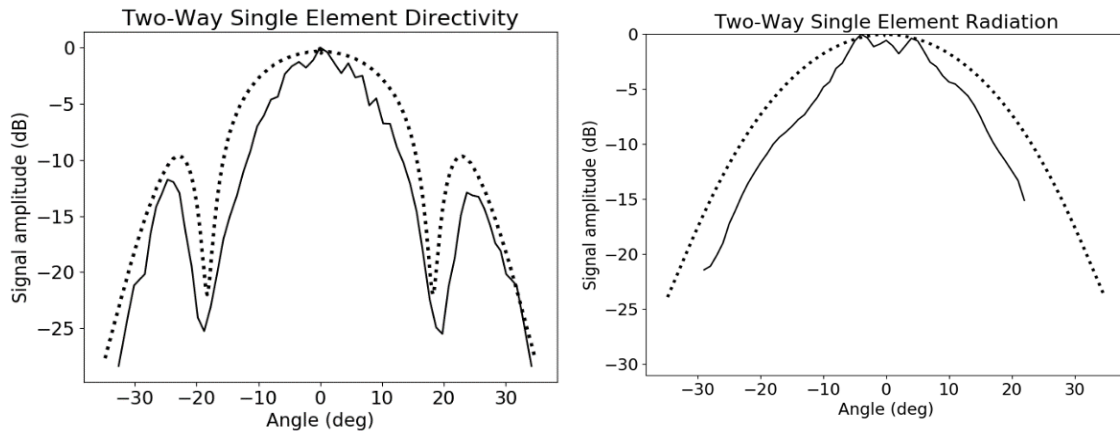
Figure 5-10: Two-way single element directivity plots for kerfless (left) and fully-kerfed (right) array designs. The collected data (solid line) is plotted against the simulated response (dashed line). The simulation difference between the kerfless array and the fully-kerfed arrays differ in that the kerfless array simulation uses a center frequency of 45 MHz and simulates five lateral wave emissions. The fully-kerfed array simulation is completed for a pulse center frequency of 40 MHz and does not simulate any acoustic energy radiated by lateral waves

The collected data, shown in Figure 5-10, was first filtered using a matched filter centered at the pulse frequency with a passband of $\pm$ 15 MHz around the center frequency. The data were smoothed, and the signal centered about 0°, compensating for physical misalignments in the test setup. The data was plotted against the simulated data. Since the reflector was scanned linearly at a constant depth, there is an increased path length angle. Diffraction causes a loss in the signal that is inversely proportional to path-length, and so the two-way signal amplitude had an angle dependant gain of $1/\cos(\theta)$, applied to compensate for diffraction effects. For example, the signals from a reflector located at 30° would have traveled a distance 15.5% farther than signals from a reflector at 0°, and so a gain of 1.15 is applied.

5.5.3 BEAMFORMED PEAK SIGNAL PRESSURE AS A FUNCTION OF ANGLE (BEAMFORMED DIRECTIVITY)

The beamformed directivities were collected in a method similar to the single element directivities, but instead of using a single-channel pulser, the array was connected to an in-house developed 64-channel beamformer. The beamformer recorded the pulse-echo signal as the array was scanned laterally over the wire-phantom in 4° steps. The collected pulse-

107

echo data was up-sampled to 400 MSa/s and filtered using a discrete band-pass filter (Gaussian envelope, 75% bandwidth) centered at the pulse frequency with a passband of ± 15 MHz centered around 40 MHz. The peak pulse-echo intensity was then recorded for each location and plotted. The Gaussian filter is defined by:

$$\cos(2\pi \cdot f_c \cdot t)\, e^{-\dfrac{-t^2}{2*(2\sqrt{\frac{\ln(2)}{2\pi f_c \cdot BW}})^2}} \tag{5-10}$$

and was implemented using a post-processing script. The plotted data was smoothed using a three-point rolling average, and the signal was centered about 0° compensating for physical misalignments in the test setup. The experimental data was plotted against the simulated data. The received amplitude had an angle dependant gain applied of 1/cos(θ) to compensate for path length dependant attenuation. The collected and smoothed data is shown in Figure 5-11.
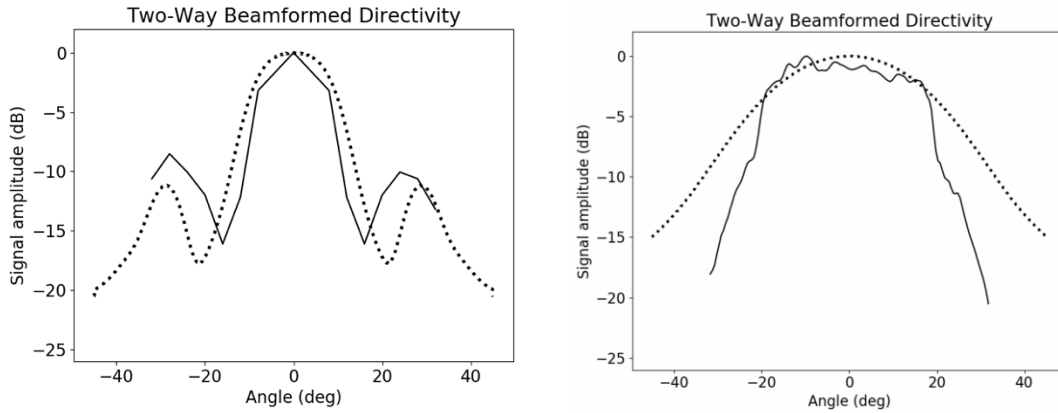
Figure 5-11: Two-way beamformed peak signal pressure relative to steering angle for the kerfless phased array (left) and sub-diced and fully kerfed beamformed array (right). Collected by measured returned signal strength off a wire-phantom scanned across the array focus in 4° increments.

5.5.4 RADIATION PATTERNS

Radiation patterns were collected by positioning the wire-phantom in a water tank at 0, 15, and 30° angles at a depth of 6.5 mm. The array was connected to the real-time 64-channel beamformer that controlled transmit and receive events and provided measurements of the peak signal intensity for all angles, while the phantom was located at the positions noted above. The measured and simulated dataset are shown below in Figure 5-12.
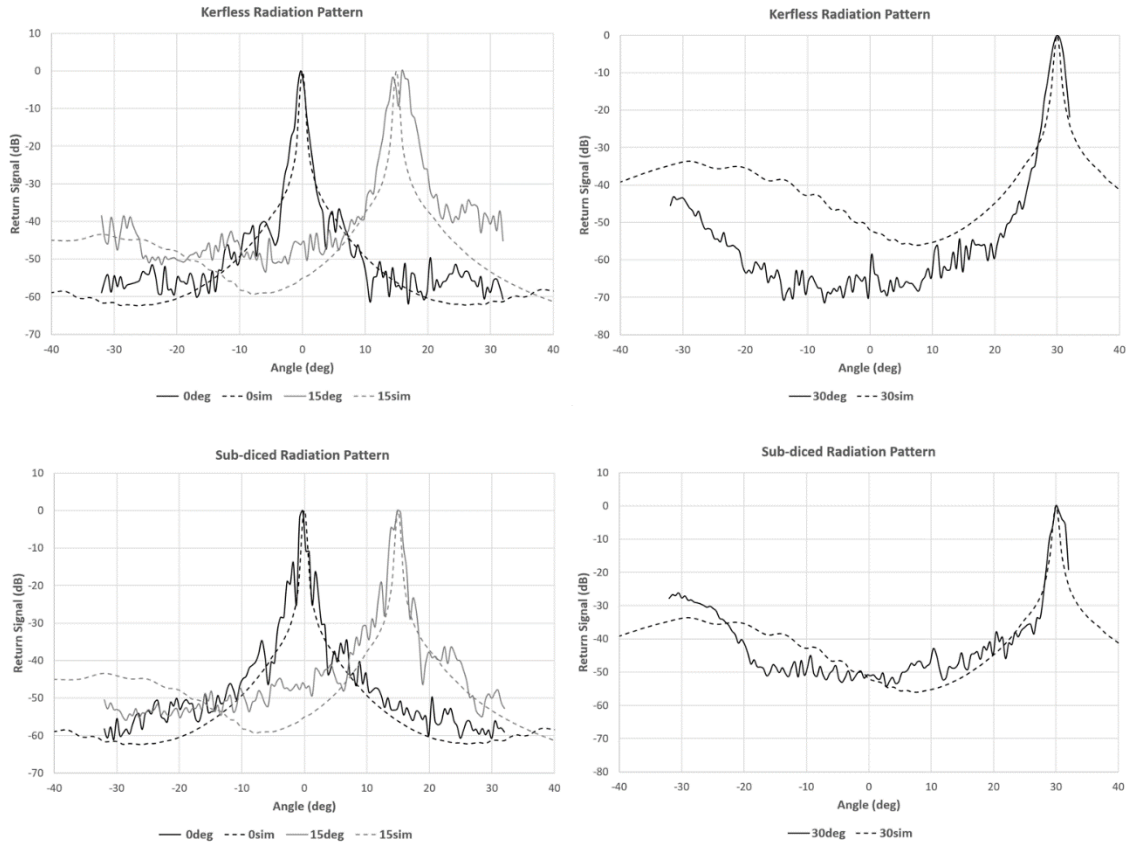
Figure 5-12: Radiation patterns of kerfless (top row) and fully-kerfed (bottom row) at 0, 15, and 30° positions with simulated (dashed) and measured (solid) datasets

Both the kerfless array and kerfed array had very good radiation patterns that were similar to the impulse response simulation. Most of the secondary lobes in the radiation patterns approach -60 dB except for the Kerfless array at 15°, which is limited to approximately -50 dB and the kerfed array at 30°, which is limited by its directivity.

5.6 DISCUSSION

In this work, the acoustic radiation of kerfless linear phased arrays was examined and compared to newly developed impulse response simulations that incorporate a laterally propagating wave in the piezoelectric substrate. It was found that kerfless PZT-5H arrays have considerably more signal strength at high steering angles (beyond ± 20°) than was expected. The inclusion of the simulated acoustic emissions from lateral oscillatory modes, within kerfless phased arrays, showed a strong fit with measured data (Figure 5-11).

Because of the simplicity of kerfless array fabrication, the better-than-expected beam-steering ability was an encouraging finding.

5.6.1   COMPENSATING FOR DIRECTIVITY NULLS

It is worth noting that the tested kerfless array produced a much higher signal level than the sub-diced and fully-kerfed array, presumably due to the reduced active area of and increased impedance of the sub-diced elements within the fully kerfed array (Figure 5-9). The beamformed directivity plot, shown in Figure 5-13, results when the kerfless array data is plotted on the same scale as the kerfed array.

Beamformed Directivity
Two-Way Wire Phantom - Normalized to Kerfed Array Signal
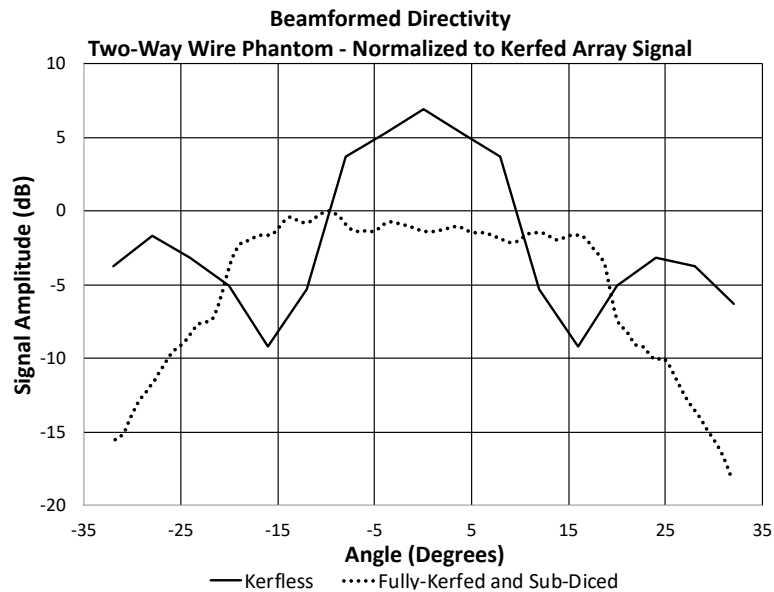
Figure 5-13: Comparison of kerfless and fully kerfed array signal intensity and directivity when normalized to the maximum signal of the fully kerfed array's peak signal intensity

Though the kerfless array provides significantly higher signal levels at low steering angles (>6 dB) than the sub-diced and kerfed array, it suffers from high variability in the signal intensity that is dependant on the angle of returned echoes. This causes the resulting image to have artifacts such as the dark bands seen Figure 5-14.A. However, an angle dependant gain can be applied to the returned kerfless array data as the relative attenuation as a function of steering angle is known. Figure 5-14 shows an experimental image of a tissue phantom before and after applying an angle dependant gain to produce a more uniform image.

110

This compensated image shows great promise for improving the functionality of kerfless phased arrays and demonstrates that the image quality, from kerfless phased arrays, can approach that of a fully kerfed array.

However, in contrast to fully kerfed arrays, kerfless arrays are much easier to fabricate. Not only is a custom-built pico-second laser micromachining system extremely costly, but it also takes approximately 2 hours per array to perform the laser cutting. In many intra-surgical and intra-vascular applications, the probes are designed to be single-use disposables, due to the challenges in device sterilization. The high cost of the laser dicing system and long processing time of the micro-machining could easily make the difference allowing for feasible commercialization of high-frequency single-use transducers.
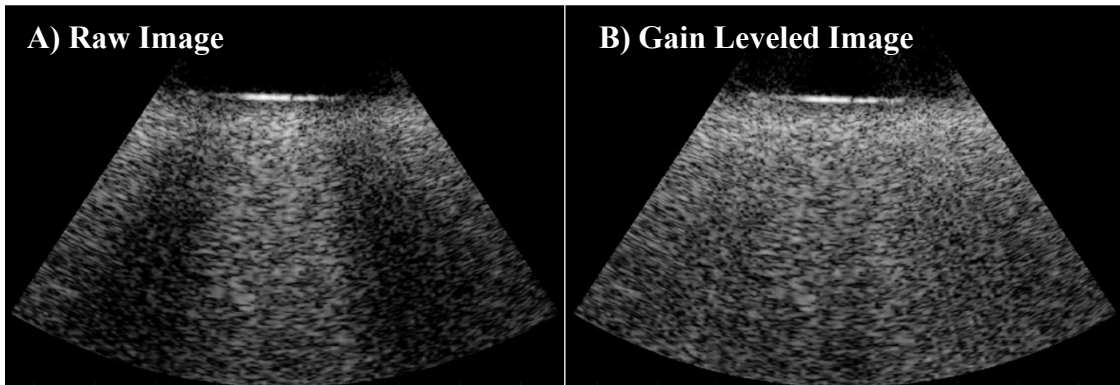
Figure 5-14: Tissue phantom produced by a kerfless array (A), and the same image with angle dependant gain leveling (B). Though the dark bands in image (A) represent a significant image artifact, the effects of this artifact can be removed through the application of an angle dependant gain. Since the signal attenuation as a function of angle is known, this process can be implemented on any image produced by a kerfless array

5.6.2 LOW-FREQUENCY MODE

The beamformer used for data collection in this study implemented filtering and sampling techniques that were tuned for probes operating at 40MHz with moderate pulse bandwidth, of around 50%. Additionally, the beamformer was used in its stock configuration for most data-collections presented above. However, when the data processing was by-passed and the peak signal intensity computed from raw data, the data shown in Figure 5-15 is obtained.
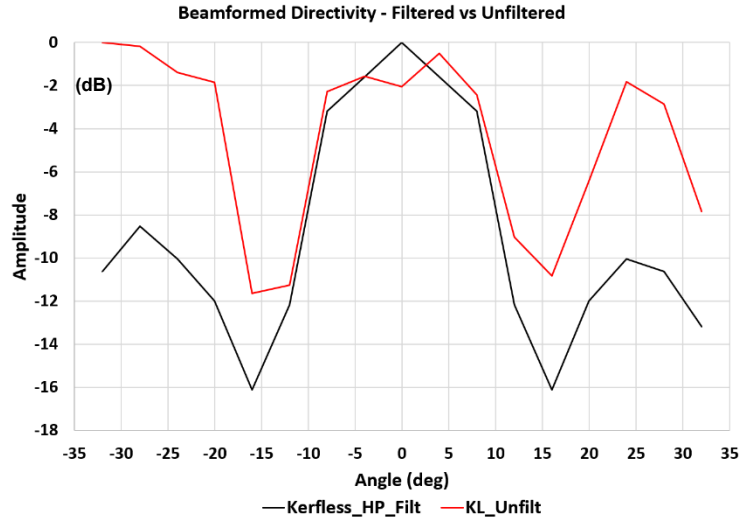
Figure 5-15: Filtered (black) and unfiltered (red) array directivities. When the receive electronics are configured to record a wide-band return signal, the signal attenuation at high steering angles is significantly decreased (red).

As shown in Figure 5-15, the unfiltered dataset shows the significantly stronger signal at wider angles than the stock, filtered dataset. It is hypothesized that the increased signal is due to a low-frequency component of the signal that is filtered out under normal operation. To investigate this, single element pulse-echo datasets were captured for the kerfless array with the wire-phantom located at 0° and 25° as shown in Figure 5-16.
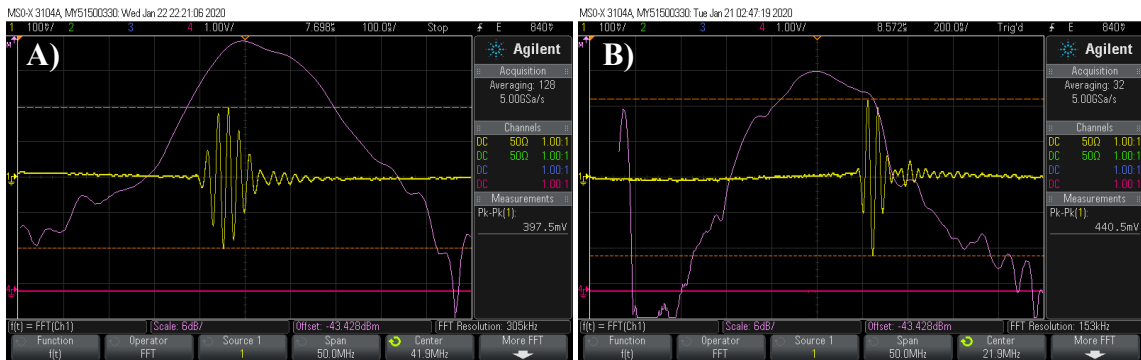
Figure 5-16: Single element pulse-echo captures at 0° (A) and 25° (B), the pulse captured at 25° shows a significantly lower center frequency (21 MHz at 25° instead of 41.9 MHz at 0°). Both pulses have a -6 dB bandwidth of approximately 10 MHz, but at 20 MHz, this translates to a fractional bandwidth of 50% whereas the 40 MHz pulse, collected at 0°, has a fractional bandwidth of 25%.

The captures shown in Figure 5-16 suggest that the pulse, at wider steering angles (B), has a reduced center frequency (22 MHz instead of 50 MHz). Future work may allow for the beamformer to take advantage of this low-frequency component to expand the field of view at high steering angles (Figure 5-17).

The lower-frequency mode, at ½ f_c, begins to dominate the return signal at wide steering angles, where grating lobes begin to become a significant issue. Advantageously, this effect may cause attenuation of the grating lobes or it may widen them to where they fall outside of the image window. Although beyond the scope of this thesis, it is imagined that a technique for kerfless arrays could be developed that utilizes an angle-dependent filter to remove grating lobes by filtering out the signal from the transducer's center frequency, f_c, at high steering angles where the low frequency pulse, at ½ f_c, dominates.
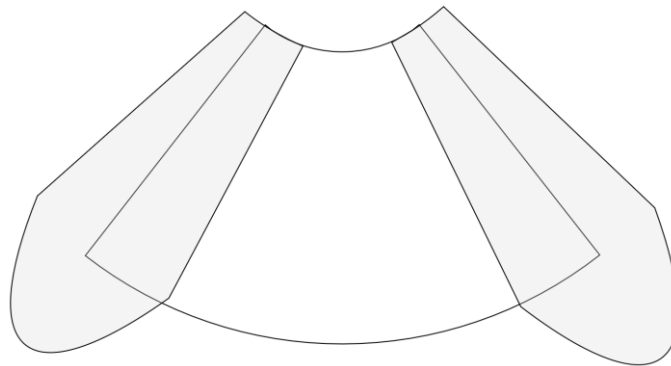
Figure 5-17: Illustrative depiction of the approximate zones (shaded) where the low-frequency signal component may allow for an increased field of view or improved SNR.

It is worth noting that the initial simulations suggest that this low-frequency mode may be caused by the interference of the radial pulse from an element interfering with the emissions from the lateral wave. However, it may also be caused by a shear mode induced from the laterally propagating wave-front or a sub-harmonic mode of the fundamental.

5.6.3   KERFLESS PMN-32PT SINGLE CRYSTAL ARRAYS

An interesting result is shown in Figure 5-18, where the simulated performance is shown for a kerfless PMN-PT array (dotted) and compared to the simulated performance of a PZT-5H array (dashed).

Effects of Lateral Mode on Directivity for PZT-5H and PMN-PT

Legend: --- PZT-5H .... PMN-PT —— Both Without Coupling
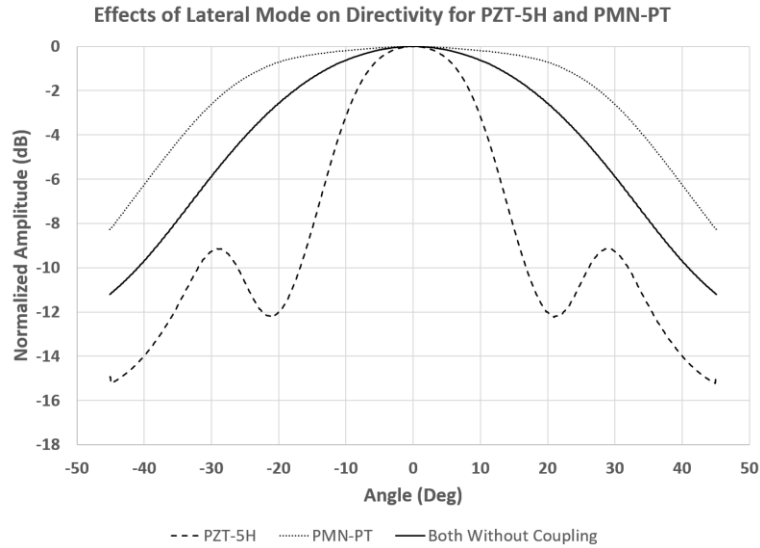
Figure 5-18: Simulations comparing expected peak beamformed signal pressure patterns for fully kerfed and sub-diced array (solid line), kerfless PZT-5H array (dashed) and kerfless PMN-PT array (dotted). Datasets normalized to each array's signal pressure when focused to 0°.

In Figure 5-18, both PZT and PMN-PT arrays have the same directivity prediction when lateral modes are not accounted for (solid), this method is used when simulating fully-kerfed and sub-diced arrays due to the high levels of lateral attenuation. However, when lateral modes are accounted for, we see a boost in the directivity for a PMN-PT array. The very different predictions for kerfless PZT and PMN-PT are the result of the vastly different lateral speed of sound in the two materials (1540 m/s in PMN-PT (R. Chen et al. 2014) and 4560 m/s for PZT). However, the beamforming delays may need to be updated to take advantage of this in practice as the summed pulses of the element pulse, and lateral emission may have a shifted phase.

5.7 CONCLUSIONS

In this study, the single element and beamformed radiation patterns were compared between kerfless and fully kerfed linear arrays. The results showed that kerfless array performance was close to the level of a fully kerfed array if the angle dependant variation in signal gain is compensated for. Although kerfless arrays inherently had slightly lower

performance, the advantages in simplified fabrication may be an acceptable trade-off in many imaging applications.

The study presents two significant findings. The first finding is that kerfless linear arrays can be used for phased array ultrasonic imaging if the angle dependant variation in gain is compensated for (Figure 5-14). The second finding was that kerfless PZT-5H arrays generate a low-frequency wave at wide steering angles that may be exploitable for an expanded field of view. Despite the promising findings, it is worth noting that the kerfless arrays still show compromises when directly compared to fully-kerfed and sub-diced arrays, such as the weakened signal within the $\pm$ 15 to 20° bands and reduced signal bandwidth/resolution (Figure 5-9). Through methods have been proposed that may further help to alleviate the drawbacks associated with kerfless arrays, more work is required to fully realize this opportunity.

CHAPTER 6:

CONCLUSION

Minimally invasive surgical procedures are an exciting area of development within the medical field. The potential to reduce collateral tissue damage means that minimally invasive procedures have shorter recovery times and lower incidence of comorbidities such as infection (Ochsner 2000). However, the restricted access to the pathological tissues results in unique challenges related to visualization and manipulation of the tissue and surgical pathways (Wilhelm et al. 2018). The development of a high-resolution endoscopic ultrasound device presents an exciting opportunity to satisfy aspects of the visualization challenges, thereby aiding in the advancement and adoption of minimally invasive procedures.

6.1 STUDY ONE – FABRICATION OF ENDOSCOPIC FORM-FACTOR

This research began with an investigation into potential techniques for the miniaturization of ultrasonic arrays to achieve an endoscopic form-factor. Considerable efforts went into the development of new microfabrication processes and packaging techniques. In the end, a viable construction technique was established, and an ultrasonic array was developed that fit within a 2.5 mm by 3.1 mm cross-section. The imaging performance was quantified and reached a similar performance level as other high-resolution ultrasonic imaging systems, but with an endoscopic form-factor.

6.1.1 STUDY ONE - LIMITATIONS

Even with the promising initial results, the array presented several challenges that limited performance. Mainly, the use of a 1λ pitch for the array elements resulted in grating lobes that limited the steering angle of the device to $\pm 32°$. Additionally, though the work proved

that an endoscopic ultrasonic array could be produced, there remain significant process steps in packaging and encapsulating the device for clinical applications. At this point in the research, the arrays were using hand-built cable assemblies, and were driven by running custom data-collection scripts on a commercially available system and then processing the data offline. The generation of one image frame took up to an hour to collect and process. Though not covered in this thesis, the development of beamforming hardware to facilitate data collection constituted a significant effort and greatly facilitated later studies.

6.1.2   STUDY ONE SUMMARY

This study started with an investigation into the potential of creating a high-resolution ultrasonic array in an endoscopic form-factor. However, the design required the use of a 64 element design with elements at 1λ pitch instead of a more conventional configuration with 128 elements and a ½λ pitch. These element count trade-offs allowed for packaging refinements that provided an overall package size of 3.1 x 2.5 mm, which was considered to be suitable for a broad range of endoscopic applications. Therefore, the work proved that a high-resolution ultrasonic array could be produced in an endoscopic form-factor. However, the large element pitch in the design lowered the maximum steering angle due to the introduction of grating lobes. Moreover, these arrays required semi-kerfing through micro-dicing for element-to-element isolation. This fabrication step was challenging, with inherently long processing times and low yield.

6.2   STUDY TWO – PASSIVE METHOD FOR GRATING LOBE SUPPRESSION

The objective of the second study was to determine if a Vernier element spacing technique would allow for the passive reduction of grating lobes, present in the original design. The technique works by using a different element pitch between the transmission and reception events of ultrasonic pulses. The different pitch for each event was designed to optimally suppress grating lobes without an increase in the number of electrical interconnections in the array.

6.2.1 STUDY TWO – LIMITATIONS

Although the technique was validated as an effective method for grating lobe suppression and was able to image a wider range of steering angles, the sparsity of the array would severely limit its applicability in general soft tissue applications.

6.2.2 STUDY TWO – SUMMARY

The arrays were simulated, and the simulations were validated through the construction of arrays. The testing of these arrays showed that the grating lobes were suppressed by 33 dB. However, the main lobe was also suppressed by 15 dB, resulting in an effective grating lobe suppression of 18 dB.

Though this result was significant, the limited signal strength of these arrays limits the application of these devices to areas where lower sensitivity is acceptable. One possible application for this technology is the imaging of the middle and inner ear, where the ear can be filled with water and where the cortical bone of the skull presents a highly echogenic signal at the edges of the image (Torbatian et al. 2009; Torbatian 2012). It should be pointed out, however, that due to the acceleration in computational technology such as graphics processing units, software-based adaptive beamforming solutions are likely a better approach to grating lobe suppression over passive array geometry approaches such as that described in this study.

6.3 STUDY THREE –KERFLESS ARRAY DIRECTIVITY INVESTIGATION

During the second study, it was observed that kerfless array designs provided more signal at higher steering angles than was initially expected. The purpose of the third study was to explore this characteristic and to provide a model explaining the better-than-expected performance.

6.3.1 STUDY THREE – LIMITATIONS

A model was developed that focused on including the acoustic emissions originating from laterally propagating waves. The developed simulation techniques became very computationally demanding as each propagation was modeled independently and then summed.

When compared against the standard impulse response simulation of a beamformed pulse, the resulting scripts increased the computational demands by a factor proportional to the number of simulated propagations. A final set of limitations on the third study was the lack of experimental data for different piezoelectric substrates. When the model was developed, it was used to make predictions related to the performance of kerfless PZT-5H and kerfless PMN-PT arrays. Due to time constraints, only the performance of a PZT-5H array was physically tested. Ideally, time would have allowed for continued fabrication and testing as the model predicted superior performance for kerfless PMN-PT arrays.

6.3.2   STUDY THREE – SUMMARY

During the third study, a model was developed that helped explain a recently observed finding whereby kerfless arrays were observed to produce higher signal levels at steering angles beyond $\pm$ 15° than had been predicted by the literature. The model was tested and showed a good fit with experimental results.

6.4   FUTURE WORK

The motivation for this research was focused on developing high-resolution ultrasonic endoscopes to satisfy the needs of minimally invasive surgical procedures.

At a minimum, the arrays would require some developments related to the application and maintenance of sterile packaging before clinical application. However, real-time imaging has been achieved, and research-based collaborations with clinical staff and academic groups may best inform future technical developments.

In addition to these points, several other technological avenues would benefit from exploration; testing with kerfless PMN-PT arrays and exploration of whether the lower frequency acoustic waves (at ½ the transducer's center frequency) that are seen at high steering angles, may be used for an expanded field of view.

An additional area of future work could involve an exploration of the acoustic model within finite element modeling software packages, to obtain more detailed simulations that incorporate more features of the arrays.

6.5 FINAL CONCLUSIONS

The work conducted in this thesis investigated the development of high-resolution ultrasonic endoscopes with the aim of helping to minimize the imaging challenges associated with minimally invasive surgical procedures. In the first study, a design was produced that met the size requirements of endoscopic applications. Though the array entailed some design compromises, it achieved the objective of incorporating a high-resolution ultrasonic array into an endoscopic package. It is hoped that this study will represent a significant contribution to the existing literature by establishing the techniques for, and demonstrating the feasibility of, the production of high-resolution ultrasonic endoscopes.

The second study was able to successfully demonstrate that a Vernier array pattern would significantly suppress grating lobe image artifacts. However, the overall signal in a Vernier array proved to be significantly attenuated, and therefore, it's tissue imaging applications are limited. Some applications, such as imaging the middle and inner ear, are well suited to the resulting performance characteristics of Vernier arrays. However, when all factors are considered, the most promising methods of grating lobe suppression appear to be computationally based. Due to the varying pitch of elements within a Vernier array, kerfless arrays were used in this study. The images collected by these arrays were characterized by dark bands (attenuated zones) around $\pm\,15°$ and a higher signal strength from 20° to 30° than would have been expected considering the poor directivity reported in existing literature.

In the third study, we explored observations related to the performance of kerfless arrays seen during the second study. We expanded on current simulation techniques to include the acoustic emissions of lateral waves, and the resulting predictions showed a strong correlation to experimental results. Though future developments may be required to fully capitalize on the potential of kerfless arrays, this work has significantly expanded on the reported body of measured data related to the performance of kerfless arrays, and has established that the material selection in these arrays is critically important.

The work presented in this thesis has demonstrated viable techniques for the construction of high-resolution ultrasonic endoscopes. Future work may expand on these methods and may take advantage of newly established knowledge, such as the kerfless array directivity.

BIBLIOGRAPHY

Adelsperger, Amelia R, Evan H Phillips, Hilda S Ibriga, Bruce A Craig, Linden A Green, Michael P Murphy, and Craig J Goergen. 2018. "Development and growth trends in angiotensin II-induced murine dissecting abdominal aortic aneurysms." *Physiological reports* 6 (8): e13668.

Aernouts, Jef, Johan R. M. Aerts, and Joris J. J. Dirckx. 2012. "Mechanical properties of human tympanic membrane in the quasi-static regime from in situ point indentation measurements." *Hearing Research* 290 (1-2): 45-54.

Anbarasan, Thineskrishna, Christine EM Démoré, Holly Lay, Mohammed RS Sunoqrot, Romans Poltarjonoks, Sandy Cochran, and Benjamin F Cox. 2017. "High Resolution Microultrasound (μUS) Investigation of the Gastrointestinal (GI) Tract." *Biosensors and Biodetection: Methods and Protocols, Volume 2: Electrochemical, Bioelectronic, Piezoelectric, Cellular and Molecular Biosensors*: 541-561.

ASA. Retrived_2019. "Procedures - Back Surgery." American Society of Anesthesiologists. Accessed Dec 4, 2019. https://www.asahq.org/whensecondscount/preparing-for-surgery/procedures/back-surgery/.

Baber, Zafeer, and Michael Erdek. 2016. "Failed back surgery syndrome: current perspectives." *Journal of Pain Research* Volume 9: 979-987.

Bantignies, Claire, Pascal Mauchamp, Rémi Dufait, Franck Levassort, Tony Mateo, J Grégoire, and Frédéric Ossant. 2011. "40 MHz piezo-composite linear array and integration in a high resolution system." Ultrasonics Symposium (IUS), 2011 IEEE International.

Bates, Andrew T., and Celia Divino. 2015. "Laparoscopic surgery in the elderly: a review of the literature." *Aging and disease* 6 (2): 149-155.

Beekman, R., and L. H. Visser. 2004. "High-resolution sonography of the peripheral nervous system - a review of the literature." *European Journal of Neurology* 11 (5): 305-314.

Bernassau, A. L., L. Garcia-Gancedo, D. Hutson, C. E. Demore, J. J. McAneny, T. W. Button, and S. Cochran. 2012. "Microfabrication of electrode patterns for high-frequency ultrasound transducer arrays." *IEEE Trans Ultrason Ferroelectr Freq Control* 59 (8): 1820-9.

Bernassau, A.L., D. Flynn, F. Amalou, M.P.Y Desmulliez, and S. Cochran. 2009. "Techniques for wirebond free interconnection of piezoelectric ultrasound arrays operating above 50 MHz." *IEEE-UFFC Rome, Italy*.

Bezanson, Andre B, Robert Adamson, and Jeremy A. Brown. 2013. "Fabrication and performance of a miniaturized 64-element high-frequency endoscopic phased array." 2013 IEEE International Ultrasonics Symposium (IUS), 2013-07-21.

---. 2014. "Fabrication and performance of a miniaturized 64-element high-frequency endoscopic phased array." *IEEE Transactions on Ultrasonics, Ferroelectrics, and Frequency Control* 61 (1): 33-43.

---. 2015. Ultrasound endoscope and methods of manufacture thereof. United States US Application filed 2015-07-30.

Bezanson, Andre B., Robert Adamson, and Jeremy A. Brown. 2011. "A low-cost high frame-rate piezoelectric scanning mechanism for high-frequency ultrasound systems." 2011 IEEE International Ultrasonics Symposium, 2011-08-18.

Bezanson, Andre B., Phil Garland, Robert Adamson, and Jeremy A. Brown. 2012. "Fabrication of a miniaturized 64-element high-frequency phased array." 2012 IEEE International Ultrasonics Symposium, 2012-08-07.

Bezanson, Andre B., Jeff Leadbetter, and Jeremy A. Brown. 2014. "Fabrication of a high-frequency phased array with sparse Vernier array element spacing for grating lobe suppression." 2014 IEEE International Ultrasonics Symposium, 2014-08-03.

BK-Ultrasound. 2015. *I12C4f Transducer - User Guide.* 8 Centennial Drive, Peabody, MA 01960, USA: BK Ultrasound.

Bradley, William G. 2008. "History of medical imaging." *Proceedings of the American Philosophical Society* 152 (3): 349-361.

Brayda-Bruno, M., and P. Cinnella. 2000. "Posterior endoscopic discectomy (and other procedures)." *European Spine Journal* 9 (S1): S024-S029.

Brown, Jeremy A., F. S. Foster, A. Needles, E. Cherin, and G. R. Lockwood. 2007. "Fabrication and performance of a 40-MHz linear array based on a 1-3 composite with geometric elevation focusing." *IEEE Trans Ultrason Ferroelectr Freq Control* 54 (9): 1888-94.

Brown, Jeremy A., Jeff Leadbetter, Michael Leung, Andre B. Bezanson, and Robert Adamson. 2013. "A low cost open source high frame-rate high-frequency imaging system." 2013 IEEE International Ultrasonics Symposium (IUS), 2013-07-21.

Brown, Jeremy A., S. Sharma, Jeff Leadbetter, Sandy Cochran, and Robert Adamson. 2014. "Mass-spring matching layers for high-frequency ultrasound transducers: a new technique using vacuum deposition." *IEEE Trans Ultrason Ferroelectr Freq Control* 61 (11): 1911-21.

Brunke, Shelby S, and Geoffrey R Lockwood. 1997. "Broad-bandwidth radiation patterns of sparse two-dimensional vernier arrays." *IEEE transactions on ultrasonics, ferroelectrics, and frequency control* 44 (5): 1101-1109.

Bushberg, Jerrold T, and John M Boone. 2011. *The essential physics of medical imaging*. Lippincott Williams & Wilkins.

Cabrera-Munoz, Nestor E., Payam Eliahoo, Robert Wodnicki, Hayong Jung, Chi Tat Chiu, Jay A. Williams, Hyung Ham Kim, Qifa Zhou, Guang-Zhong Yang, and K. Kirk Shung. 2019. "Fabrication and Characterization of a Miniaturized 15-MHz Side-Looking Phased-Array Transducer Catheter." *IEEE Transactions on Ultrasonics, Ferroelectrics, and Frequency Control* 66 (6): 1079-1092.

Cannata, J. M. , J. A. Williams, Hu Chang-Hong, and K. K. Shung. 2008. Development of high frequency linear arrays using interdigital bonded composites.

Cannata, JM, JA Williams, and KK Shung. 2005. "A kerfless 30 MHz linear ultrasonic array." Ultrasonics Symposium, 2005 IEEE.

Cannata, Jonathan M, Jay A Williams, Lequan Zhang, Chang-Hong Hu, and K Kirk Shung. 2011. "A high-frequency linear ultrasonic array utilizing an interdigitally bonded 2-2 piezo-composite." *IEEE transactions on ultrasonics, ferroelectrics, and frequency control* 58 (10): 2202-2212.

Cannata, Jonathan M, Jay A Williams, Qifa Zhou, Timothy A Ritter, and K Kirk Shung. 2006. "Development of a 35-MHz piezo-composite ultrasound array for medical imaging." *IEEE transactions on ultrasonics, ferroelectrics, and frequency control* 53 (1): 224-236.

Carey, Stephen J, Christian Brox-Nilsen, Hugh M Lewis, Christopher M Gregory, and John V Hatfield. 2009. "Scanning head with 128-element 20-MHz PVDF linear array transducer." *IEEE transactions on ultrasonics, ferroelectrics, and frequency control* 56 (8).

Chen, R., N. E. Cabrera-Munoz, K. H. Lam, H. S. Hsu, F. Zheng, Q. Zhou, and K. K. Shung. 2014. "PMN-PT single-crystal high-frequency kerfless phased array." *IEEE Trans Ultrason Ferroelectr Freq Control* 61 (6): 1033-41.

Chen, Ying-Chun, Lin Zhang, Er-Nan Li, Li-Xiang Ding, Gen-Ai Zhang, Yu Hou, and Wei Yuan. 2019. "An updated meta-analysis of clinical outcomes comparing minimally invasive with open transforaminal lumbar interbody fusion in patients with degenerative lumbar diseases." *Medicine* 98 (43): e17420.

Cheng, Yonghong, and Yiming Liu. 2019. "Percutaneous curved vertebroplasty in the treatment of thoracolumbar osteoporotic vertebral compression fractures." *Journal of International Medical Research* 47 (6): 2424-2433.

Cobbold, Richard SC. 2006. *Foundations of biomedical ultrasound*. Oxford University Press.

Colchester, Richard J., Callum Little, George Dwyer, Sacha Noimark, Erwin J. Alles, Edward Z. Zhang, Christopher D. Loder, Ivan P. Parkin, Ioannis Papakonstantinou, Paul C. Beard, Malcolm C. Finlay, Roby D. Rakhit, and Adrien E. Desjardins. 2019. "All-Optical Rotational Ultrasound Imaging." *Scientific Reports* 9 (1).

Cook, Jason R, Richard R Bouchard, and Stanislav Y Emelianov. 2011. "Tissue-mimicking phantoms for photoacoustic and ultrasonic imaging." *Biomedical optics express* 2 (11): 3193-3206.

Council, National Research. 1996. *Mathematics and physics of emerging biomedical imaging*. National Academies Press.

Cox, Benjamin F., Fraser Stewart, Holly Lay, Gerard Cummins, Ian P. Newton, Marc P. Y. Desmulliez, Robert J. C. Steele, Inke Näthke, and Sandy Cochran. 2017. "Ultrasound capsule endoscopy: sounding out the future." *Annals of translational medicine* 5 (9): 201-201.

Cullen, John P., and Mark A. Talamini. 2010. "General Surgery: Current Trends and Recent Innovations." In *Key Topics in Surgical Research and Methodology*, 781-791.

Cummins, Thomas, Payam Eliahoo, and K. Kirk Shung. 2016. "High-Frequency Ultrasound Array Designed for Ultrasound-Guided Breast Biopsy." *IEEE Transactions on Ultrasonics, Ferroelectrics, and Frequency Control* 63 (6): 817-827.

Dauchy, F., and R. A. Dorey. 2007. "Thickness mode high frequency MEMS piezoelectric micro ultrasound transducers." *Journal of Electroceramics* 19 (4): 383-386.

Dausch, David E, John B Castellucci, Derrick R Chou, and Olaf T von Ramm. 2008. "Theory and operation of 2-D array piezoelectric micromachined ultrasound transducers." *ieee transactions on ultrasonics, ferroelectrics, and frequency control* 55 (11).

Degertekin, F. L., R. O. Guldiken, and M. Karaman. 2006. "Annular-ring CMUT arrays for forward-looking IVUS: transducer characterization and imaging." *IEEE Transactions on Ultrasonics, Ferroelectrics and Frequency Control* 53 (2): 474-482.

Demirci, Utkan, Arif S Ergun, Omer Oralkan, Mustafa Karaman, and Butrus T Khuri-Yakub. 2004. "Forward-viewing CMUT arrays for medical imaging." *IEEE transactions on ultrasonics, ferroelectrics, and frequency control* 51 (7): 887-895.

Desilets, Charles S, John D Fraser, and Gordon S Kino. 1978. "The design of efficient broad-band piezoelectric transducers." *IEEE Transactions on sonics and ultrasonics* 25 (3): 115-125.

Di Ieva, Antonio, Fabio Rotondo, Luis V Syro, Michael D Cusimano, and Kalman Kovacs. 2014. "Aggressive pituitary adenomas diagnosis and emerging treatments." *Nature Reviews Endocrinology* 10 (7): 423.

Faerber, Julia, Rachael Gregson, Richard Eddie Clutton, Sadeque Reza Khan, Sandy Cochran, Marc P. Y. Desmulliez, Gerard Cummins, Sumanth Kumar Pavuluri, Paul Record, Adrian R. Ayastuy Rodriguez, Holly S. Lay, Rachael McPhillips, Benjamin F. Cox, and Ciaran Connor. 2018. "In Vivo Characterization of a Wireless Telemetry Module for a Capsule Endoscopy System Utilizing a Conformal Antenna." *IEEE Transactions on Biomedical Circuits and Systems* 12 (1): 95-105.

Fei, C., J. Ma, C. T. Chiu, J. A. Williams, W. Fong, Z. Chen, B. Zhu, R. Xiong, J. Shi, T. K. Hsiai, K. K. Shung, and Q. Zhou. 2015. "Design of matching layers for high-frequency ultrasonic transducers." *Appl Phys Lett* 107 (12): 123505.

Fleshman, James W, Heidi Nelson, Walter R Peters, H Charles Kim, Sergio Larach, Richard R Boorse, Wayne Ambroze, Phillip Leggett, Ronald Bleday, and Steven Stryker. 1996. "Early results of laparoscopic surgery for colorectal cancer." *Diseases of the Colon & Rectum* 39 (10): S53-S58.

Forte, Antonio Jorge, Daniel Boczar, Jeremie D. Oliver, Andrea Sisti, and Steven R. Clendenen. 2019. "Ultra-high-frequency Ultrasound to Assess Nerve Fascicles in Median Nerve Traumatic Neuroma." *Cureus*.

Foster, F Stuart, James Mehi, Marc Lukacs, Desmond Hirson, Chris White, Chris Chaggares, and Andrew Needles. 2009. "A new 15–50 MHz array-based micro-ultrasound scanner for preclinical imaging." *Ultrasound in Medicine and Biology* 35 (10): 1700-1708.

Foster, F Stuart, Charles J Pavlin, Kasia A Harasiewicz, Donald A Christopher, and Daniel H Turnbull. 2000. "Advances in ultrasound biomicroscopy." *Ultrasound in medicine & biology* 26 (1): 1-27.

Franco, Ediguer E, Marco AB Andrade, Julio C Adamowski, and Flávio Buiochi. 2011. "Acoustic beam modeling of ultrasonic transducers and arrays using the impulse response and the discrete representation methods." *Journal of the Brazilian Society of Mechanical Sciences and Engineering* 33 (4): 408-416.

Friedly, Janna, Christopher Standaert, and Leighton Chan. 2010. "Epidemiology of spine care: the back pain dilemma." *Physical Medicine and Rehabilitation Clinics* 21 (4): 659-677.

Fudulu, Daniel, Harriet Lewis, Umberto Benedetto, Massimo Caputo, Gianni Angelini, and Hunaid A Vohra. 2017. "Minimally invasive aortic valve replacement in high risk patient groups." *Journal of thoracic disease* 9 (6): 1672.

Fujifilm. 2016. *Endoscopic Ultrasound System.* Düsseldorf, Germany: FUJIFILM Europe GmbH.

Fujimoto, James, and Eric Swanson. 2016. "The development, commercialization, and impact of optical coherence tomography." *Investigative ophthalmology & visual science* 57 (9): OCT1-OCT13.

Fuster, Valentin. 2017. "Changing Demographics: A New Approach to Global Health Care Due to the Aging Population." *Journal of the American College of Cardiology* 69 (24): 3002-3005.

Garland, Phil P., Andre B. Bezanson, Robert Adamson, and Jeremy A. Brown. 2011. "Experimental and finite element model directivity comparison between PZT and PMN-PT kerfless arrays." 2011 IEEE International Ultrasonics Symposium, 2011-10-18.

Goertz, David E, L Yu Joanne, Robert S Kerbel, Peter N Burns, and F Stuart Foster. 2002. "High-frequency Doppler ultrasound monitors the effects of antivascular therapy on tumor blood flow." *Cancer research* 62 (22): 6371-6375.

Gora, Michalina J, Jenny S Sauk, Robert W Carruth, Kevin A Gallagher, Melissa J Suter, Norman S Nishioka, Lauren E Kava, Mireille Rosenberg, Brett E Bouma, and Guillermo J Tearney. 2013. "Tethered capsule endomicroscopy enables less invasive imaging of gastrointestinal tract microstructure." *Nature medicine* 19 (2): 238.

Grune, Jana, Annelie Blumrich, Sarah Brix, Sarah Jeuthe, Cathleen Drescher, Tilman Grune, Anna Foryst-Ludwig, Daniel Messroghli, Wolfgang M Kuebler, and Christiane Ott. 2018. "Evaluation of a commercial multi-dimensional echocardiography technique for ventricular volumetry in small animals." *Cardiovascular ultrasound* 16 (1): 10.

Hacihaliloglu, I. 2017. "Ultrasound imaging and segmentation of bone surfaces: A review." *Technology (Singap World Sci)* 5 (2): 74-80.

Hammoud, Maarouf A, B Lee Ligon, Rabih Elsouki, Wei Ming Shi, Donald F Schomer, and Raymond Sawaya. 1996. "Use of intraoperative ultrasound for localizing tumors and determining the extent of resection: a comparative study with magnetic resonance imaging." *Journal of neurosurgery* 84 (5): 737-741.

Hitachi. 2012. ProSound Alpha 7 Version 6.1.0. http://www.roxon.ca/uploads/document/5660bc02c0828.pdf. Hitachi Aloka Medical LTD, Ltd. Hitachi Aloka Medical, 10 Fairfield Boulevard, Wallingford, CT 06492.

Hu, ChangHong, Lequan Zhang, Jonathan M Cannata, and K Kirk Shung. 2010. "Development of a digital high frequency ultrasound array imaging system." Ultrasonics Symposium (IUS), 2010 IEEE.

Huygens, Christiaan. 1690. "1690: Traité de la Lumière (Treatise on Light)." *The Scientific Background to Modern Philosophy*: 124-32.

Inagaki, Ken, Shimpei Arai, Kengo Namekawa, and Iwaki Akiyama. 2018. "Sound Velocity Estimation and Beamform Correction by Simultaneous Multimodality Imaging with Ultrasound and Magnetic Resonance." *Applied Sciences* 8 (11): 2133.

Ivan, Ioan Alexandru, Joël Agnus, and Pierre Lambert. 2012. "PMN–PT (lead magnesium niobate–lead titanate) piezoelectric material micromachining by excimer laser ablation and dry etching (DRIE)." *Sensors and Actuators A: Physical* 177: 37-47.

Janjic, Jovana, Mingliang Tan, Verya Daeichin, Emile Noothout, Chao Chen, Zhao Chen, Zu-Yao Chang, Robert H. S. H. Beurskens, Gijs Van Soest, Antonius F. W. Van Der Steen, Martin D. Verweij, Michiel A. P. Pertijs, and Nico De Jong. 2018. "A 2-D Ultrasound Transducer With Front-End ASIC and Low Cable Count for 3-D Forward-Looking Intravascular Imaging: Performance and Characterization." *IEEE Transactions on Ultrasonics, Ferroelectrics, and Frequency Control* 65 (10): 1832-1844.

Jensen, Henrik, Robert Harold Owen, Soren Juel Andersen, Christopher Beers, Niels Christian Sasady, and Per Ehrenreich Nygaard. 2018. Ultrasound imaging system probe cable and connector. Google Patents.

Jensen, Jo/rgen Arendt. 1999. "A new calculation procedure for spatial impulse responses in ultrasound." *The Journal of the Acoustical Society of America* 105 (6): 3266-3274.

Jin, XC, BT Ehuri-Yakub, FL Degertekin, I Ladabaum, and S Calmes. 1998. "Micromachined capacitive ultrasonic immersion transducer for medical imaging." Engineering in Medicine and Biology Society, 1998. Proceedings of the 20th Annual International Conference of the IEEE.

John-Hopkins, Health. 2019. "Minimally Invasive Spinal Fusion." Accessed Dec 4, 2019. https://www.hopkinsmedicine.org/health/treatment-tests-and-therapies/minimally-invasive-spinal-fusion.

Jones, Rhys, Patrick Haufe, Edward Sells, Pejman Iravani, Vik Olliver, Chris Palmer, and Adrian Bowyer. 2011. "RepRap–the replicating rapid prototyper." *Robotica* 29 (1): 177-191.

Juliano, Amy F, Daniel T Ginat, and Gul Moonis. 2013. "Imaging review of the temporal bone: part I. Anatomy and inflammatory and neoplastic processes." *Radiology* 269 (1): 17-33.

Ketterling, Jeffrey A, Orlando Aristizábal, Billy YS Yiu, Daniel H Turnbull, Colin KL Phoon, CH Alfred, and Ronald H Silverman. 2017. "High-speed, high-frequency ultrasound, in utero vector-flow imaging of mouse embryos." *Scientific reports* 7 (1): 16658.

Kim, Jihun, TJ Shin, HJ Kong, Jae Youn Hwang, and HK Hyun. 2019. "High-frequency ultrasound imaging for examination of early dental caries." *Journal of dental research* 98 (3): 363-367.

Kim, Moojoon, Jungsoon Kim, and Wenwu Cao. 2006. "Electromechanical coupling coefficient of an ultrasonic array element." *Journal of applied physics* 99 (7): 074102.

Krimholtz, R. , D. A. Leedom, and G. L. Matthaei. 1970. "New equivalent circuits for elementary piezoelectric transducers." *Electronics Letters* 6 (13): 398-399.

Landry, Thomas G, Guy Earle, Jeremy A Brown, and Manohar L Bance. 2018. "Real-time intracochlear imaging of automated cochlear implant insertions in whole decalcified cadaver cochleas using ultrasound." *Cochlear implants international* 19 (5): 255-267.

Latham, Gregory J, Melissa L Veneracion, Denise C Joffe, Adrian T Bosenberg, Sean H Flack, and Daniel K Low. 2013. "High-frequency micro-ultrasound for vascular access in young children–a feasibility study by the High-frequency UltraSound in Kids studY (HUSKY) group." *Pediatric Anesthesia* 23 (6): 529-535.

Lawrence, Melinda M, and Salim M Hayek. 2013. "Minimally invasive lumbar decompression: a treatment for lumbar spinal stenosis." *Current Opinion in Anesthesiology* 26 (5): 573-579.

Lay, Holly S., Benjamin F. Cox, Vipin Seetohul, Christine E. M. Demore, and Sandy Cochran. 2018. "Design and Simulation of a Ring-Shaped Linear Array for Microultrasound Capsule Endoscopy." *IEEE Transactions on Ultrasonics, Ferroelectrics, and Frequency Control* 65 (4): 589-599.

Leal Ghezzi, Tiago, and Oly Campos Corleta. 2016. "30 Years of Robotic Surgery." *World journal of surgery* 40 (10): 2550-2557.

Lee, John H, Giovanni Traverso, Carl M Schoellhammer, Daniel Blankschtein, Robert Langer, Kai E Thomenius, Duane S Boning, and Brian W Anthony. 2014. "Towards wireless capsule endoscopic ultrasound (WCEU)." 2014 IEEE International Ultrasonics Symposium.

Lew, J. I., and C. C. Solorzano. 2010. "Use of Ultrasound in the Management of Thyroid Cancer." *The Oncologist* 15 (3): 253-258.

Li, L., S. Mori, M. Kodama, M. Sakamoto, S. Takahashi, and T. Kodama. 2013. "Enhanced Sonographic Imaging to Diagnose Lymph Node Metastasis: Importance of Blood Vessel Volume and Density." *Cancer Research* 73 (7): 2082-2092.

Liu, C., Q. Zhou, F. T. Djuth, and K. K. Shung. 2012. "High-frequency (>50 MHz) medical ultrasound linear arrays fabricated from micromachined bulk PZT materials." *IEEE Trans Ultrason Ferroelectr Freq Control* 59 (2): 315-8.

Lockwood, Geoffrey R, and F Stuart Foster. 1994. "Modeling and optimization of high-frequency ultrasound transducers." *IEEE transactions on ultrasonics, ferroelectrics, and frequency control* 41 (2): 225-230.

Lockwood, Geoffrey R, Pai-Chi Li, Matthew O'Donnell, and F Stuart Foster. 1996. "Optimizing the radiation pattern of sparse periodic linear arrays." *IEEE Transactions on Ultrasonics, Ferroelectrics, and frequency control* 43 (1): 7-14.

Lu, X Ming, and TL Proulx. 2005. "Single crystals vs. PZT ceramics for medical ultrasound applications." Ultrasonics Symposium, 2005 IEEE.

Lucas, V. S., R. S. Burk, S. Creehan, and M. J. Grap. 2014. "Utility of high-frequency ultrasound: moving beyond the surface to detect changes in skin integrity." *Plast Surg Nurs* 34 (1): 34-8.

Lukacs, M., M. Sayer, and S. Foster. 2000. "Single element high frequency (<50 MHz) PZT sol gel composite ultrasound transducers." 47 (1): 148-159.

Lukacs, Marc, Jianhua Yin, Guofeng Pang, Richard Garcia, Emmanuel Cherin, Ross Williams, Jim Mehi, and F. Foster. 2006. "Performance and Characterization of New Micromachined High-Frequency Linear Arrays." *IEEE Transactions on Ultrasonics, Ferroelectrics and Frequency Control* 53 (10): 1719-1729.

Ma, Teng, Bill Zhou, Tzung K Hsiai, and K Kirk Shung. 2016. "A review of intravascular ultrasound-based multimodal intravascular imaging: the synergistic approach to characterizing vulnerable plaques." *Ultrasonic imaging* 38 (5): 314-331.

MacDougall, Dan, Joshua Farrell, Jeremy A. Brown, Manohar Bance, and Robert Adamson. 2016. "Long-range, wide-field swept-source optical coherence tomography with GPU accelerated digital lock-in Doppler vibrography for real-time, in vivo middle ear diagnostics." *Biomedical optics express* 7 (11): 4621-4635.

Maréchal, Pierre, Franck Levassort, L-P Tran-Huu-Hue, Marc Lethiecq, and Nicolas Félix. 2004. "Effect of acoustical properties of a lens on the pulse-echo response of a single element transducer." Ultrasonics Symposium, 2004 IEEE.

McAnany, Steven J, Jun S Kim, Samuel C Overley, Evan O Baird, Paul A Anderson, and Sheeraz A Qureshi. 2015. "A meta-analysis of cervical foraminotomy: open versus minimally-invasive techniques." *The Spine Journal* 15 (5): 849-856.

McPhillips, Rachael. 2017. "Fabrication of Ultrasound Transducers and Arrays Integrated Within Needles for Imaging Guidance and Diagnosis." University of Dundee.

Medtronic. 2016. *Product Catalog.* Goleta, CA: Inc. Medtronic.

Mekky, Mohamed A. 2014. "Endoscopic ultrasound in gastroenterology: From diagnosis to therapeutic implications." *World Journal of Gastroenterology* 20 (24): 7801.

Mezger, Uli, Claudia Jendrewski, and Michael Bartels. 2013. "Navigation in surgery." *Langenbeck's Archives of Surgery* 398 (4): 501-514.

Midtbø, K, A Rønnekleiv, KA Ingebrigtsen, J Due-Hansen, E Poppe, DT Wang, GU Jensen, and K Schjølberg-Henriksen. 2012. "High-frequency CMUT arrays with phase-steering for in vivo ultrasound imaging." Sensors, 2012 IEEE.

Mlosek, Robert, and Sylwia Malinowska. 2014. "Application of high-frequency ultrasonography in closing small blood vessels." *Journal of Ultrasonography* 14 (58): 320-327.

Mohler, Emile R., Alexandra A. Sibley, Susan M. Schultz, Lifeng Zhang, and Chandra M. Sehgal. 2009. "High-Frequency Ultrasound for Evaluation of Intimal Thickness." *Journal of the American Society of Echocardiography* 22 (10): 1129-1133.

Morton, CE, and GR Lockwood. 2002. "Evaluation of kerfless linear arrays." Ultrasonics Symposium, 2002. Proceedings. 2002 IEEE.

Mu, Ju-Wei, Shu-Geng Gao, Qi Xue, You-Sheng Mao, Da-Li Wang, Jun Zhao, Yu-Shun Gao, Jin-Feng Huang, and Jie He. 2015. "Updated experiences with minimally invasive McKeown esophagectomy for esophageal cancer." *World journal of gastroenterology* 21 (45): 12873.

Netter, Frank H. 2014. *Atlas of Human Anatomy, Saunders Elsevier, 2014: Atlas of Human Anatomy*. Vol. 1. Bukupedia.

Ochsner, John L. 2000. "Minimally Invasive Surgical Procedures." *The Ochsner Journal* 2 (3): 135-136.

Olympus. 2014. *Forward-Viewing Ultrasound Gastrovideoscope Creates Pioneering New Opportunities in EUS-guided Treatment.* Vol. TGF-UC180J. Olympus Europa SE & CO.KG.

Packer, Douglas L, Carolyn L Stevens, Michael G Curley, Charles J Bruce, Fletcher A Miller, Bijoy K Khandheria, Jae K Oh, Lawrence J Sinak, and James B Seward. 2002. "Intracardiac phased-array imaging: methods and initial clinical experience with high resolution, under blood visualization: initial experience with intracardiac phased-array ultrasound." *Journal of the American College of Cardiology* 39 (3): 509-516.

Pang, G., M. Sayer, G. R. Lockwood, and M. Watt. 2006. "Fabrication of PZT sol gel composite ultrasonic transducers using batch fabrication micromolding." *IEEE Trans Ultrason Ferroelectr Freq Control* 53 (9): 1679-84.

Parisi, Amilcare, Daniel Reim, Felice Borghi, Ninh T Nguyen, Feng Qi, Andrea Coratti, Fabio Cianchi, Maurizio Cesari, Francesca Bazzocchi, and Orhan Alimoglu. 2017. "Minimally invasive surgery for gastric cancer: A comparison between robotic, laparoscopic and open surgery." *World journal of gastroenterology* 23 (13): 2376.

Park, Yung, Sang-Ok Seok, Soo-Bin Lee, and Joong-Won Ha. 2018. "Minimally invasive lumbar spinal fusion is more effective than open fusion: a meta-analysis." *Yonsei medical journal* 59 (4): 524-538.

Pavel, D., V. Callaghan, and A. K. Dey. 2010. "Democratization of healthcare through self-monitoring technologies." 2010 4th International Conference on Pervasive Computing Technologies for Healthcare, 22-25 March 2010.

Pederson, T, T Zawada, K Hansen, R Lou-Moeller, and EV Thomsen. 2010. "Fabrication of high frequency PMUT arrays on silicon substrate." *IEEE Trans. Ultrason. Ferroelectr. Freq. Control* 57 (6): 1470-1477.

Phan, Kevin, and Ralph J Mobbs. 2016. "Minimally invasive versus open laminectomy for lumbar stenosis: a systematic review and meta-analysis." *Spine* 41 (2): E91-E100.

Phillips. 2017. *A full line of peripheral IVUS catheters to help guide your treatment strategies.* San Diego, USA: Phillips Volcano.

Pierorazio, Phillip M, and Mohamad E Allaf. 2009. "Minimally invasive surgical training: challenges and solutions." Urologic Oncology: Seminars and Original Investigations.

Qian, Y., and N. R. Harris. 2014. "Modelling of a novel high-impedance matching layer for high frequency (>30MHz) ultrasonic transducers." *Ultrasonics* 54 (2): 586-591.

Rahmani, George, Peter McCarthy, and Diane Bergin. 2017. "The diagnostic accuracy of ultrasonography for soft tissue lipomas: a systematic review." *Acta Radiologica Open* 6 (6): 205846011771670.

Ramasawmy, Rajiv, S Peter Johnson, Thomas A Roberts, Daniel J Stuckey, Anna L David, R Barbara Pedley, Mark F Lythgoe, Bernard Siow, and Simon Walker-Samuel. 2016. "Monitoring the growth of an orthotopic tumour xenograft model: multi-modal imaging assessment with benchtop MRI (1T), high-field MRI (9.4 T), ultrasound and bioluminescence." *PloS one* 11 (5): e0156162.

Ritter, Timothy A, Thomas R Shrout, Rick Tutwiler, and K Kirk Shung. 2002. "A 30-MHz piezo-composite ultrasound array for medical imaging applications." *IEEE transactions on ultrasonics, ferroelectrics, and frequency control* 49 (2): 217-230.

Robinson, D., S. Lees, and L. Bess. 1974. "Near field transient radiation patterns for circular pistons." 22 (6): 395-403.

Rosen, David B, Mandi D Conway, Charles P Ingram, Robin D Ross, and Leonardo G Montilla. 2019. "A Brief Overview of Ophthalmic Ultrasound Imaging." In *Novel Diagnostic Methods in Ophthalmology*. IntechOpen.

Rousset, J, M Garetier, JC Gentric, S Chinellato, C Barberot, T Le Bivic, and P Mériot. 2014. "Biometry of the normal stapes using stapes axial plane, high-resolution computed tomography." *The Journal of Laryngology & Otology* 128 (5): 425-430.

Ruetten, Sebastian, Martin Komp, Harry Merk, and Georgios Godolias. 2008. "Full-endoscopic cervical posterior foraminotomy for the operation of lateral disc herniations using 5.9-mm endoscopes: a prospective, randomized, controlled study." *Spine* 33 (9): 940-948.

Ryan, Linda K, and F Stuart Foster. 1997. "Tissue equivalent vessel phantoms for intravascular ultrasound." *Ultrasound in medicine & biology* 23 (2): 261-273.

Samson, Chris A., Andre B. Bezanson, and Jeremy A. Brown. 2017. "A Sub-Nyquist, Variable Sampling, High-Frequency Phased Array Beamformer." *IEEE Transactions on Ultrasonics, Ferroelectrics, and Frequency Control* 64 (3): 568-576.

SanEmeterio, Jose L., and Luis G. Ullate. 1992. "Diffraction impulse response of rectangular transducers." *The Journal of the Acoustical Society of America* 92 (2): 651-662.

Scatliff, James H, and Peter J Morris. 2014. "From Röntgen to Magnetic Resonance Imaging The History of Medical Imaging." *North Carolina medical journal* 75 (2): 111-113.

Schembre, Drew, Kamran Ayub, and Geoffrey Jiranek. 2005. High-frequency mini-probe ultrasound: the Rodney Dangerfield of endoscopy? : LWW.

Schiavone, Giuseppe, Thomas Jones, Dennis Price, Rachael McPhillips, Yun Jiang, Zhen Qiu, Carl Meggs, Syed O. Mahboob, Sam Eljamel, Tim W. Button, Christine E. M. Demore, Sandy Cochran, and Marc P. Y. Desmulliez. 2017. "A highly compact packaging concept for ultrasound transducer arrays embedded in neurosurgical needles." *Microsystem Technologies* 23 (9): 3881-3891.

Scientific, Boston. 2015. *Captivator™ EMR Device.* Marlborough, USA: Boston Scientific Corporation.

Shearwood, McClelland III, and Jeffrey A Goldstein. 2017. "Minimally invasive versus open spine surgery: What does the best evidence tell us?" *Journal of neurosciences in rural practice* 8 (2): 194.

Shung, K Kirk. 2015. *Diagnostic ultrasound: Imaging and blood flow measurements*. CRC press.

Shung, K. K., J. M. Cannata, and Q. F. Zhou. 2007. "Piezoelectric materials for high frequency medical imaging applications: A review." *Journal of Electroceramics* 19 (1): 141-147.

Silvestry, Frank E, and Susan E Wiegers. 2005. *Intracardiac echocardiography*. CRC Press.

Skovrlj, Branko, Jeffrey Gilligan, Holt S Cutler, and Sheeraz A Qureshi. 2015. "Minimally invasive procedures on the lumbar spine." *World Journal of Clinical Cases: WJCC* 3 (1): 1.

Sosna, Jacob, Mara M. Barth, Jonathan B. Kruskal, and Robert A. Kane. 2005. "Intraoperative Sonography for Neurosurgery." *Journal of Ultrasound in Medicine* 24 (12): 1671-1682.

St.Jude-Medical. 2015. *OPTIS Integrated System.* Abbott. http://www.incathlab.com/files/STJUDE/OPTIS-Integrated-System-brochure.pdf.

Stephens, Douglas N, Matthew O'Donnell, Kai Thomenius, Aaron Dentinger, Douglas Wildes, Peter Chen, K Kirk Shung, Jonathan Cannata, Pierre Khuri-Yakub, and Omer Oralkan. 2009. "Experimental Studies With a 9F Forward-Looking Intracardiac Imaging and Ablation Catheter." *Journal of Ultrasound in Medicine* 28 (2): 207-215.

Storz, Dr. Karl 2017. *TIPCAM®1 S 3D ORL.* Postbox 230, 78503 Tuttlingen/Germany: Karl Storz SE and Co. KG.

---. 2018. *Neurosurgery Highlights 2018.* Postbox 230, 78503 Tuttlingen/Germany: KARL STORZ SE & Co. KG.

Sun, L., W. D. Richard, J. M. Cannata, C. C. Feng, J. A. Johnson, J. T. Yen, and K. K. Shung. 2007. "A high-frame rate high-frequency ultrasonic system for cardiac imaging in mice." *IEEE Trans Ultrason Ferroelectr Freq Control* 54 (8): 1648-55.

Szabo, Thomas L. 2004. *Diagnostic ultrasound imaging: inside out.* Academic Press.

Szabo, Thomas L, and Peter A Lewin. 2013. "Ultrasound transducer selection in clinical imaging practice." *Journal of Ultrasound in Medicine* 32 (4): 573-582.

Tait, IS, SM Yong, and Sir A Cuschieri. 2002. "Laparoscopic in situ ablation of liver cancer with cryotherapy and radiofrequency ablation." *BJS* 89 (12): 1613-1619.

Thoen, P. J. 1982. "Systematic analysis of the grating lobe of ultrasonographic array directivity." PROCEEDINGS OF THE SOCIETY OF PHOTO-OPTICAL INSTRUMENTATION ENGINEERS.

Toda, Minoru, and Mitchell Thompson. 2010. "Polymer-metal front matching layers for ultrasonic transducers with arbitary impedance conversion." Ultrasonics Symposium (IUS), 2010 IEEE.

Torbatian, Z, Robert Adamson, Manohar Bance, and Jeremy A. Brown. 2011. "Experimental verification of a split-aperture transmit beamforming technique for suppressing grating lobes in large pitch phased arrays." Ultrasonics Symposium (IUS), 2011 IEEE International.

Torbatian, Z, Robert Adamson, and Jeremy A. Brown. 2012. "A virtual point source pulse probing technique for suppressing grating lobes in large-pitch phased arrays." Ultrasonics Symposium (IUS), 2012 IEEE International.

Torbatian, Z., R. Adamson, and J. A. Brown. 2013. "Experimental verification of pulse-probing technique for improving phase coherence grating lobe suppression." *IEEE Transactions on Ultrasonics, Ferroelectrics, and Frequency Control* 60 (7): 1324-1332.

Torbatian, Z., Robert Adamson, Manohar Bance, and Jeremy A. Brown. 2010. "A split-aperture transmit beamforming technique with phase coherence grating lobe suppression." *IEEE Trans Ultrason Ferroelectr Freq Control* 57 (11): 2588-95.

Torbatian, Zahra. 2012. "High-Frequency Ultrasound Imaging of the Auditory System."

Torbatian, Zahra, Rob Adamson, Rene van Wijhe, Ronald Pennings, Manohar Bance, and Jeremy A. Brown. 2009. "Imaging the auditory system: A new application of high-frequency ultrasound." Ultrasonics Symposium (IUS), 2009 IEEE International.

UN. 2010. *World population prospects: The 2010 revision*. United Nations. Department of Economic and Social Affairs. Population Division.

Urs, R., J. A. Ketterling, and R. H. Silverman. 2016. "Ultrafast Ultrasound Imaging of Ocular Anatomy and Blood Flow." *Invest Ophthalmol Vis Sci* 57 (8): 3810-6.

Vallor, Shannon. 2011. "Carebots and caregivers: Sustaining the ethical ideal of care in the twenty-first century." *Philosophy & Technology* 24 (3): 251.

Van Mulder, T. J. S., M. de Koeijer, H. Theeten, D. Willems, P. Van Damme, M. Demolder, G. De Meyer, K. C. L. Beyers, and V. Vankerckhoven. 2017. "High frequency ultrasound to assess skin thickness in healthy adults." *Vaccine* 35 (14): 1810-1815.

Van Rossum, Guido, and Fred L Drake. 2011. *The python language reference manual*. Network Theory Ltd.

Vince, D. Geoffrey, and Stephen C. Davies. 2004. "Peripheral application of intravascular ultrasound virtual histology." *Seminars in Vascular Surgery* 17 (2): 119-125.

Viren, T., J. T. Honkanen, E. K. Danso, L. Rieppo, R. K. Korhonen, and J. Toyras. 2017. "Ultrasound Assessment of Human Meniscus." *Ultrasound Med Biol* 43 (9): 1753-1763.

Viviano, Stephen L., Laurel K. Chandler, and Jonathan D. Keith. 2018. "Ultrahigh Frequency Ultrasound Imaging of the Hand: A New Diagnostic Tool for Hand Surgery." *HAND* 13 (6): 720-725.

Vogt, M, J Opretzka, C Perrey, and H Ermert. 2010. "Ultrasonic microscanning." *Proceedings of the Institution of Mechanical Engineers, Part H: Journal of Engineering in Medicine* 224 (2): 225-240.

Von Ramm, OT, SW Smith, and FL Thurstone. 1976. "Gray scale imaging with complex TGC and transducer arrays." Application of Optical Instrumentation in Medicine IV.

Wackym, Phillip A, Wesley A King, Dennis S Poe, Glenn A Meyer, Robert G Ojemann, Fred G Barker, Patrick R Walsh, and Heinrich Staecker. 1999. "Adjunctive use of endoscopy during acoustic neuroma surgery." *The laryngoscope* 109 (8): 1193-1201.

Wagner, Ralf, Albert E Telfeian, Menno Iprenburg, and Guntram Krzok. 2017. "Minimally invasive fully endoscopic two-level posterior cervical foraminotomy." *Journal of Spine Surgery* 3 (2): 238.

Wang, Haifeng, Tim Ritter, Wenwu Cao, and K Kirk Shung. 2001. "High frequency properties of passive materials for ultrasonic transducers." *IEEE transactions on ultrasonics, ferroelectrics, and frequency control* 48 (1): 78-84.

Wang, Louis W., Scott H. Kesteven, Inken G. Huttner, Michael P. Feneley, and Diane Fatkin. 2018. "High-Frequency Echocardiography ─ Transformative Clinical and Research Applications in Humans, Mice, and Zebrafish ─." *Circulation Journal* 82 (3): 620-628.

Wang, Yao, Douglas N Stephens, and Matthew O'Donnell. 2001. "A forward-viewing ring-annular array for intravascular ultrasound imaging." Ultrasonics Symposium, 2001 IEEE.

Wang, Zhihong, Weiguang Zhu, Hong Zhu, Jianmin Miao, Chen Chao, Changlei Zhao, and Ooi Kiang Tan. 2005. "Fabrication and characterization of piezoelectric micromachined ultrasonic transducers with thick composite PZT films." *IEEE transactions on ultrasonics, ferroelectrics, and frequency control* 52 (12): 2289-2297.

Wildes, Douglas, Warren Lee, Bruno Haider, Scott Cogan, Krishnakumar Sundaresan, David M Mills, Christopher Yetter, Patrick H Hart, Christopher R Haun, and Mikael Concepcion. 2016. "4-D ICE: A 2-D array transducer with integrated ASIC in a 10-Fr catheter for real-time 3-D intracardiac echocardiography." *IEEE transactions on ultrasonics, ferroelectrics, and frequency control* 63 (12): 2159-2173.

Wilhelm, Dirk, Thomas Vogel, Daniel Ostler, Nils Marahrens, Nils Kohn, Sebastian Koller, Helmut Friess, and Michael Kranzfelder. 2018. "Enhanced Visualization: From Intraoperative Tissue Differentiation to Augmented Reality." *Visceral medicine* 34 (1): 52-59.

Wu, D-W, Qifa Zhou, Xuecang Geng, C-Geng Liu, Frank Djuth, and K Kirk Shung. 2009. "Very high frequency (beyond 100 MHz) PZT kerfless linear arrays." *IEEE transactions on ultrasonics, ferroelectrics, and frequency control* 56 (10).

Wygant, Ira O, David T Yeh, Xuefeng Zhuang, Srikant Vaithilingam, Amin Nikoozadeh, Omer Oralkan, A Sanli Ergun, Goksen G Yaralioglu, and Butrus T Khuri-Yakub. 2005. "Integrated ultrasound imaging systems based on capacitive micromachined ultrasonic transducer arrays." Sensors, 2005 IEEE.

Xiao, Yiming, Mathieu Boily, Hoda Sadat Hashemi, and Hassan Rivaz. 2018. "High-Dynamic-Range Ultrasound: Application for Imaging Tendon Pathology." *Ultrasound in Medicine & Biology* 44 (7): 1525-1532.

Yang, Hao-Chung, Jonathan Cannata, Jay Williams, and K Kirk Shung. 2012. "Crosstalk reduction for high-frequency linear-array ultrasound transducers using 1-3 piezocomposites with pseudo-random pillars." *IEEE transactions on ultrasonics, ferroelectrics, and frequency control* 59 (10).

Yeh, David T, Omer Oralkan, Arif S Ergun, Xuefeng Zhuang, Ira O Wygant, and Butrus T Khuri-Yakub. 2005. "High-frequency CMUT arrays for high-resolution medical imaging." Medical Imaging 2005: Ultrasonic Imaging and Signal Processing.

Yeh, David T, Omer Oralkan, Ira O Wygant, A Sanli Ergun, J Wong, and Butrus T Khuri-Yakub. 2005. "High-resolution imaging with high-frequency 1-D linear CMUT arrays." IEEE International Ultrasonics Symposium, Rotterdam, The Netherlands.

Yeh, David T, Omer Oralkan, Ira O Wygant, Matthew O'Donnell, and Butrus T Khuri-Yakub. 2006. "3-D ultrasound imaging using a forward-looking CMUT ring array for intravascular/intracardiac applications." *IEEE transactions on ultrasonics, ferroelectrics, and frequency control* 53 (6): 1202-1211.

Yin, He-Ping, Yu-Peng Wang, Zhi-Ye Qiu, Zhi-Cai Du, Yi-Min Wu, and Shu-Wen Li. 2016. "Comparison of safety and efficiency of microendoscopic discectomy with automatic nerve retractor and with nerve hook." *Regenerative Biomaterials* 3 (5): 319-322.

Zanchetta, Mario, Gianluca Rigatelli, Luigi Pedon, Marco Zennaro, Eustaquio Onorato, and Pietro Maiolino. 2002. "Intracardiac Echocardiography During Catheter-Based Procedures: Ultrasound System, Examination Technique, and Image Presentation." *Echocardiography* 19 (6): 501-507.

Zemp, Roger J, Rachel Bitton, K Kirk Shung, Meng-Lin Li, George Stoica, and Lihong V Wang. 2007. "Photoacoustic imaging of the microvasculature with a high-frequency ultrasound array transducer." *Journal of biomedical optics* 12 (1): 010501.

Zhang, Bei-Bei, Yu-Jie Zhou, Jie Du, Shi-Wei Yang, Zhi-Jiang Wang, Hua Shen, and Zhi-Ming Zhou. 2017. "Comparison of very-high-frequency ultrasound assessment of radial arterial wall layers after first and repeated transradial coronary procedures." *Journal of geriatric cardiology: JGC* 14 (4): 245.

Zhang, Junshan, Wei Ren, Xinpan Jing, Peng Shi, and Xiaoqing Wu. 2015. "Deep reactive ion etching of PZT ceramics and PMN-PT single crystals for high frequency ultrasound transducers." 41: S656-S661.

Zhang, Lequan, Xiaochen Xu, Changhong Hu, Lei Sun, Jesse T Yen, Jonathan M Cannata, and K Kirk Shung. 2010. "A high-frequency, high frame rate duplex ultrasound linear array imaging system for small animal imaging." *IEEE transactions on ultrasonics, ferroelectrics, and frequency control* 57 (7).

Zhang, Yu-Hua, Cheng-Wu Zhang, Zhi-Ming Hu, and De-Fei Hong. 2016. "Pancreatic cancer: Open or minimally invasive surgery?" *World journal of gastroenterology* 22 (32): 7301.

Zhou, Dan, Kwok Fung Cheung, Yan Chen, Sien Ting Lau, Qifa Zhou, K Kirk Shung, Hao Su Luo, Jiyan Dai, and Helen Lai Wa Chan. 2011. "Fabrication and performance of endoscopic ultrasound radial arrays based on PMN-PT single crystal/epoxy 1-3 composite." *IEEE transactions on ultrasonics, ferroelectrics, and frequency control* 58 (2).

Zhou, Qifa, Dawei Wu, Changgeng Liu, Benpeng Zhu, Frank Djuth, and K Kirk Shung. 2010. "Micro-machined high-frequency (80 MHz) PZT thick film linear arrays." *IEEE transactions on ultrasonics, ferroelectrics, and frequency control* 57 (10).

Zipparo, Michael, Clyde Oakley, Rich Denny, Said Azim, WL Gore, V Balannik, Z Soferman, M Berman, R Nechushtai, and D Kopelman. 2008. "3-D laparoscopic imaging." Ultrasonics Symposium, 2008. IUS 2008. IEEE.

Zou, C., Z. Sun, D. Cai, S. Muhammad, W. Zhang, and Q. Chen. 2016. "A Fast Method to Calculate the Spatial Impulse Response for 1-D Linear Ultrasonic Phased Array Transducers." *Sensors (Basel)* 16 (11).

APPENDIX A:

OPTIMIZED IMPULSE RESPONSE SCRIPT

The following section presents a Python® function developed by the author for the calculation of the impulse response function, the function allows for the calculation of the impulse response using one process that works for all geometries.

```
1   import numpy as np
2   import math
3
4   def                                    FUNC_impulse_response_inter-
5   cepts(time_step_f,c_f,a_f,b_f,x_f,y_f,z_f,round_factor_f):
6       impulse_array_f =   [0]
7       arc_radius      =   []
8       impulse_time = []
9       tau_max_f = (((x_f+a_f)**2 + (y_f+b_f)**2 + z_f**2)**0.5)/c_f +
10  time_step_f*10
11      if  ((x_f >= a_f) and (y_f >= b_f)):
12          tau_min_f = ((x_f-a_f)**2 + (y_f-b_f)**2 + (z_f)**2)**0.5/c_f
13      elif((x_f <  a_f) and (y_f >= b_f)):
14          tau_min_f = ((y_f-b_f)**2 + (z_f)**2)**0.5/c_f
15      elif((x_f >= a_f) and (y_f <  b_f)):
16          tau_min_f = ((x_f-a_f)**2 + (z_f)**2)**0.5/c_f
17      elif((x_f<a_f)and(y_f<b_f)):
18          tau_min_f = z_f/c_f
19      tau_min_f = tau_min_f #- time_step_f
20
```

```python
    for                              i_f                                    in
range(int(round(math.ceil(tau_min_f/time_step_f))),int(round(tau_max_f/
time_step_f))):

        #transit_time.append(i*time_step_f)
        arc_radius = (c_f**2*(i_f*time_step_f)**2 - z_f**2)**0.5
        if(type(arc_radius)==complex):  #if the arc_radius is a complex
number then don't start computing (sometimes pops up due to rounding
errors - theorectially this should never occur but float's aren't in-
finitly precise)
            impulse_array_f.append(0)
        else:
            impulse_time.append(i_f*time_step_f)
            intersection_array = []    #x value relative to element cen-
ter, y value rel to element center, theta to point from P* rel to +x axis

            if(abs(y_f-b_f)<arc_radius):
                dXt = (arc_radius**2 - (y_f - b_f)**2)**0.5
                if(-a_f<=(x_f-dXt)<=a_f):
                    intersection_array.append([x_f-dXt,b_f,np.arctan2(-
(y_f - b_f) , (-dXt)) + 2*np.pi*(-(y_f-b_f)<0) ,-1]) #note arctan2(y,x)
(takes Y BEFORE X)
                if(-a_f<=(x_f+dXt)<=a_f):
#-1 is a place holder for the 'transistion variable' that marks if the
arg segment clockwise from the point is in or out of the element
                    intersection_array.append([x_f+dXt,b_f,np.arctan2(-
(y_f - b_f) , (+dXt)) + 2*np.pi*(-(y_f-b_f)<0),-1]) #arctan2(location to
intercept rel to P*)

            if(abs(y_f+b_f)<arc_radius):
                dXt = (arc_radius**2 - (y_f + b_f)**2)**0.5
                if(-a_f<=(x_f-dXt)<=a_f):
                    intersection_array.append([x_f-dXt,-
b_f,np.arctan2(-(y_f+b_f),-(dXt)) + 2*np.pi*(-(y_f+b_f)<0),-1])
                if(-a_f<=(x_f+dXt)<=a_f):
                    intersection_array.append([x_f+dXt,-
b_f,np.arctan2(-(y_f+b_f),+(dXt)) + 2*np.pi*(-(y_f+b_f)<0),-1])
```

144

```
58
59                  if(abs(x_f-a_f)<arc_radius):
60                      #discard duplicate points if they exist
61                      dYt = (arc_radius**2 - (x_f - a_f)**2)**0.5
62                      if(-b_f<= (y_f-dYt)<=b_f):
63                          tmp_ang = np.arctan2((-dYt),(a_f-x_f)) + 2*np.pi*(-
64      dYt<0)  #Second part wraps the angle so all angles are 0 <-> 2pi instead
65      of -pi <-> pi (if y value is negitive the angle is, so this just says add
66      2pi to angle if y term is negative)
67
68                          #step thourgh the rows in the array pulling the theta
69      value (gives array of angles)
70                          #if the angle already exists don't log a second time
71                          if(len([row[2]   for   row   in   intersection_array
72      if(abs(row[2] - tmp_ang) < round_factor_f)])<1): #take the angles from
73      the array of points that intersect the element, if this point has already
74      been logged (or if one VERY close to it has been logged) then don't bother
75      logging the point a 2nd time
76                              intersection_array.append([a_f,y_f-
77      dYt,tmp_ang,-1])
78                      if(-b_f<= (y_f+dYt)<=b_f):
79                          tmp_ang    =    np.arctan2((+dYt),(a_f-x_f))    +
80      2*np.pi*(+dYt<0)
81                          if(len([row[2]   for   row   in   intersection_array
82      if(abs(row[2] - tmp_ang) < round_factor_f)])<1): #don't duplicate points
83      intersection_array.append([a_f,y_f+dYt,tmp_ang,-1])
84              if(abs(x_f+a_f)<arc_radius):
85                  dYt = (arc_radius**2 - (x_f + a_f)**2)**0.5
86                  if(-b_f<= (y_f-dYt)<=b_f):
87                      tmp_ang = np.arctan2((-dYt),-(x_f+a_f)) + 2*np.pi*(-
88      dYt<0)
89                      if(len([row[2]   for   row   in   intersection_array
90      if(abs(row[2] - tmp_ang) < round_factor_f)])<1):
91                          intersection_array.append([-a_f,y_f-
92      dYt,tmp_ang,-1])
93                  if(-b_f<= (y_f+dYt)<=b_f):
```

```python
94                          tmp_ang        =       np.arctan2((+dYt),-(x_f+a_f))      +
95      2*np.pi*((y_f+dYt)<0)
96                          if(len([row[2]    for    row    in    intersection_array
97      if(abs(row[2] - tmp_ang) < round_factor_f)])<1):
98                              intersection_array.append([-
99      a_f,y_f+dYt,tmp_ang,-1])
100                 if(len(intersection_array)==0): #if the array doesn't hit a
101     side but t>t_min then we know that the full radiation arc is covered by
102     the element
103                     intersection_array.append([arc_radius,0,0,-1])
104                 #turn array into array to ease handling
105                 intersection_array = np.array(intersection_array)
106                 #wrap array so theta values start counting at 0 and increase
107     as we move around the Z axis in the +Z direction (RHR)
108                 #[intersection_array[:,2][i] = intersection_array[:,2][i] +
109     2*pi  for  i  in  range(0,np.shape(intersection_array)[1])  if(intersec-
110     tion_array[:,2][i]<0)]
111                 #sort intersection array
112                 intersection_array  =  intersection_array[intersection_ar-
113     ray[:,2].argsort()]
114
115                 active_arc_length = 0
116                 for i2 in range(0,np.shape(intersection_array)[0]):
117                     ref_ang = intersection_array[:,2][i2]
118                     prev_ang     =      intersection_array[:,2][i2-1]     -
119     2*np.pi*(i2==0)
120                     theta_mid = (ref_ang+prev_ang)/2
121                     midpoint = [x_f + arc_radius*np.cos(theta_mid), y_f +
122     arc_radius*np.sin(theta_mid)]
123                     if((-a_f < midpoint[0] < a_f)and(-b_f < midpoint[1] <
124     b_f)):  #if point on arc segment is in array then the preceding segment
125     was in the element
126                         active_arc_length = active_arc_length + (ref_ang -
127     prev_ang)
128                 #if(active_arc_length != 0):
129                 impulse_array_f.append(active_arc_length/(2*np.pi))
130         return tau_min_f,impulse_array_
```

APPENDIX B:

CLINICAL APPLICATIONS AND EXISTING ULTRASONIC TECHNOLOGIES

The following appendix provides a review of existing applications and solutions to the challenges of endoscopic probes and high-resolution imaging. This section begins with a discussion of the endoscopic applications of ultrasound and a review of some current solutions. From there this work presents an analysis of existing high-frequency ultrasound applications and a discussion of applications that benefit from high-resolution high-frequency ultrasound probe within an endoscopic package.

B.1   EXISTING APPLICATIONS OF ENDOSCOPIC ULTRASOUND

Table B-1 lists current literature on endoscopic ultrasound and summarizes the applications and probe sizes. Additionally, this review identifies the imaging method. Though manufacturers are currently producing endoscopic ultrasound devices for vascular imaging applications, significant design compromises are needed to achieve a small form-factor. Through some of these devices use high-frequency elements, the design compromises result in lower image quality (Fujifilm 2016; Phillips 2017; St.Jude-Medical 2015).

Intravascular ultrasound (IVUS) endoscopes are of note as they present designs that are close to satisfying the requirements of minimally invasive surgical procedures. IVUS endoscopes provide visualization of vascular plaques but incorporate design compromises that reduce image quality (Ma et al. 2016). Typically, these devices have a low lateral resolution due to a low element count or a side-facing field of view. Methods such as the translation of a single element or multiplexing elements within an IVUS array are used to decrease the number of electrical connections (Szabo 2004; Cox et al. 2017; Ma et al. 2016; Y. Wang, Stephens, and O'Donnell 2001; Wildes et al. 2016). These compromises can

result in a reduced lateral resolution, lower signal to noise ratio (SNR), induce motion artifacts, and deteriorated image quality.

Table B-1: Endoscopic imaging – application summary

Application	Size - (mm)	Field	Technology	Reference
Esophagus	6 - 12	Gastro-intestinal	Optical Imaging, Resection	(Fujifilm 2016; Scientific 2015)
Full GI Tract	10-13	Gastro-intestinal	Ultrasonic Capsule Endoscopes	(Anbarasan et al. 2017; Cox et al. 2017; Lee et al. 2014; Gora et al. 2013)
Forward-Viewing	14	Gastro-intestinal tract wall imaging	Forward-viewing endoscopic ultrasonic imaging	(Mekky 2014; Olympus 2014)
Intracardiac	1 - 4	Intracardiac Echography	Ultrasonic Imaging (ICE)	(Y. Wang, Stephens, and O'Donnell 2001; Wildes et al. 2016)
Angiography	2 - 3	Intravascular Ultrasound	Ultrasonic Imaging (IVUS)	(Phillips 2017; Vogt et al. 2010)
General Surgery	5-12	Laparoscopic	Ultrasound - low-frequency - side-facing	(BK-Ultrasound 2015; Hitachi 2012)
Endonasal	4 - 7	Neurosurgery	Optical Imaging	(Storz 2018)
Keyhole - Neuro	4	Neurosurgery	3D Video Endoscope	(Storz 2017)
Tumor Ablation	2 - 3	Cancer (Liver)	Ultrasonic Therapy, MRI Imaging	(Tait, Yong, and Cuschieri 2002)
Acoustic Neuroma	3 - 4	Auditory	Optical Endoscope	(Wackym et al. 1999)
Spinal Surgery	2 - 12	Spinal	Optical Endoscope	(Wagner et al. 2017; Ruetten et al. 2008)

As discussed by Schembre, Ayub, and Jiranek (2005), low-resolution images restrict the accurate assessment of various pathologies. Therefore, literature was reviewed to determine applications that would benefit from high-resolution ultrasonic endoscopes. The reviewed endoscopic imaging applications listed fall into three main categories:

- Applications where the anatomy allows for endoscopes larger than 10 mm in diameter, such as gastrointestinal imaging

- Applications that require endoscopes under 4 mm in diameter, but where the imaged anatomy is very specific and some image artifacts can be tolerated, such as intracardiac and intravascular imaging

- Applications that can support probes 4 mm in diameter, but where high-resolution and artifact-free images are required. Imaging applications such as the auditory system, spinal structures, laparoscopic, and neurosurgical

Of these categories, the third set of applications presents the most significant opportunity for the application of a forward-looking high-resolution ultrasonic endoscope. As such, the design work discussed in this thesis focuses on developing a solution for those applications.

B.2   EXISTING TECHNOLOGIES FOR ULTRASONIC ENDOSCOPY

As discussed by Szabo and Lewin (2013), the selection of an appropriate transducer to meet the needs of the application is an essential step towards successful diagnosis. A review of existing applications and technologies is listed in Table B-1, and suggests that an endoscopic probe with a diameter of 4 mm would be of use in several minimally invasive procedures. As such, existing endoscopic solutions within $4 \text{ mm} \pm 50\%$ have been investigated and their general design characteristics are summarized below.

- Mechanically translated single element transducers
- Sparse side-looking arrays
- Ring arrays

The following sections summarize these devices, and Figure B-1 gives a general reference of the volumes that the various transducer technologies can image.
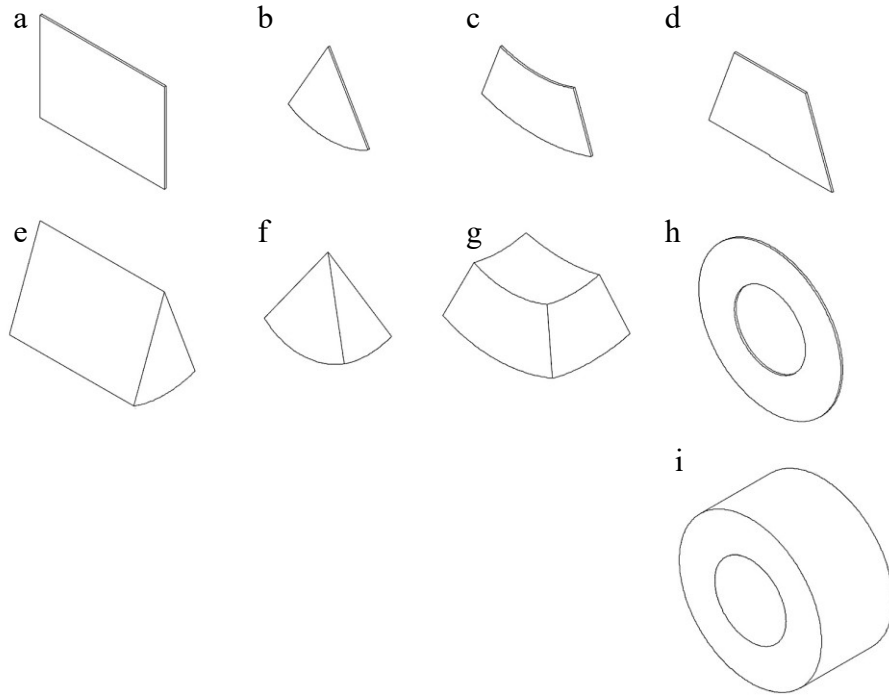
Figure B-1: Fields of view produced by ultrasonic transducer designs. Adapted from (Szabo and Lewin 2013). (a) 2D rectangular field of view; (b) 2D sector view; (c) 2D convex sector; (d) 2D trapezoidal; (e) 3D rectangular sweep; (f) 3D fan; (g) 3D truncated prism; (h) 2D annulus; (i) 3D annulus

B.2.1 MECHANICALLY TRANSLATED SINGLE ELEMENT TRANSDUCERS

Figure B-2 shows an illustrative example of a mechanically translated single element transducer. Vascular and cardiac imaging applications (IVUS and ICE) employ these designs due to the small probe diameter. The single element transducer only allows for the acquisition of a single A-mode image line at a time. The element rotates or slides within the device housing to acquire adjacent scan lines. The processing system then stitches together the scan lines to form a two-dimensional (cross-sectional) image. The guidewire controls the motion of the transducer, and the ultrasound system controller matches the motion of the wire to the expected line location in the image.

150
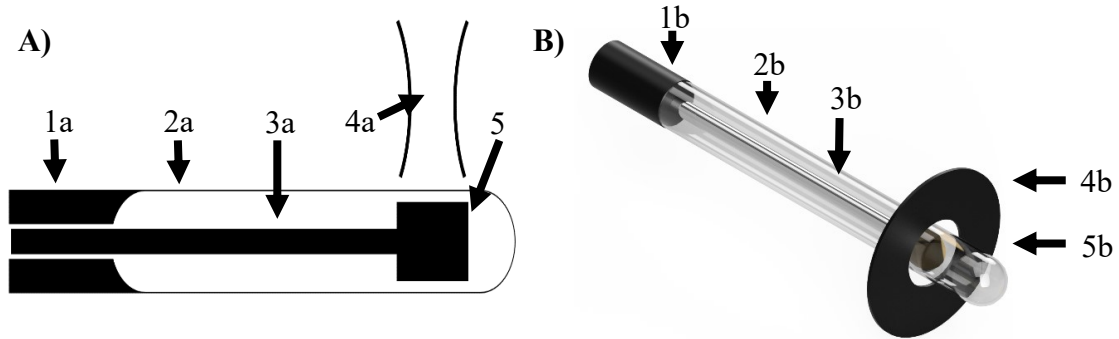
Figure B-2: (A) Depicts a wireframe model of a side-facing mechanically rotated ICE catheter probe head. The probe is located on the distal end of a long flexible shaft and is typically 2-3 millimeters in diameter. (1a & 1b) indicate the device cable sheath (2a & 2b) indicate the acoustically transparent device housing (3a & 3b) indicate the mechanical and electrical interconnect to the transducer (4a & 4b) indicate the device's field of view (5a & 5b) depict the ultrasonic transducer element

Mechanically scanned transducers have the advantage of being relatively compact as only one electrical interconnection is required. However, imprecision in the mechanical translation of the transducer can causes image artifacts. Additionally, the single element transducer is typically only focused at one image depth, and so resolution suffers at deeper focal depths, though some manufacturers alleviate this issue by adding multiple elements (Szabo and Lewin 2013). Depending on the level of sophistication, these transducers can provide a 2D rectilinear field of view, a 2D annulus field of view, or a 3D annulus field of view.

B.2.2 SIDE FACING ARRAYS

An endoscopic side facing array is shown in Figure B-3 based on the work discussed by Cabera-Munoz et al (2019). This side facing array beamforms pulses to the array elements allowing for the acquisition of scan lines and two-dimensional image generation.

A)
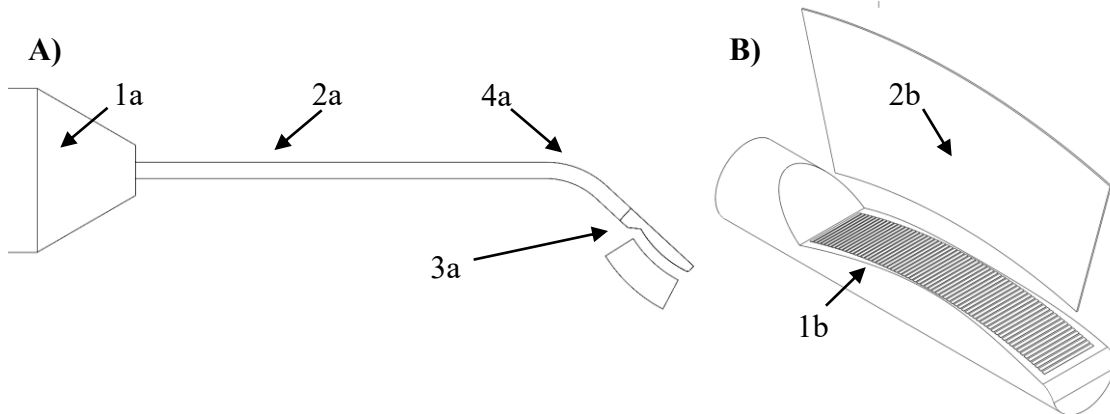
Figure B-3: An illustrative example of a 5 mm diameter laparoscopic endoscope. (1a) probe handle, (2a) probe shaft, (3a) imaging array, (4a) flexion point, (1b) transducer element array, and (2b) convex sector field of view. The transducer geometry shown in this image roughly approximates that of the I12C4f array developed by bk ultrasound and described in (H. Jensen et al. 2018). This figure does not include matching layers or lenses for illustrative effect. Orienting the array along the axis of the shaft axis expands the area available for the array and its electrical connections in comparison to a forward-facing array. However, this prevents the array from being able to image in front of the endoscope.

Though current commercial systems typically utilize sparse arrays with relative poor image resolution, researchers have produced high-frequency arrays with one-wavelength element pitch (Cabrera-Munoz et al. 2019). The main trade-off in these arrays is that the array is side facing and does not image the material in-front of the array stack. As discussed in (Wackym et al. 1999), minimally invasive surgical procedures benefit from forward-facing visualization devices as they allow for the smallest and least invasive surgical pathways.

B.2.3 RING ARRAYS

Below are described two representative examples of ring array transducers. These transducers are typically used in intravascular imaging applications where their small diameter (<5 mm) and hollow core allow for insertion into veins and arteries to image vascular plaques and stents while also allowing for co-registration with guidewires. These devices are highly tailored to their applications providing high axial resolution but suffer from poor lateral resolution and a limited field of view.
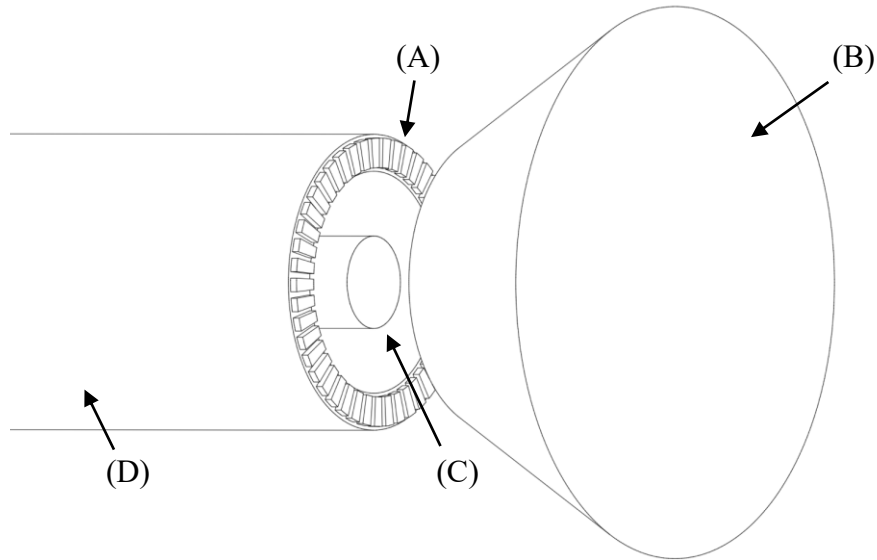
Figure B-4: Forward-facing ring array transducer composed of (A) a forward-facing transducer array, (B) the forward-facing conical field of view, (C) a guidewire inserted through the hollow internal working channel and (D) a flexible sheath.

Ring arrays have the transducer elements arranged in an annular ring around a working channel (as shown by Figure B-4.A). The two-dimensional geometry of the array allows the transducers to image a three-dimensional volume (Figure B-4.B) in front of the array. However, the small element size means that the pulses are weak, and the signal to noise ratio of the arrays suffers. The primary benefit of the construction technique is that it can provide a hollow core within the array, allowing for a guidewire or surgical instrument.
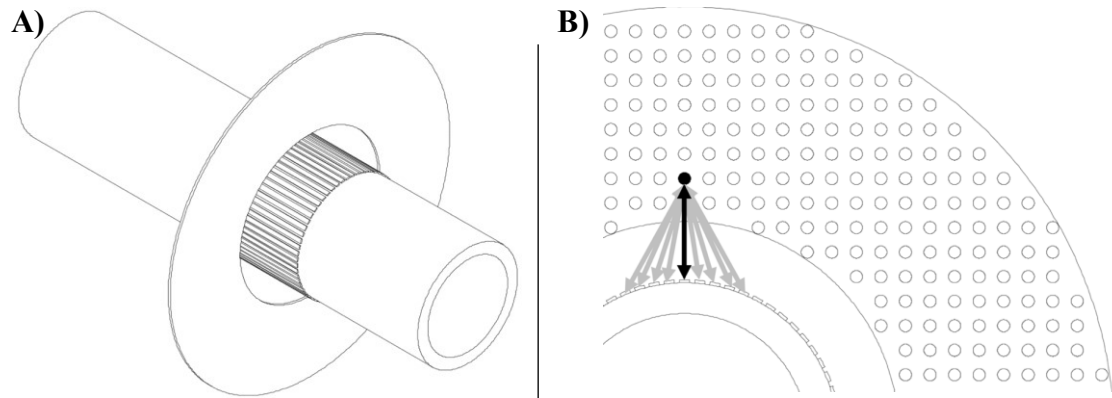
Figure B-5: Radial ring array with 64 elements and radial field of view. (left) shows the arrangement of transducer elements allowing for a radial field of view while (right) shows an illustrative example of pixels within the two-dimensional field of view. Intensity plots for each pixel are constructed by summing the respective signal strengths from each element that can image the pixel, signals from elements that are angled too far away from the pixel are not included. This array is based on the 64-element radial array transducer described in (Vince and Davies 2004)

Figure B-5 shows a ring array transducer with a radial arrangement of side-facing elements. The transducer allows for radial imaging of vascular tissue and plaques as required by intravascular imaging applications. However, the limited number of elements facing a given pixel restricts the lateral resolution of the probe and the depth of field.

B.2.4 EMERGING TECHNOLOGIES

Developments in capsule endoscopy for imaging the gastrointestinal tract are of interest to the work completed within this dissertation despite the relatively large diameter of proposed designs (~10 mm) due to the high element density (Lay et al. 2018) and the use of a wireless antenna for data transmission (Faerber et al. 2018). The use of a wireless antenna for data transmission may provide a method whereby future designs may be able to avoid the use of sizeable coaxial cable assemblies for data transmission.
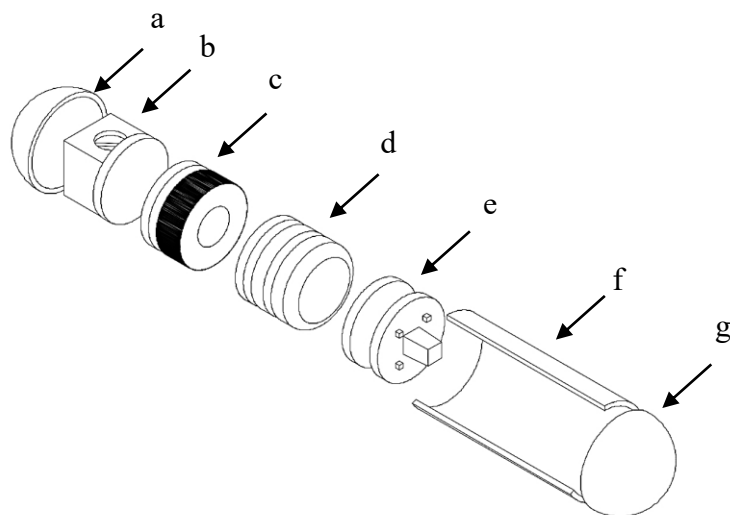
Figure B-6: A 10 mm x 30 mm untethered capsule integrating co-registered optical and ultrasonic imaging with image adapted from (Cox et al. 2017) for illustrative purposes (a) optical lens; (b) fluorescence imaging module and PCB; (c) ultrasonic array and application-specific integrated circuit; (d) battery module and PCB; (e) light module and camera; (f) cross-sectioned capsule shell with integrated radio antenna; (g) optical lens

Figure B-6 presents an untethered capsule design that incorporates a 512-element ultrasonic ring array into the 10 mm diameter by 30 mm long untethered capsule. Simulations of the endoscope, as discuss by Lay et al. (2018), present a basis for the design of high-resolution imaging devices discussed in this work due to the concise and systematic presentation of the simulation approach.

B.3   SUMMARY

IVUS and ICE probes are single element transducers and would produce higher quality images if they did not rely on the physical translation of the element. Ultrasonic arrays of elements can generate images by controlling the pulsing sequence to shift the scan line without motion of the array. Ideally, IVUS and ICE probes could be built out of ultrasonic arrays so that the physical translation of the transducer is not required. However, current fabrication techniques prevent high-resolution ultrasonic arrays from being built at that scale. Although side-facing arrays provide an endoscopic form-factor and high-resolution images, minimally invasive procedures require a forward-facing perspective to minimize the size of the surgical pathway. Ring-arrays have achieved many of these goals and allow

for three-dimensional imaging; unfortunately, the signal strength is weak, and the field of view is limited as a result.

Minimally invasive procedures require the development of a high-resolution ultrasonic phased array in an endoscopic form-factor of approximately 4 mm in diameter. This development would provide surgeons and diagnostic imaging specialists with a tool to investigate many new and novel imaging applications beyond those discussed in this work. Many diagnostic imaging applications do not have access to a real-time cross-sectional imaging device due to the tight size constraints of the applications. This development could lead to significant improvements in patient care by providing clinicians with a powerful diagnostic tool.

APPENDIX C:

POTENTIAL APPLICATIONS OF HIGH-FREQUENCY ULTRASOUND

An initial focus of the probe designed within this thesis was limited to applications that matched well to existing endoscopic applications, listed in Table C-1. These applications are:

- Neurosurgical imaging
- Auditory system
- Spinal imaging
- Small animal (preclinical)

These applications have an unmet clinical need for a high-resolution forward-facing endoscope capable of providing depth-resolved images. The ability to successfully image the smallest structures of interest determines the required resolution for a given application. In the above-listed applications, the smallest structures of surgical interest are nerve fibers ranging in size from approximately 0.6 mm to 5 mm (Beekman and Visser 2004), and as such, a resolution of 100-200 μm is the desired resolution range.

Table C-1: List of emerging and established applications of high-frequency ultrasound with related references

Field	Application	Reference
Vascular	Radial Artery	(B.-B. Zhang et al. 2017)
	Venous Valves	(Mlosek and Malinowska 2014)
	Intima-Media Thickness	(Mohler et al. 2009)
	Peripheral Vasculature	(Zemp et al. 2007)
	Blood Flow Patterns	(Goertz et al. 2002)

Field	Application	Reference
Small Parts	Nerves	(Forte et al. 2019)
	Thyroid and Glands	(Lew and Solorzano 2010)
	Lymph Nodes	(Li et al. 2013)
	Hand Surgery	(Viviano, Chandler, and Keith 2018)
Dermatology	Skin Layers	(Van Mulder et al. 2017)
	Melanoma	(Viviano, Chandler, and Keith 2018)
	Lipomas	(Rahmani, McCarthy, and Bergin 2017)
	Lesions and Bruising	(J. Kim et al. 2019)
Auditory System	Acoustic Neuroma and Middle ear diagnosis	(Wackym et al. 1999; Torbatian 2012)
Musculoskeletal (MSK)	Superficial Joint Segments	(Hacihaliloglu 2017)
	Tendons	(Viviano, Chandler, and Keith 2018)
	Medial Meniscus	(Viren et al. 2017)
Neonatal/Pediatric	Vasculature	(Latham et al. 2013)
Neurosurgical	Imaging	(Schiavone et al. 2017)
Guided Biopsy	General Endoscopic	(McPhillips 2017)
	Breast Cancer	(Cummins, Eliahoo, and Kirk Shung 2016)
Dental	Caries (cavities)	(J. Kim et al. 2019)
Ocular	Diagnostics	(Rosen et al. 2019)
Intravascular (endoscopic)	Arteriosclerosis	(Janjic et al. 2018; Colchester et al. 2019; Degertekin, Guldiken, and Karaman 2006)

The following sub-sections discuss the above-listed applications of high-frequency ultrasound that match well to endoscopic imaging applications.

C.1 NEUROLOGICAL IMAGING

Current optical probes for imaging during neuro-surgical procedures can range from 4-7 mm in diameter (Storz 2017; Medtronic 2016). However, these probes only provide a topological view of the tissue morphology. In some brain tumor resection procedures, failure rates range between 50% to 90% (Di Ieva et al. 2014). As such, there is a critical need for technologies that facilitate the detection of cancerous tissue with precision visualization of the boundaries between healthy tissue and tumor. The proposed endoscope would allow cancerous tissue to be accurately detected and removed while preserving healthy brain tissue. As discussed by Wang, Stephens, and O'Donnell (2001), ultrasound has proven to be adept at the differentiation of healthy tissue from cancerous tissue.

Current brain tumor resections use small surgical tools that access surgical pathways through small access ports drilled into the skull. Surgeons navigate using magnetic resonance or computed tomography images that were acquired pre-operatively. Navigation is conducted by co-registering the static volumetric image with real-time markers on the surgical instruments. However, MR and CT images are acquired pre-operatively, and the brain tissue can shift during the procedure, causing misregistration of the tool and the expected anatomy by up to 20 mm (Sosna et al. 2005). Although MR and CT images can be recaptured during the procedure (Hammoud et al. 1996), this only provides a snapshot at a specific time point, and shifts can still occur. Intraoperative images also increase the duration, complexity, and cost of the surgery.
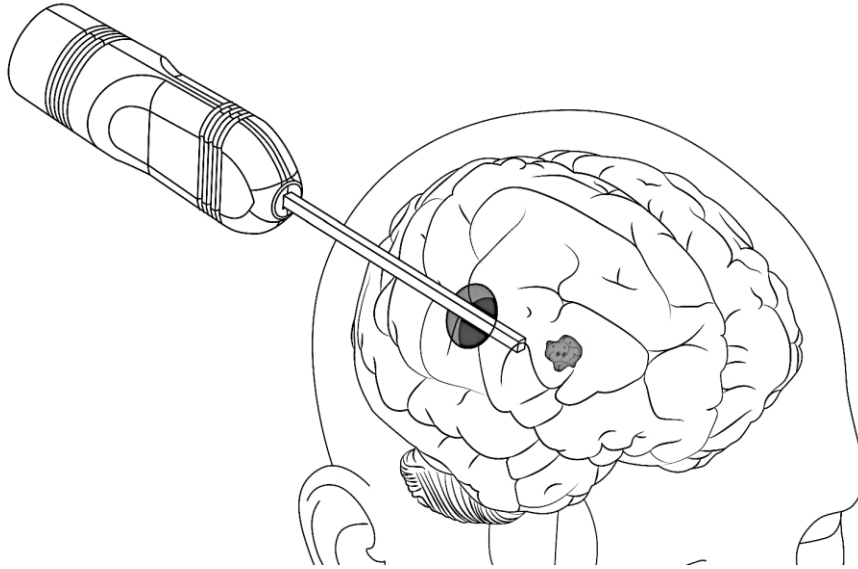
Figure C-1: Example of a neurosurgical procedure where an ultrasonic endoscope is used to visualize a cancerous mass after being inserting into the brain through a surgical opening in the skull.

Optical endoscopes and microscopes are prevalent tools for neurosurgical guidance (Medtronic 2016). However, these probes only provide a topological view of the tissue morphology. In some of the most common brain tumor resections, failure rates ranging between 50% to 90% were reported (Di Ieva et al. 2014). As such, a critical need exists for real-time tomographic imaging technologies that facilitate the detection and differentiation of cancerous tissue to help reduce the failure rate and improve surgical efficacy. Specifically, a solution is needed that allows cancerous tissue to be accurately detected and removed while preserving healthy brain tissue, a task that ultrasound has proven to be adept at (Hammoud et al. 1996).

C.2 EAR IMAGING

Commercially available technologies cannot provide in-vivo images of the fine structures of the middle ear. Though high-frequency ultrasound has been proven to have the required resolution (Wildes et al. 2016), the existing devices are too large to fit within the ear canal. The proposed high-frequency endoscope would have the size required to image the middle ear structures while being small enough for insertion into the ear canal. Potentially, this research could allow for a more accurate diagnosis of hearing disorders.

Otologic diagnostics are limited in many respects, being based mainly on the patient's symptoms and functional hearing tests (audiograms). Other, more specialized tests can be performed to help to confirm the diagnosis or extent of the disease, such as auditory brain-stem evoked potentials, otoacoustic emissions, or vestibular testing (Torbatian 2012). However, these tests only inform surgeons on the functionally of the auditory system, but not on the anatomical cause. Exploratory surgeries are often required to link a functional limitation, such as a reduced high-frequency hearing threshold, to an anatomical pathology such as an arthritic stapes. This requirement contrasts with other medical fields, where imaging techniques have revolutionized diagnostic procedures, allowing for visualization and diagnosis of the pathologies before surgical intervention.
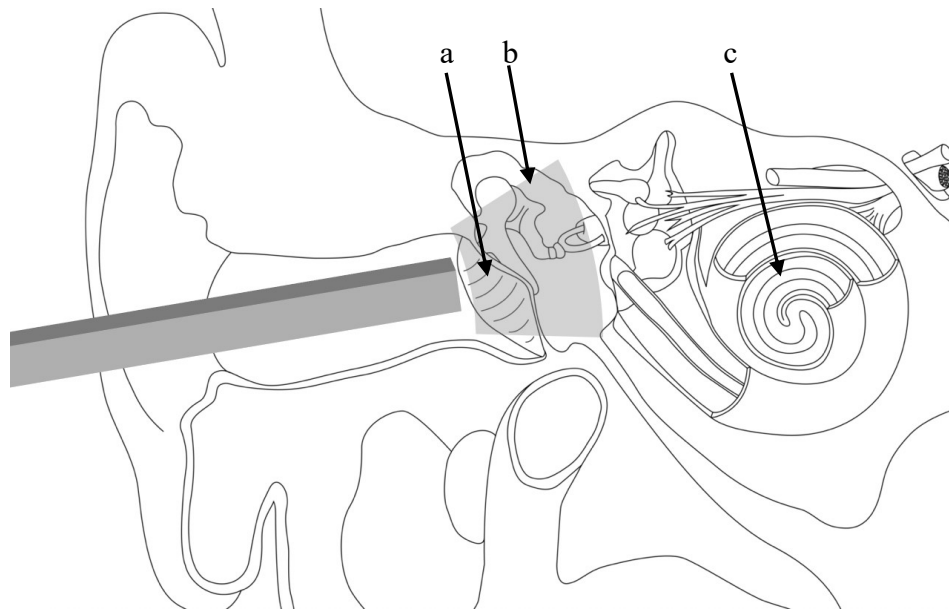
Figure C-2: Example of an Otolaryngology procedure by which the middle ear is being imaged by an endoscopic ultrasonic probe inserted into the ear canal. The probe's field-of-view shown in grey. Image adapted from reference figures within (Netter 2014). (a) shows the tympanic membrane where sound is translated into vibrations of tissue; (b) indicates the ossicles of the middle ear which translate the vibrations through the middle ear; (c) is the inner ear's cochlea where acoustical vibrations are translated into electrical action potentials which are relayed to the brain.

Medical imaging technologies have limited value in otolaryngological applications as the structures of the ear are smaller than in most other organs of the body. Additionally, the

skull conceals the structures of the middle and inner ear and limits access. The tympanic membrane (eardrum) is approximately 60 to 110 μm thick (Aernouts, Aerts, and Dirckx 2012), and the ossicles are the smallest bones in the body with dimensions on the order of several millimeters. At approximately 10 mm in diameter, the cochlea is relatively large, but the structures of interest within it, the basilar membrane, organ of Corti and hair cells, all have dimensions measured in the range of μm. MRI and CT have a typical resolution in the millimeter range for imaging in vivo (Juliano, Ginat, and Moonis 2013; Rousset et al. 2014). Figure C-3 (right) shows a typical high-resolution CT scan of the middle ear. In it, the ossicles are barely distinguishable, and as such, these images have limited diagnostic value.
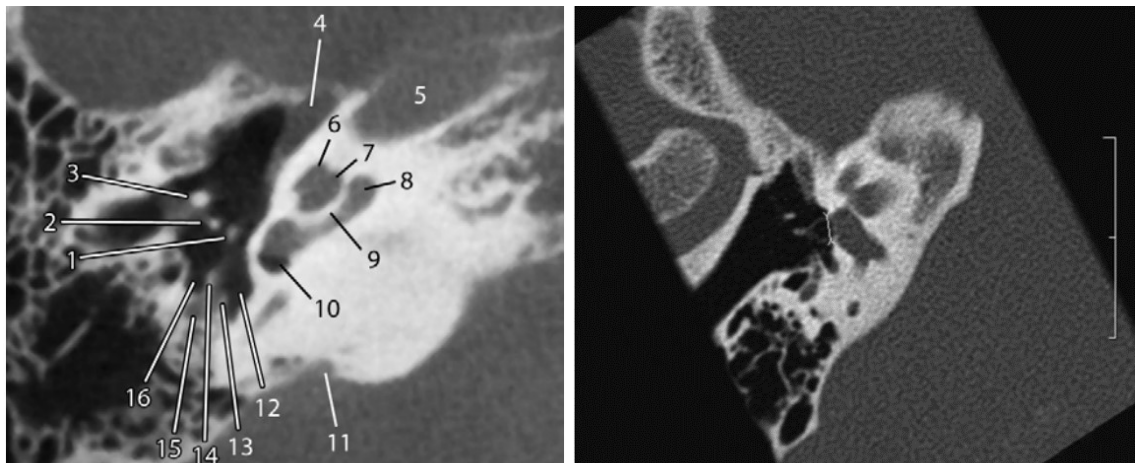
Figure C-3: Resolution of current imaging technologies. (left) shows an image collected with MR by Juliano et al (2013) with feature '2' indicating the stapes; (right) shows a high-resolution CT image collected by Rousset et al (2014)

Though high-frequency ultrasound has been proven to have the required resolution (Torbatian et al. 2009; Landry et al. 2018), the devices used for these studies are too large to fit within the ear canal, and the studies used excised tissue. Recent work on optical coherence tomography imaging systems reports an additional solution to this clinical need (MacDougall et al. 2016). In this application, OCT has the advantage of not requiring the insertion of an acoustic coupling medium (ideally saline solution) into the middle ear. However, high-frequency ultrasound may be more useful for middle ear pathologies where an opaque fluid or pus prevents the transmission of light.

C.3 SURGICAL GUIDANCE – SPINAL

Up to 80% of the population experience lower back pain related to spinal pathologies at some point in life, and currently 1-2% of the adult population in the United States are disabled due to lower back pain (Friedly, Standaert, and Chan 2010). Surgeons are working to develop novel and effective treatments to aide in the resolution of the various pathologies. As such, many surgeons are moving to minimally invasive approaches to reduce trauma to surrounding muscles and tissue(Skovrlj et al. 2015), thereby reducing recovery times and improving outcomes. Table C-2 presents a subset of minimally invasive procedures requiring high-resolution imaging of the spinal nerve fibers as failed back surgery procedures are often the result of post-operative nerve impingement (Baber and Erdek 2016).

Table C-2: Limited summary of spinal procedures utilizing endoscopic surgical procedures

Procedure	Description	Reference
Fusion	Addresses a condition in which excessive movement between vertebrae stresses nerve fibers and tissues. The procedure involves the use of graft material to fuse multiple vertebrae, preventing movement.	(Y.-C. Chen et al. 2019; Park et al. 2018; John-Hopkins 2019)
Decompression	Addresses a condition in which pressure on the spinal cord or nerves causes pain or paralysis. The procedure involves the removal of impinging tissue, which may be thickened bone, a herniated disc or the lamina. Includes variants such as: foraminotomy, laminectomy, and discectomy	(McAnany et al. 2015; Wagner et al. 2017; Lawrence and Hayek 2013; Phan and Mobbs 2016)
Vertebroplasty	Addresses compressive fractures to the vertebrae typically arising from osteoporosis. The procedure involves the injection of bone cement into the vertebrae to strengthen the remaining structure.	(ASA Retrived_2019; Cheng and Liu 2019)

Minimally invasive approaches for spinal surgeries utilize various systems of tubes, freehand working channels, and tubular retractors to establish the surgical pathways and expose

the anatomy of interest (Brayda-Bruno and Cinnella 2000). For visualization, current procedures use endoscopic (optical) microscopes. At the end of the procedure, the surgeon must check the surgical site for retained disc fragments and residual compression tests completed by probing the nerves for excessive tension using specialized 'nerve hooks' (Yin et al. 2016).

Standard clinical imaging technologies such as MRI and CT do not have enough resolution to visualize the nerve roots, which can be as small as 100 and 200 μm in diameter. An endoscope, less than 4 mm in diameter, and with a resolution on the order of 100 μm could potentially replace the nerve hook technique with a direct and quantifiable visualization technique.

Minimally invasive procedures for spinal surgery can result in a tenfold increase in the radiation dose experienced by the surgeon when compared to similar procedures performed non-invasively (Shearwood and Goldstein 2017). The increased dose results from the use of ionizing radiation modalities for imaging during the minimally invasive procedures and the limited ability to visualize the tissue through other methods. This work aims to provide surgeons with a non-ionizing imaging device that will be capable of imaging the required structures, thereby reducing risks and improving outcomes.

C.4   SMALL ANIMAL IMAGING

Currently, there are a handful of commercially available high-frequency imaging systems that are suitable for pre-clinical imaging of small animals. However, these systems are limited to large topical probes and prohibit researchers from visualizing organs that are shielded by bone in the animals. As in human cardiac imaging, where phased array transducers allowed for visualization of the heart from a small opening between rib bones (Packer et al. 2002), a miniature high-frequency phased array could do the same in small animal imaging applications. Specifically, brain imaging of small animals is difficult when using standard probes since large sections of the skull must be resected in order to visualize the brain anatomy with high resolution.

The extensive resections of skull result in high morbidity rates and prohibit long term studies. A probe with a less than or equal to 4 mm size could allow researchers to perform smaller craniotomies, allowing for longitudinal studies of the rodent brain.

C.5 SUMMARY

Minimally invasive surgical procedures would benefit from the use of ultrasound as it provides real-time depth-resolved images of tissue. However, we see that standard ultrasound probes are too large to be used for minimally invasive imaging applications. However, since the active transducer element size is inversely proportional to frequency (Szabo 2004), high-frequency probes can be much smaller, allowing for high-resolution imaging during endoscopic procedures.

A review of the literature indicates that there is a strong need for a high-resolution, forward-looking tomographic imaging device in an endoscopic form-factor that does not use ionizing radiation. Tomographic, to provide cross-sectional images into unexposed tissue, and endoscopic so that the probe can fit within minimally invasive surgical pathways. Other design priorities include high framerate, fine image resolution, and a large field-of-view.

APPENDIX D:

CALCULATION OF LENS AND MATCHING LAYER PARAMETERS

The use of a vacuum deposition mass-spring and ¼λ matching layer technique was selected due to the high-frequency (40 MHz) of the arrays. At these frequencies the imperfections associated with traditional bonded matching layer application procedures become a significant impediment to the operation of the transducer. As discussed in (Desilets, Fraser, and Kino 1978) the desired impedance for the mass-spring matching layer was determined by Equation (D-6-1).

$$Z_{\frac{\lambda}{4}(\#1)} = (Z_p^4 Z_w^3)^{\frac{1}{7}}$$ (D-6-1)

The spring thickness, t_s, was determined from Equation (D-6-2) as obtain from (Brown et al. 2014).

$$t_s = \frac{\rho_s v_s^2}{2\pi f_o(Z_{\frac{\lambda}{4}(\#1)})}$$ (D-6-2)

where, ρ_s, is the density of parylene, 1,100 kg/m³, (Fei et al. 2015). v_s, is the velocity of sound in parylene of 2,135 m/s, (Brown et al. 2014), f_o, is the center frequency of the array (40 MHz). From (D-6-1) $Z_{\lambda/4(\#1)}$ is equal to 8.309 MRayls given an acoustic impedance of PZT-5H where Z_p is 30 MRayls (Lu and Proulx 2005) and an acoustic impedance for water Z_w of 1.5 MRayls. As such, t_s, solves to a thickness of 2.4 μm. The required mass thickness is then given by:

$$t_m = \frac{\rho_s v_s^2}{t_s \rho_m (2\pi f_o)^2} - \frac{0.4\rho_s t_s}{\rho_m}$$ (D-6-3)

where, ρ_m, is the density of copper (8960 kg/m³) and Equation (D-6-3) solves to 3.6 μm for t_m. The final ¼λ matching layer of parylene is then given a desired acoustic impedance of

2.3 MRayls from Equation (D-6-5) which approximates the actual impedance of parylene of 2.65 MRayl (Brown et al. 2014).

$$t_{\frac{1}{4}} = \frac{\lambda_{parylene}}{4} = \frac{c_{parylene}}{4f_o} \tag{D-6-4}$$

The final thickness of the final ¼λ matching layer of parylene is determined from the acoustic wavelength of the sound wave in parylene. From Equation (D-6-4) and the speed of sound in parylene ($c_{parylene}$) of 2,135 m/s the final parylene coating layer thickness is 13.3 μm at 40 MHz, as given by Equation (D-6-5).

$$Z_{\frac{\lambda}{4}(\#2)} = (Z_p Z_w^6)^{\frac{1}{7}} \tag{D-6-5}$$

The advantage of the detailed mass-spring & one-quarter wavelength matching layer is that it allows for a high-bandwidth dual matching layer configuration while using materials that can be vacuum deposited. The vacuum deposition of materials removes losses associated with imperfections in the traditional matching layer bonding and lamination process that become significant at fine feature characteristics seen in high-frequency transducers (Brown et al. 2014).

A polymer lens (Alumilite Water-Clear, Alumilite Corporation, USA) with a speed of sound of 2300 m/s, was cast onto the distal end of the array, with a specific radius of curvature, R_c, for a focal depth of 6.5 mm. The standard lens focus is given by (Maréchal et al. 2004) where n is the velocity ratio between the lens and water and equal to ~0.65:

$$F = \frac{R_c}{(1-n)} \tag{D-6-6}$$

The lens curvature is more accurately solved for by using the formula given by equation (D-6-7) as discussed in (Maréchal et al. 2004):

$$F_e = \frac{F}{1 + \left(\frac{2}{3}\right)\left(\frac{F}{L_{nf}}\right)^{\frac{4}{3}}} \quad Wherein: \quad L_{nf} = \frac{a^2}{\lambda} \tag{D-6-7}$$

where F_e is the effective focal distance of 6.5 mm, a is the source aperture of 1.52 mm and λ is the pulse wavelength in water of 38 μm. By combining equations (D-6-6) and (D-6-7),

then solving for R_c an ideal lens curvature of 2.35 mm was determined. Due to availability, a Teflon rod of 4.8 mm in diameter was used. The lens was cast using a custom machined Teflon fixture at a temperature of 90 °C and at a pressure of 120 psi to prevent bubbles from forming during casting.

APPENDIX E:

COPYRIGHT PERMISSION LETTERS

Fabrication and performance of a miniaturized 64-element high-frequency endoscopic phased array

Author: Andre Bezanson

Publication: Ultrasonics, Ferroelectrics and Frequency Control, IEEE Transactions on

Publisher: IEEE

Date: January 2014

Copyright © 2014, IEEE

IEEE
Requesting permission to reuse content from an IEEE publication

Thesis / Dissertation Reuse

The IEEE does not require individuals working on a thesis to obtain a formal reuse license, however, you may print out this statement to be used as a permission grant:

Requirements to be followed when using any portion (e.g., figure, graph, table, or textual material) of an IEEE copyrighted paper in a thesis:

1) In the case of textual material (e.g., using short quotes or referring to the work within these papers) users must give full credit to the original source (author, paper, publication) followed by the IEEE copyright line © 2011 IEEE.
2) In the case of illustrations or tabular material, we require that the copyright line © [Year of original publication] IEEE appear prominently with each reprinted figure and/or table.
3) If a substantial portion of the original paper is to be used, and if you are not the senior author, also obtain the senior author's approval.

Requirements to be followed when using an entire IEEE copyrighted paper in a thesis:

1) The following IEEE copyright/ credit notice should be placed prominently in the references: © [year of original publication] IEEE. Reprinted, with permission, from [author names, paper title, IEEE publication title, and month/year of publication]
2) Only the accepted version of an IEEE copyrighted paper can be used when posting the paper or your thesis on-line.
3) In placing the thesis on the author's university website, please display the following message in a prominent place on the website: In reference to IEEE copyrighted material which is used with permission in this thesis, the IEEE does not endorse any of [university/educational entity's name goes here]'s products or services. Internal or personal use of this material is permitted. If interested in reprinting/republishing IEEE copyrighted material for advertising or promotional purposes or for creating new collective works for resale or redistribution, please go to http://www.ieee.org/publications_standards/publications/rights/rights_link.html to learn how to obtain a License from RightsLink.

If applicable, University Microfilms and/or ProQuest Library, or the Archives of Canada may supply single copies of the dissertation.

BACK   CLOSE

The Journal of Laryngology & Otology

18 February 2020

Dear Mr Bezanson

Thank you for your letter regarding a request to reproduce figure 4 from the Journal of Laryngology and Otology 2014, 128; 425-430 Rousset, J., Garetier, M., Gentric, J., Chinellato, S., Barberot, C., Le Bivic, T., & Mériot, P. (2014). Biometry of the normal stapes using stapes axial plane, high-resolution computed tomography

JLO (1984) Ltd is happy to grant permission for use in this presentation only but please ensure that full acknowledgement of the source is made.

Yours sincerely,

Rosamund Greensted
Managing Editor

Mr A Bezanson

December 3, 2019

Andre Bezanson
39 Ridgepark Ln
Halifax, NS B3N 3J2
Canada

Dear Andre Bezanson:

The Radiological Society of North America (RSNA®) is pleased to grant you permission to reproduce the following figure in print and electronic format for use in your thesis entitled *Design, fabrication, and performance of a high-frequency phased-array ultrasonic endoscope*, provided you give full credit to the authors of the original publication.

> Figure 3
> Juliano A F, Ginat D T, Moonis G. Imaging Review of the Temporal Bone: Part I. Anatomy and Inflammatory and Neoplastic Processes. *Radiology* 2013;269:17-33.

This permission is a one-time, non-exclusive grant for English-language use and is exclusively limited to the usage stated and underlined above. The requestor guarantees to reproduce the material as originally published. Permission is granted under the condition that a full credit line is prominently placed (i.e. author name(s), journal name, copyright year, volume #, inclusive pages and copyright holder).

This permission becomes effective upon receipt of this signed contract. Please sign a copy of this agreement, return a signed copy to me and retain a copy for your files. Thank you for your interest in our publication.

[Print Name]:   Andre Bezanson

SIGNATURE: **Redacted**   Date: 2019-12-04

Sincerely,

Redacted

Ashley E. Daly
Senior Manager, Journal Rights & Communications
Publications

Phone: 630-590-7771
Fax: 630-590-7724
E-mail: *permissions@rsna.org*

172

IEEE
Requesting permission to reuse content from an IEEE publication

A high-frequency linear ultrasonic array utilizing an interdigitally bonded 2-2 piezo-composite

Author: Jonathan M. Cannata

Publication: Ultrasonics, Ferroelectrics and Frequency Control, IEEE Transactions on

Publisher: IEEE

Date: October 2011

Copyright © 2011, IEEE

Thesis / Dissertation Reuse

The IEEE does not require individuals working on a thesis to obtain a formal reuse license, however, you may print out this statement to be used as a permission grant:

Requirements to be followed when using any portion (e.g., figure, graph, table, or textual material) of an IEEE copyrighted paper in a thesis:

1) In the case of textual material (e.g., using short quotes or referring to the work within these papers) users must give full credit to the original source (author, paper, publication) followed by the IEEE copyright line © 2011 IEEE.
2) In the case of illustrations or tabular material, we require that the copyright line © [Year of original publication] IEEE appear prominently with each reprinted figure and/or table.
3) If a substantial portion of the original paper is to be used, and if you are not the senior author, also obtain the senior author's approval.

Requirements to be followed when using an entire IEEE copyrighted paper in a thesis:

1) The following IEEE copyright/ credit notice should be placed prominently in the references: © [year of original publication] IEEE. Reprinted, with permission, from [author names, paper title, IEEE publication title, and month/year of publication]
2) Only the accepted version of an IEEE copyrighted paper can be used when posting the paper or your thesis on-line.
3) In placing the thesis on the author's university website, please display the following message in a prominent place on the website: In reference to IEEE copyrighted material which is used with permission in this thesis, the IEEE does not endorse any of [university/educational entity's name goes here]'s products or services. Internal or personal use of this material is permitted. If interested in reprinting/republishing IEEE copyrighted material for advertising or promotional purposes or for creating new collective works for resale or redistribution, please go to http://www.ieee.org/publications_standards/publications/rights/rights_link.html to learn how to obtain a License from RightsLink.

If applicable, University Microfilms and/or ProQuest Library, or the Archives of Canada may supply single copies of the dissertation.

BACK

CLOSE

ASA Standards \<standards@acousticalsociety.org\>
Thu 2/27/2020 1:25 PM
Andre Bezanson ⌄

Permission granted as requested.

Nancy A. Blair-DeLeon
Standards Manager
Acoustical Society of America
Office: +1 (516) 576-2341
Mobile: +1 (573) 219-8291

. . .

| Thank you! | Thank you so much! | Permission granted! |

💬 Are the suggestions above helpful? Yes   No

Andre Bezanson
Thu 2/27/2020 11:02 AM
asastds@acousticalsociety.org ⌄

📄 **PermissionRequest_ASOA.pdf**
    75 KB

Hello,

I'd like to request permission to publish redrawn copies of Fig1 and Fig 2 from:

J. L. SanEmeterio and L. G. Ullate, "Diffraction impulse response of rectangular transducers," *The Journal of the Acoustical Society of America,* vol. 92, no. 2, pp. 651-662, 1992.

I'm looking to include these in my thesis that I'll be defending next month

Best Regards,

Andre Bezanson
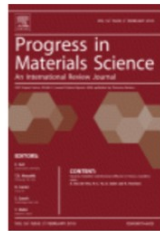
Thank you for your order!

Dear Mr. Andre Bezanson,

Thank you for placing your order through Copyright Clearance Center's RightsLink® service.

Order Summary

Licensee:	Dalhousie University
Order Date:	Feb 27, 2020
Order Number:	4777110543937
Publication:	Progress in Materials Science
Title:	Piezoelectric films for high frequency ultrasonic transducers in biomedical applications
Type of Use:	reuse in a thesis/dissertation
Order Ref:	Andre_KLMFig
Order Total:	0.00 CAD

View or print complete details of your order and the publisher's terms and conditions.

Sincerely,

Copyright Clearance Center